AFRL-RY-HS-TR-2010-0019

COMPLEX WAVES ON 1D, 2D, AND 3D PERIODIC ARRAYS OF LOSSY AND LOSSLESS MAGNETODIELECTRIC SPHERES

Dr. Robert A. Shore
Dr. Arthur D. Yaghjian

Electromagnetics Technology Division
Antenna Technology Branch
AFRL/RYHA

16 May 2010

In-House Technical Report

APPROVED FOR PUBLIC RELEASE; DISTRIBUTION UNLIMITED.

AIR FORCE RESEARCH LABORATORY
Sensors Directorate
Electromagnetics Technology Division
Antenna Technology Branch
80 Scott Drive
Hanscom AFB MA 01731-2909

NOTICE AND SIGNATURE PAGE

Using Government drawings, specifications, or other data included in this document for any purpose other than Government procurement does not in any way obligate the U.S. Government. The fact that the Government formulated or supplied the drawings, specifications, or other data does not license the holder or any other person or corporation; or convey any rights or permission to manufacture, use, or sell any patented invention that may relate to them.

This report was cleared for public release by the Electronic Systems Center Public Affairs Office for the Air Force Research Laboratory Electromagnetic Technology Division and is available to the general public, including foreign nationals. Copies may be obtained from the Defense Technical Information Center (DTIC) (http://www.dtic.mil).

AFRL-RY-HS-TR-2010-0019 HAS BEEN REVIEWED AND IS APPROVED FOR PUBLICATION IN ACCORDANCE WITH ASSIGNED DISTRIBUTION STATEMENT.

Robert A Shore

ROBERT A SHORE
Program Manager

David Curtis

DAVID CURTIS
Branch Chief
Antenna Technology Branch

Robert V. McGahan

ROBERT V MCGAHAN
Technical Communications Advisor
Electromagnetic Technology Division

This report is published in the interest of scientific and technical information exchange, and its publication does not constitute the Government's approval or disapproval of its ideas or findings.

REPORT DOCUMENTATION PAGE

Form Approved
OMB No. 0704-0188

Public reporting burden for this collection of information is estimated to average 1 hour per response, including the time for reviewing instructions, searching existing data sources, gathering and maintaining the data needed, and completing and reviewing this collection of information. Send comments regarding this burden estimate or any other aspect of this collection of information, including suggestions for reducing this burden to Department of Defense, Washington Headquarters Services, Directorate for Information Operations and Reports (0704-0188), 1215 Jefferson Davis Highway, Suite 1204, Arlington, VA 22202-4302. Respondents should be aware that notwithstanding any other provision of law, no person shall be subject to any penalty for failing to comply with a collection of information if it does not display a currently valid OMB control number. **PLEASE DO NOT RETURN YOUR FORM TO THE ABOVE ADDRESS.**

1. REPORT DATE *(DD-MM-YYYY)*	2. REPORT TYPE	3. DATES COVERED *(From - To)*
16-05-2010	IN-HOUSE	1 Nov 2006 – 16 May 2010

4. TITLE AND SUBTITLE

Complex Waves on 1D, 2D, and 3D Periodic Arrays of Lossy and Lossless Magnetodielectric Spheres

5a. CONTRACT NUMBER

5b. GRANT NUMBER

5c. PROGRAM ELEMENT NUMBER
61102F

6. AUTHOR(S)

Robert A. Shore and Arthur D. Yaghjian

5d. PROJECT NUMBER
2304

5e. TASK NUMBER
HE

5f. WORK UNIT NUMBER
01

7. PERFORMING ORGANIZATION NAME(S) AND ADDRESS(ES)
AFRL/RYHA
80 Scott Drive
Hanscom AFB, MA 01731-2909

8. PERFORMING ORGANIZATION REPORT

9. SPONSORING / MONITORING AGENCY NAME(S) AND ADDRESS(ES)
Electromagnetics Technology Division
Sensors Directorate
Air Force Research Laboratory
80 Scott Drive
Hanscom AFB MA 01731-2909

10. SPONSOR/MONITOR'S ACRONYM(S)
AFRL-RY-HS

11. SPONSOR/MONITOR'S REPORT NUMBER(S)
AFRL-RY-HS-TR-2010-0019

12. DISTRIBUTION / AVAILABILITY STATEMENT
Approved for public release; distribution unlimited. ESC PA 66ABW-2010-0145

13. SUPPLEMENTARY NOTES

14. ABSTRACT
Complex waves propagating along the axes of 1D, 2D and 3D infinite periodic arrays of small lossless and lossy magnetodielectric spheres are investigated. The focus is on obtaining the kd–βd equations (diagrams) characterizing dipolar complex waves. The kd–βd (dispersion) equation for the complex propagation constants of a given array is obtained from the corresponding equation previously obtained for the real propagation constants by rewriting the real propagation dispersion equation in a form that can be analytically continued into the complex βd plane. This equation reduces correctly to the real βd dispersion equation and enables complex values of βd to be found as a function of kd and the array element parameters. By allowing for all the possible branches of the multivalued homogeneous dispersion equation analytically continued into the complex βd plane, the propagation constants of all the improper as well as proper complex waves supported by the 1D, 2D, and 3D arrays are found from the homogeneous solutions for these arrays. Green's functions are not required to find the propagation constants of the complex waves supported by the arrays. The kd–βd equations for complex βd are solved by searching a given region of the complex βd plane with a progressively finer grid for the value of βd that minimizes the absolute value of the dispersion equation. A final very accurate value for the zero is then obtained using an IMSL implementation of a quasi-Newton algorithm or of Müller's Method. Computer programs have been written to obtain the kd–βd diagrams for all the arrays treated, and extensive numerical results are presented and discussed. For 3D arrays of magnetodielectric spheres, it is possible in certain regions of the kd–βd diagrams to regard the arrays as media characterized by bulk or effective permittivities and permeabilities. Expressions have been obtained for these bulk parameters utilizing quantities readily available from solving the kd–βd equations. These expressions are more accurate than the Clausius-Mossotti bulk-parameter expressions.

15. SUBJECT TERMS
Periodic arrays, traveling waves, complex propagation constants, magnetodielectric spheres, bulk parameters

16. SECURITY CLASSIFICATION OF:			17.LIMITATION OF ABSTRACT	18.NUMBER OF PAGES	19a. NAME OF RESPONSIBLE PERSON
a. REPORT	b. ABSTRACT	c. THIS PAGE	SAR	104	Dr. Robert A. Shore
Unclassified	Unclassified	Unclassified			19b. TELEPHONE NUMBER *(include area code)* N/A

Standard Form 298 (Rev. 8-98)
Prescribed by ANSI Std. Z39.18

Contents

1 INTRODUCTION 1

2 1D ARRAYS 9
- 2.1 ELECTRIC AND MAGNETIC DIPOLES PERPENDICULAR TO THE ARRAY AXIS . . . 10
- 2.2 DIPOLES PARALLEL TO THE ARRAY AXIS . . . 13

3 2D ARRAYS 13
- 3.1 ELECTRIC AND MAGNETIC DIPOLES PERPENDICULAR TO THE ARRAY AXIS . . . 14
  - 3.1.1 ELECTRIC DIPOLES IN THE ARRAY PLANE . . . 14
  - 3.1.2 ELECTRIC DIPOLES PERPENDICULAR TO THE ARRAY PLANE . . . 18
- 3.2 DIPOLES PARALLEL TO THE ARRAY AXIS . . . 18

4 3D ARRAYS 20
- 4.1 ELECTRIC AND MAGNETIC DIPOLES PERPENDICULAR TO THE ARRAY AXIS . . . 20
- 4.2 DIPOLES PARALLEL TO THE ARRAY AXIS . . . 23

5 EFFECTIVE PERMITTIVITY AND PERMEABILITY 25

6 PARTIALLY FINITE ARRAYS 27

7 BIDIRECTIONALITY AND COMPLEX CONJUGATES OF WAVES 28

8 NUMERICAL RESULTS 32
- 8.1 MAGNETODIELECTRIC SPHERE ARRAYS . . . 33
  - 8.1.1 LINEAR (1D) ARRAYS OF MAGNETODIELECTRIC SPHERES . . . 33
  - 8.1.2 2D ARRAYS OF MAGNETODIELECTRIC SPHERES . . . 35
  - 8.1.3 3D ARRAYS OF MAGNETODIELECTRIC SPHERES . . . 35
  - 8.1.4 EFFECTIVE PARAMETERS FOR 3D ARRAYS OF MAGNETODIELECTRIC SPHERES . . . 36
- 8.2 DIAMOND SPHERES . . . 37
  - 8.2.1 LINEAR (1D) ARRAYS OF DIAMOND SPHERES . . . 37
  - 8.2.2 2D ARRAYS OF DIAMOND SPHERES . . . 37
  - 8.2.3 3D ARRAYS OF DIAMOND SPHERES . . . 38
- 8.3 SILVER NANOSPHERE ARRAYS . . . 38
  - 8.3.1 LINEAR (1D) ARRAYS OF SILVER NANOSPHERES . . . 38
  - 8.3.2 2D ARRAYS OF SILVER NANOSPHERES . . . 40
  - 8.3.3 3D ARRAYS OF SILVER NANOSPHERES . . . 41

A COMPLEX WAVES SUPPORTED BY A TWO-DIMENSIONAL SLAB 76
- A.1 INHOMOGENEOUS BOUNDARY VALUE PROBLEM FOR THE SLAB . . . 76
- A.2 HOMOGENEOUS BOUNDARY VALUE PROBLEM FOR THE SLAB . . . 79
- A.3 INTEGRATION OVER POLARIZATION . . . 80

B DIVERGENCE OF COMPLEX-WAVE FIELDS OBTAINED FROM DIRECT SUMMATION OF DIPOLE FIELDS OF PERIODIC ARRAYS **82**

C PROPERTIES OF COMPLEX WAVES ON UNIFORM OR PERIODIC WAVEGUIDES **86**

C.1 INTRODUCTION TO COMPLEX WAVES 86

C.2 FAST AND SLOW WAVES 89

REFERENCES **91**

List of Figures

1 Branch cuts in the complex βd plane for the two alternative expressions for $F_{1+}(kd, \beta d)$. 13
2 kd–βd diagram for a 1D periodic array of magnetodielectric spheres with $\epsilon_r = \mu_r = 10$, and $a/d = 0.45$; dipoles perpendicular to array axis; βd real. 43
3 kd–βd diagram for a 1D periodic array of magnetodielectric spheres with $\epsilon_r = \mu_r = 10$, and $a/d = 0.45$; dipoles perpendicular to array axis; βd complex. 43
4 kd–βd diagram for a 1D periodic array of magnetodielectric spheres with $\epsilon_r = \mu_r = 10$, and $a/d = 0.45$; dipoles perpendicular to array axis; βd complex. Multiple modes shown. 44
5 kd–βd diagram for a 1D periodic array of magnetodielectric spheres with $\epsilon_r = \mu_r = 10$, and $a/d = 0.45$; electric dipoles only; βd real. 45
6 kd–βd diagram for a 1D periodic array of magnetodielectric spheres with $\epsilon_r = \mu_r = 10$, and $a/d = 0.45$; electric dipoles only; βd complex. 45
7 kd–βd diagram for a 1D periodic array of magnetodielectric spheres with $\epsilon_r = \mu_r = 20$, and $a/d = 0.45$; dipoles perpendicular to array axis; βd real. 46
8 kd–βd diagram for a 1D periodic array of magnetodielectric spheres with $\epsilon_r = \mu_r = 20$, and $a/d = 0.45$; dipoles perpendicular to array axis; βd complex. 46
9 kd–βd diagram for a 1D periodic array of magnetodielectric spheres with $\epsilon_r = \mu_r = 20$, and $a/d = 0.45$; dipoles perpendicular to array axis; βd complex. Multiple modes shown. 47
10 kd–βd diagram for a 1D periodic array of magnetodielectric spheres with $\epsilon_r = \mu_r = 20$ and $a/d = 0.45$; dipole moments parallel to propagation direction; βd real. 48
11 kd–βd diagram for a 1D periodic array of magnetodielectric spheres with $\epsilon_r = \mu_r = 20$ and $a/d = 0.45$; dipole moments parallel to propagation direction; βd complex. . . . 48
12 kd–βd diagram for a 2D square-lattice array of magnetodielectric spheres with $\epsilon_r = \mu_r = 20$ and $a/d = .45$; electric dipole moments parallel or perpendicular to the array plane; βd real. 49
13 kd–βd diagram for a 2D square-lattice array of magnetodielectric spheres with $\epsilon_r = \mu_r = 20$ and $a/d = .45$; electric dipole moments parallel or perpendicular to the array plane; βd complex. 49
14 kd–βd diagram for a 2D square-lattice array of magnetodielectric spheres with $\epsilon_r = \mu_r = 20$ and $a/d = .45$; electric dipole moments parallel or perpendicular to the array plane; βd complex; detail. 50
15 kd–βd diagram for a 2D square-lattice array of magnetodielectric spheres with $\epsilon_r = \mu_r = 20$ and $a/d = .45$; electric dipole moments parallel or perpendicular to the array plane; βd complex. Multiple modes shown. 51
16 kd–βd diagram for a 2D square-lattice array of magnetodielectric spheres with $\epsilon_r = \mu_r = 20$ and $a/d = .45$; electric dipole moments parallel or perpendicular to the array plane; βd complex. Multiple modes shown; detail. 51
17 kd–βd diagram for a 3D cubic-lattice array of $\epsilon_r = \mu_r = 20$ magnetodielectric spheres (dipole moments normal to the propagation direction) with $a/d = .45$; βd real. . . . 52
18 kd–βd diagram for a 3D cubic-lattice array of $\epsilon_r = \mu_r = 20$ magnetodielectric spheres (dipole moments normal to the propagation direction) with $a/d = .45$; βd complex. Multiple modes shown. 52
19 kd–βd diagram for 3D cubic-lattice arrays of $(\epsilon_r = 20.0, \mu_r = 20.0 + 0.04\mathrm{i})$, $(\epsilon_r = 20.0, \mu_r = 20.0 + 0.4\mathrm{i})$, magnetodielectric spheres (dipole moments normal to the propagation direction) with $a/d = .45$; βd complex. 53

20 kd–βd curves for 3D cubic-lattice arrays of magnetodielectric spheres; 1) $\epsilon_r = (13.8, 0.0)$, $\mu_r = (11.0, 0.0)$; 2) $\epsilon_r = (13.8, 0.1)$, $\mu_r = (11.0, 0.0)$; dipole moments perpendicular to array axis; $a/d = 0.4$. 54
21 Effective permeability and permeability of 3D cubic-lattice arrays of magnetodielectric spheres; 1) $\epsilon_r = (13.8, 0.0)$, $\mu_r = (11.0, 0.0)$; 2) $\epsilon_r = (13.8, 0.1)$, $\mu_r = (11.0, 0.0)$; dipole moments perpendicular to array axis; $a/d = 0.4$. 54
22 kd–βd diagram for a 1D periodic array of diamond spheres; dipole moments normal to the propagation direction; $a/d = .45$; βd real. 55
23 kd–βd diagram for a 1D periodic array of diamond spheres; dipole moments normal to the propagation direction; $a/d = .45$; βd complex. 55
24 kd–βd diagram for a 1D periodic array of diamond spheres; dipole moments normal to the propagation direction; $a/d = .45$; βd complex. Multiple modes shown. 56
25 kd–βd diagram for a 1D periodic array of diamond spheres; magnetic dipole moments parallel to the propagation direction; $a/d = .45$; βd real. 57
26 kd–βd diagram for a 1D periodic array of diamond spheres; magnetic dipole moments parallel to the propagation direction; $a/d = .45$; βd complex. 57
27 kd–βd diagram for a 2D square-lattice array of diamond spheres; electric dipole moments parallel to the array plane; $a/d = .45$; βd real. 58
28 kd–βd diagram for a 2D square-lattice array of diamond spheres; electric dipole moments parallel to the array plane; $a/d = .45$; βd complex. 58
29 kd–βd diagram for a 2D square-lattice array of diamond spheres; electric dipole moments parallel to the array plane; $a/d = .45$; βd complex. Multiple modes shown. 59
30 kd–βd diagram for a 2D square-lattice array of diamond spheres; electric dipole moments parallel to the array plane; $a/d = .45$; βd complex. Multiple modes shown; detail. 59
31 kd–βd diagram for a 2D square-lattice array of diamond spheres; electric dipole moments perpendicular to the array plane; $a/d = .45$; βd real. 60
32 kd–βd diagram for a 2D square-lattice array of diamond spheres; electric dipole moments perpendicular to the array plane; $a/d = .45$; βd complex. 60
33 kd–βd diagram for a 2D square-lattice array of diamond spheres; electric dipole moments perpendicular to the array plane; $a/d = .45$; βd complex. Multiple modes shown. 61
34 kd–βd diagram for a 2D square-lattice array of diamond spheres; electric dipole moments perpendicular to the array plane; $a/d = .45$; βd complex. Multiple modes shown; detail. 61
35 kd–βd diagram for a 2D square-lattice array of diamond spheres; magnetic dipole moments parallel to the propagation direction; $a/d = .45$; βd real. 62
36 kd–βd diagram for a 2D square-lattice array of diamond spheres; magnetic dipole moments parallel to the propagation direction; $a/d = .45$; βd complex. 62
37 kd–βd diagram for a 3D cubic-lattice array of diamond spheres; dipole moments normal to the propagation direction; $a/d = .45$; βd real. 63
38 kd–βd diagram for a 3D cubic-lattice array of diamond spheres; dipole moments normal to the propagation direction; $a/d = .45$; βd complex. 63
39 kd–βd diagram for a 3D cubic-lattice array of diamond spheres; dipole moments normal to the propagation direction; $a/d = .45$; βd complex. Multiple modes shown. 64
40 kd–βd diagram for a 3D cubic-lattice array of diamond spheres; dipole moments normal to the propagation direction; $a/d = .45$; βd complex. Multiple modes shown; detail. 64

41 kd–βd diagram for a 3D cubic-lattice array of diamond spheres; magnetic or electric dipole moments parallel to the propagation direction; $a/d = .45$; βd real. 65
42 kd–βd diagram for a 3D cubic-lattice array of diamond spheres; magnetic or electric dipole moments parallel to the propagation direction; $a/d = .45$; βd complex. 65
43 kd–βd curves for a 1D periodic array of glass-embedded silver nanospheres; dipole moments normal to the propagation direction; $a = 5$ nm; permittivity real; βd real. . 66
44 kd–βd curves for a 1D periodic array of lossy glass-embedded silver nanospheres; dipole moments normal to the propagation direction; $a = 5$ nm; βd complex. 66
45 kd–βd curves for a 1D periodic array of glass-embedded silver nanospheres; electric dipole moments parallel to the direction of propagation; $a = 5$ nm; permittivity real; βd real. 67
46 kd–βd curves for a 1D periodic array of lossy glass-embedded silver nanospheres; electric dipole moments parallel to the direction of propagation; $a = 5$ nm; βd complex. 67
47 kd–βd curves for a 1D periodic array of lossy glass-embedded silver nanospheres; electric dipole moments parallel to the direction of propagation; $a = 5$ nm; βd complex; detail. 68
48 kd–βd curves for a 1D periodic array of lossy glass-embedded silver nanospheres; electric dipole moments parallel to the direction of propagation; $a = 5$ nm; βd complex; alternative branches shown. 68
49 kd–βd curves for a 2D square-lattice array of glass-embedded silver nanospheres; electric dipole moments parallel to the array plane; $a = 5$ nm; $s = 1, 4$ nm; permittivity real; βd real. 69
50 kd–βd curves for a 2D square-lattice array of glass-embedded silver nanospheres; electric dipole moments parallel to the array plane; $a = 5$ nm; $s = 1$ nm; permittivity complex; βd complex. 69
51 kd–βd curves for a 2D square-lattice array of glass-embedded silver nanospheres; electric dipole moments parallel to the array plane; $a = 5$ nm; $s = 1$ nm; permittivity complex; βd complex. Multiple modes shown. 70
52 kd–βd curves for a 2D square-lattice array of glass-embedded silver nanospheres; electric dipole moments parallel to the array plane; $a = 5$ nm; $s = 1$ nm; permittivity real; βd complex. 70
53 kd–βd curves for a 2D square-lattice array of glass-embedded silver nanospheres; electric dipole moments perpendicular to the array plane; $a = 5$ nm; $s = 1, 4$ nm; permittivity real; βd real. 71
54 kd–βd curves for a 2D square-lattice array of glass-embedded silver nanospheres; electric dipole moments perpendicular to the array plane; $a = 5$ nm; $s = 1$ nm; permittivity complex; βd complex. 71
55 kd–βd curves for a 2D square-lattice array of glass-embedded silver nanospheres; electric dipole moments perpendicular to the array plane; $a = 5$ nm; $s = 1$ nm; permittivity complex; βd complex. Multiple modes shown. 72
56 kd–βd curves for a 2D square-lattice array of glass-embedded silver nanospheres; electric dipole moments perpendicular to the array plane; $a = 5$ nm; $s = 4$ nm; βd complex. 72
57 kd–βd curves for a 2D square-lattice array of glass-embedded silver nanospheres; electric dipole moments parallel to the direction of propagation; $a = 5$ nm; permittivity real; βd real. 73

58 kd–βd curves for a 2D square-lattice array of glass-embedded silver nanospheres; electric dipole moments parallel to the direction of propagation; $a = 5$ nm; βd complex. 73
59 kd–βd curves for a 3D cubic-lattice array of glass-embedded silver nanospheres; dipole moments normal to the propagation direction; $a = 5$ nm; permittivity real; βd real. 74
60 kd–βd curves for a 3D cubic-lattice array of glass-embedded silver nanospheres; dipole moments normal to the propagation direction; $a = 5$ nm; permittivity complex; βd complex. 74
61 kd–βd curves for a 3D cubic-lattice array of glass-embedded silver nanospheres; electric dipole moments parallel to the direction of propagation; $a = 5$ nm ; permittivity real; βd real. 75
62 kd–βd curves for a 3D cubic-lattice array of glass-embedded silver nanospheres; electric dipole moments parallel to the direction of propagation); $a = 5$ nm; permittivity complex; βd complex. 75
63 Slab geometry. 77
64 The two proper complex waves for $z > 0$ (to the right of the sources) on lossless, reciprocal, open waveguides. 89
65 The two improper complex waves for $z > 0$ (to the right of the sources) on lossless, reciprocal, open waveguides. 89

ACKNOWLEDGMENT

This work was supported by the U.S. Air Force Office of Scientific Research (AFOSR) through Dr. Arje Nachman. The authors also express their thanks and appreciation to Prof. Andrea Alù (University of Texas, Austin), Dr. John Derov (RYHA, Air Force Research Laboratory), Prof. Nader Engheta (University of Pennsylvania), Prof. Chris Linton (Loughborough University, Great Britain), Prof. Richard Porter (University of Bristol, Great Britain), Prof. Jiming Song (Iowa State University), and Dr. Boris Tomasic (RYHA, Air Force Research Laboratory), for very helpful conversations and communications. Robert Shore wishes to express his deep gratitude to Mr. David D. Curtis, his branch chief at RYHA, for his long-standing support and encouragement, and for creating a work environment in which extended research efforts such as this one are possible.

1 INTRODUCTION

The subject of this report is traveling waves with complex propagation constants (complex waves) on one-, two-, and three-dimensional (1D, 2D, 3D) periodic arrays of lossless and lossy magnetodielectric spheres.[1] Such arrays are an important class of artificial composite materials – materials formed by embedding inclusions of one material in a matrix of another kind of material. Just like natural materials, artificial composite materials can have properties that are very different from those of their constituents when the scale of use or observation of the composite material (the macro-level) is much larger than the scale of the detailed structure of the composite material (the micro-level).[2] For example, it has been known since the seventeenth century that ruby-colored glass can be made by adding nanometer-sized gold particles to silicate glass [1]. Since the 1940's much attention has been given to artificial dielectrics made from lattices of different kinds of conducting elements. Similar interest in artificial magnetic materials dates from the 1950's.[3] The subject of photonic crystals [6]-[8] is a recent and very important extension of earlier work on artificial dielectrics to the optics frequency range. More recently there has been great interest in artificial composite materials characterized by a negative index of refraction (group and phase velocities in opposite directions), especially those having both their bulk permittivity and permeability negative [double negative (DNG) materials] [9]-[18].[4] In addition to the term "metamaterials" being commonly applied to such artificial negative index or doubly negative materials, the term has also come to be applied to any materials not found in nature, such as artificial dielectric and magnetic materials, and photonic crystals, whose microstructures have been engineered to result in desired macro-properties. The most interesting macro- or bulk properties of electromagnetic metamaterials are those related to how electromagnetic waves interact (scatter, propagate, refract, etc.) with the materials, hence the central importance in this report of the waves that can be supported by the periodic arrays we study. Indeed, as will be shown below, when the free-space and traveling-wave electrical separation distances between the elements in a 3D cubic-lattice periodic array are both small, the array can be regarded as a homogeneous isotropic medium whose bulk permittivity and permeability can be obtained from the solution to the dispersion equation for the array. (See, however, Footnote 23 in Section 5.)

Our investigation of complex traveling waves on periodic arrays of magnetodielectric spheres is motivated in part by the theoretical demonstration by Holloway *et al.* [23], based on work by Lewin [24], that a DNG material can be formed by embedding an array of spherical magnetodieletric

[1] The term "leaky wave" is sometimes used synonymously with the term "complex wave." Nonetheless, in this report we reserve the term "leaky wave" for outgoing improper complex waves; see Appendix C.

[2] Almost needless to say, the distinction between macro-properties and microstructure is so basic and far reaching as to be taken for granted in our world view of the molecular and atomic structure of matter or of the cellular structure of biological organisms.

[3] A good summary of early work in artificial dielectrics and magnetics is given in [2]. A review of early work in artificial plasmas as well as of early work in artificial dielectrics and magnetics can be found in [3]. A static-field treatment of artificial dielectrics is given in [4] and [5, ch. 12].

[4] The chapter in [17] by Simovski and Tretyakov referenced above (see [3]) includes a historical overview of early work on backward waves and negative refraction, and an excellent discussion of the controversy, dating from the early 2000's, regarding the possibility of negative refraction. Simovski and Tretyakov conclude that all the arguments that have been advanced to disprove the possibility of negative refraction have been convincingly refuted. (In this connection, it is unfortunate that the recent posthumous publication of a book by Munk [19] has revived arguments against the possibility of negative refraction and DNG materials that were refuted years ago. Indeed our own work [20, sec. 12.5],[21, sec. 6.4],[22] provides clear examples of theoretically possible DNG metamaterials. While skepticism regarding the practical importance of DNG structures in the foreseeable future is fully justified considering the paucity of significant practical applications to date, the validity of the theoretical foundations of negative refraction and DNG metamaterials is well established.)

particles in a background matrix[5] and by the current widespread interest in DNG metamaterials. An important application of our work is to the design of composite DNG metamaterials. Our work can be used, for example, to investigate how the frequency regions in which an array behaves as an isotropic homogeneous DNG medium depend on the permittivity, permeability, and packing of the array elements, and to estimate how losses in the elements affect the attenuation of waves propagating in composite DNG structures. The applicability of our work is not restricted to composite structures, however. It is also relevant, for example, to understanding the propagation of plasmonic waves on periodic chains of metallic optical nanospheres, to linear arrays of electric or magnetic dipoles such as the Yagi-Uda antenna, and to modeling frequency selective surfaces composed of planar periodic arrays of small electrically or magnetically polarizable elements.

The work to be described here is an extension of our previous investigations of traveling waves with *real* propagation constants supported by 1D, 2D, and 3D periodic rectangular-lattice arrays of lossless acoustic monopoles, electric or magnetic dipoles, and magnetodielectric spheres [25]-[30],[20]-[22] using a spherical-wave source scattering-matrix formulation. Unlike our previous work, in this report the array elements can be either lossless or lossy, and the propagation constants can be either real or complex. The propagation constants are always complex when the array elements are lossy, and can also be complex even when the array elements are lossless, as in the fast-wave region of 1D and 2D arrays of lossless magnetodielectric spheres, occasionally in the slow-wave region of these arrays close to the light line,[6] and in the stop-band regions (where no traveling wave with real βd exists) of 1D, 2D, and 3D arrays. Additionally, complex eigenmodes with high attenuation can be supported by 1D, 2D, and 3D periodic arrays of lossless scatterers.

The focus of our attention is the so-called k–β equation (diagram) — in our work more properly referred to as the kd–βd equation (diagram) — that relates the traveling wave electrical separation distance βd of the array elements in the direction parallel to a specified array axis along one of the principal rectangular-lattice directions, to the corresponding free-space electrical separation distance kd, where $k = \omega/c$ is the free-space wavenumber with $\omega > 0$ the angular frequency and c the free-space speed of light. An implicit harmonic time dependence of $\exp(-\mathrm{i}\omega t)$ is assumed here and throughout the report.

In this report we treat traveling waves only in the direction parallel to a specified array axis. Our objective is to formulate an efficient rigorous method to obtain the traveling-wave, array-element electrical separation distance βd ("propagation constant") of all the discrete waves – real or complex, proper or improper – propagating parallel to the array axis that can be supported by the array for a particular free-space, array-element electrical separation distance kd ("frequency"). This is accomplished by deriving and solving the exact (to within the dipole approximation) source-free kd–βd equation for the array. Thus, all the "propagation constants" of the discrete waves are found from an analysis of the source-free array, without having to resort to determining the full

[5]Lewin's procedure for obtaining the effective permittivity and permeability of a mixture consisting of a homogeneous material in which is embedded a cubic lattice of magnetodielectric particles is quite different from ours although there are some similarities. He considers the problem of a plane wave incident on a half-space of the mixture, and obtains the propagation constant of the transmitted wave by first calculating the electric and magnetic field incident on a reference particle as the sum of the transmitted wave plus the sum of the Mie electric and magnetic dipole fields scattered from all the particles of the lattice other than the reference particle itself. He then evaluates the summations by approximating them by integrals, leading to a simultaneous pair of integral equations which can be solved for the propagation constant of the transmitted wave. This in turn allows him to calculate the wave reflected from the interface, and knowing both the transmitted and reflected waves he obtains expressions for the bulk parameters of the mixture. Although ingenious, his procedure is far more complicated, unnecessarily, than ours and is approximate rather than exact as ours is (to within the dipole approximation). Furthermore, unlike Lewin's work, in our work the conditions for the validity of the bulk parameter expressions we derive are extremely simple.

[6]In our plots of kd–βd (dispersion) diagrams the light line is the line $\Re(\beta d) = kd$, to the left of which is the fast-wave region, $0 \leq \Re(\beta d) < kd$, and to the right of which is the slow-wave region, $kd < \Re(\beta d) \leq \pi$.

Green's function solution for the array.[7]

The restriction to waves traveling in a direction parallel to a specified array axis greatly simplifies the analysis because of the rectangular-lattice periodic arrays investigated here; the analysis of waves traveling in an arbitrary direction in 2D or 3D arrays would be far more complicated. However, even though the traveling waves treated are assumed to be in a direction parallel to an array axis, it will be seen below (see Section 5) that when both $|\beta d|$ and kd are less than about one, a 3D cubic-lattice array of identical magnetodielectric spheres can be regarded as a homogeneous isotropic medium whose bulk permittivity and permeability are obtainable from the solution of the kd–βd equation for a transverse wave traveling parallel to the array axis. Thus, the solution of the dispersion equation of a wave propagating parallel to the direction of an axis of a 3D cubic-lattice array leads directly to knowing in what frequency region the array can be regarded as a homogeneous isostropic medium, and to knowing the values of the bulk parameters in that frequency region determining wave propagation in an arbitrary direction in that medium. (See, however, Footnote 23 in Section 5.)

The class of problems analyzed in this report can be described as follows. We consider periodic arrays – 1D, 2D, or 3D – of identical, radially symmetric elements, lossy or lossless, with the elements characterized by two scattering coefficients that relate the electric and magnetic elementary dipole fields scattered from an element to the incident electric and magnetic fields at the element center. As in our previous related work, it is assumed that the array elements are sufficiently small, or the frequency ranges investigated sufficiently low, so that only the fields of the lowest order spherical multipoles (electromagnetic dipoles) are significant in analyzing scattering from the array elements. All the multiple interactions among these dipole elements are taken into account so that our analyses are exact to within the dipole field approximation. The spacing of elements in the direction parallel to the array axis is denoted by d and in the direction or directions normal to the array axis by h. For any of these arrays we obtain and solve the kd–βd equation, where βd can be either real or complex, and plot the resulting kd–βd diagram. A 3D array, when both $|\beta d|$ and kd are less than about one, and when the longitudinal element separation d equals the transverse element separation h, can generally be regarded as a homogeneous isotropic medium with effective bulk permittivity and permeability. When $|\beta d|$ and kd are sufficiently small for a 3D array to be regarded as homogeneous and isotropic, we obtain values for these bulk parameters from the solution of the kd–βd equation for the array. (See, however, Section 5, Footnote 23.)

Some basic properties of the kd–βd diagram may be noted here. In [35, ch. 7] it is shown that the dependence of the kd–βd diagram on βd is periodic in βd with a period of 2π. In Appendix A of [20] and the paper [36], it is proven that if a periodic array of reciprocal elements supports a traveling wave with propagation constant β, it also supports a corresponding traveling wave with propagation constant $-\beta$. Therefore, for periodic arrays of reciprocal elements, as are all the arrays considered in this report, kd is an even function of βd. It follows that for $\Re(\beta d)$ in the interval $\pi < \Re(\beta d) < 2\pi$

$$kd(\beta d) = kd(2\pi - \beta d), \quad \pi < \Re(\beta d) < 2\pi \tag{1.1}$$

[7]The restriction of our analysis to source-free arrays has the limitation that it cannot be used to solve problems such as those treated, for example, in [31]–[34], involving periodic arrays excited by sources.

where we have written kd as a function of βd. Hence we need consider βd only in the interval[8]

$$0 < \Re(\beta d) \leq \pi \, . \tag{1.2}$$

If we restrict $\Re(\beta d)$ to this positive interval, however, $\Im(\beta d)$ needs to range over negative as well as positive values in order to find all the discrete complex waves that can propagate on arrays with lossy elements; see Appendix C.

Although there is no upper limit on the transverse inter-element spacing h for either 2D or 3D periodic arrays, the expressions we give for the rapidly convergent summations in the kd–βd equations are valid only for $kh < 2\pi$, that is, for h less than a wavelength. This restriction on the size of h is not an essential limitation of either the transverse element separation or of the analyses we perform. It is, rather, a matter of our not wanting to unnecessarily complicate the form of the rapidly convergent expressions we give by making them independent of the range of kh since in most practical applications the transverse element spacing can be expected to be less than a wavelength. Examples of how the range of kh can be extended can be found in [20, secs. 2 and 3]. Also of interest are the limiting values of the kd–βd equations as $kh \to 2\pi$ since some of the individual terms of the rapidly convergent expressions in the kd–βd equations are singular at $kh = 2\pi$. Closer analysis shows, however, that the singularities of the various terms in the kd–βd equation cancel one another and hence the kd–βd equations remain non-singular at $kh = 2\pi$.

We follow the same procedure for all the arrays considered in this report. We begin as in [27],[29],[20],[21] by assuming the existence of a wave with real propagation constant β traveling from $-\infty$ to $+\infty$ in the direction parallel to the array axis. We are not concerned in any way (other than in Appendix B) with the excitation of the wave. No explicit source for this traveling wave is assumed (even though, of course, the wave cannot exist without some source; see Appendix B). We simply suppose that such a traveling wave supported by the array elements exists and, given that, proceed as follows to find the kd–βd equation expressing βd as a function of kd and the parameters (permittivity, permeability, and packing) of the array elements. The traveling wave excites the array elements which then radiate scattered dipole fields which in turn also serve as excitations for the array elements. (More precisely, the traveling wave is the resultant of the multiplicity of spherical vector dipole waves.) Orthogonality of the vector spherical wave functions and the radially symmetric scatterers assumed, imply that an incident electric (magnetic) dipole field can excite only a scattered electric (magnetic) dipole field [27, p. 6].[9] Additionally, noting that the vector spherical dipole fields are the only multipole vector spherical fields that are non-zero at an element center, an incident electric (magnetic) field at an element center results in a scattered electric (magnetic) dipole field radiated by an elementary electric (magnetic) dipole in the direction of the incident electric (magnetic) field. The coefficient of the scattered electric (magnetic) dipole field is given by the product of the complex electric (magnetic) dipole scattering coefficient and the coefficient of the incident electric (magnetic) dipole field. When the array elements are homogeneous spheres the dipole scattering coefficients are the ordinary Mie electric and magnetic dipole coefficients, given, for example, by [38, sec. 9.25 (10),(11)]. More complicated elements such

[8]For leaky wave antennas (LWA's) formed by periodically placed holes (perforations) in the side of an otherwise uniform closed waveguide, some authors [37] define the real propagation constant β_0 with $\pi \leq \beta_0 d \leq 3\pi$ in the imperforated waveguide as the primary ($n = 0$) Floquet-mode propagation constant (even though it does not describe the variation of the periodic fields outside the perforated waveguide). In that case, our $\Re(\beta d)$ corresponds to their $\beta_0 d - 2\pi$. That is, their $n = -1$ space harmonic for such LWA's equals our $n = 0$ space harmonic (our primary Floquet mode).

[9]The vector spherical wave functions underlying our analysis are given by [29, eqs. (1)-(3)],[27, eqs. (16a,b), eqs. (64),(65)]. In this representation, an electric (magnetic) dipole wave incoming on a sphere has only an electric (magnetic) field at the sphere center.

as coated spheres require appropriate scattering coefficients.[10] We sum the electromagnetic fields incident on a reference element from all the other elements of the array, the summations taking into account all the multiple scattering interactions of the array elements. The field incident on a reference element from all the other elements of the array is called the "interaction field" in the literature [5, ch. 12],[39, sec. 4.5.1].[11] In the case of 2D and 3D arrays we then replace the summations over the indices of the axes transverse to the array axis by expressions obtained in [20] to somewhat increase the rate of convergence of the original summations. At this point we have in effect an equation, containing infinite summations over the index of the array axis, that determines βd as a function of kd and the array element parameters.

When βd is real, these infinite summations converge, but very slowly. However, rapidly convergent expressions can be found for them yielding the kd–βd equation in a form that can be efficiently evaluated and solved. If βd is complex, however, then this final step in the procedure for obtaining the kd-βd equation for traveling waves with real propagation constants supported by periodic arrays of lossless scatterers can no longer be taken because the summations over the index of the array axis diverge. (This apparent paradox of the divergence of these summations from which the complex propagation constants are obtained indirectly is discussed in Appendix B.) Accordingly, following Citrin [41], Koenderink [42], and Alù and Engheta [43], we rewrite the kd–βd equation (containing the divergent summations) in a form that can be analytically continued into the complex βd plane and evaluated for any βd.[12] This equation reduces to the kd–βd equation obtained in our investigations of traveling waves with real propagation constants on lossless arrays when βd is real, and

[10]Because of the symmetry of the array lattice, for traveling waves with the electric and magnetic fields perpendicular to the traveling-wave propagation direction (the array axis), all components of the electric and magnetic fields incident on the center of an element cancel except for an electric and magnetic field perpendicular to each other and to the array axis, and hence the array elements effectively behave as pairs of crossed electric and magnetic dipoles perpendicular to each other and to the direction of propagation of the traveling wave. This should not be understood, however, as meaning that the array elements are in general pairs of crossed electric and magnetic dipoles that are fixed independently of the dipole fields incident on the elements. In this report we will refer to "effective" dipoles to emphasize this. Since our analysis is for waves traveling in the direction of an axis of a rectangular lattice array, it can apply not only to radially symmetric elements with no fixed electric and magnetic dipoles, but also to elements that can only be polarized electrically and magnetically in fixed directions perpendicular to each other. Indeed, we can obtain all our results by replacing the radially symmetric elements with no fixed polarization direction by elements with such fixed polarizability. But physically the two kinds of elements are not at all identical. If the electric and magnetic polarizability directions are fixed independently of the incident dipole fields, then for our analysis to be applicable the induced electric and magnetic dipoles must be uncoupled so that an incident electric (magnetic) field at the element center excites only the electric (magnetic) dipole field.

[11]For 1-D and 2-D arrays, the summations giving the interaction field for real βd converge, the 2-D array summations more slowly than the 1-D summations. For 3-D arrays, however, it is necessary to add a small imaginary part to βd if the summations are to converge rather than oscillate. Additionally, the 3-D interaction field can be viewed as a summation of the contributions from the planes of elements perpendicular to the array axis. The summations over the transverse direction indices to obtain the contributions to the interaction field of these planes of elements converge, but extremely slowly; see the integration analogue in [40, sec. D.2 of Appendix D]. In any event, for all arrays, 1-D, 2-D, and 3-D, direct summation of the scattered dipole fields is completely impractical for obtaining kd–βd diagrams, and hence the conversion of the original summations to rapidly convergent forms is central to the analysis of traveling waves supported by the arrays.

[12]Complex propagation constants β on infinite uniform or periodic waveguides arise from the solution for the fields that are excited by sources illuminating these infinite waveguides. Specifically, the fields along the longitudinal z axis of an infinite waveguide can be expressed as a Fourier transform over real values of β ranging from $-\infty$ to $+\infty$. If this integration along the infinite real β line is evaluated by closing the contour in the complex β plane, the residue contributions from the poles of the integrand represent waves with complex propagation constants β. The poles of this integrand are identical to the zeros of the homogeneous (source-free) transcendental k–β equation obtained for real β and analytically continued into the complex β plane; see Appendix A. Thus, we are able to obtain the complex propagation constants for the complex waves excited by sources illuminating a waveguide from the transcendental equation for the real propagation constants on the source-free waveguide.

enables complex values of βd to be found as a function of kd, kh, and the array element parameters when the array elements are lossy, or when we are in the fast-wave region, $0 < \Re(\beta d) < kd$, (and even in the slow-wave region close to the light line) for 1D and 2D arrays of lossless elements, or when we are in the stop-band regions of 1D, 2D, and 3D arrays of lossless scatterers. Additionally, complex eigenmodes with high attenuation (large $\Im(\beta d)$) can be supported by 1D, 2D, and 3D periodic arrays of lossless scatterers. For 1D arrays, the analytically continuable form of the kd–βd equation is obtained by replacing Clausen functions by polylogarithm functions. For 2D arrays, the analytically continuable form of the kd–βd equation is found by obtaining analytically continuable and rapidly convergent expressions for the Schlömilch series[13] with real βd that arise in the course of converting the summations of the initial form of the kd–βd equation to rapidly convergent forms. This involves a careful choice of branch cuts. Obtaining an analytically continuable form of the kd–βd equation is simplest for the 3D arrays for which all that is necessary is the use of $\cos(\beta d)$ and $\sin(\beta d)$ when βd is complex. Much the same conclusion applies to the 3D alternating two-sphere arrays treated in [22], and the analysis there has been written for complex waves and lossy arrays from the start.

Considerable insight into the analytic continuation procedure, the key step in all the analysis of this report, can be obtained from the analysis performed in Appendix A of waves supported by a 2D slab of magnetodielectric material. In that appendix it is shown that analytically continuing the homogeneous kd–βd equation for real βd into the complex plane, is equivalent to evaluating the Fourier transform expression for the solution of the inhomogeneous slab problem by closing the Fourier transform contour of integration along the real axis in the complex plane and calculating the residues at the zeroes of the integrand. We emphasize that this analytic continuation procedure allows us to find the propagation constants of all the complex waves supported by the arrays, improper as well as proper, without any consideration of the excitation of the waves. Green's functions are not required to find the propagation constants of the complex waves supported by the arrays.

It is important to comment on the procedure used to solve the kd–βd equations for complex βd. In our previous work on traveling waves with real propagation constants, all the kd–βd equations encountered were real functions of the real argument βd and so a simple search procedure with secant algorithm refinement sufficed. In the kd–βd equations encountered here in our extension of our earlier work to traveling waves with complex propagation constants, the equations are complex functions of the complex argument βd and the procedure for solving the equations for βd is necessarily more complicated. Starting with an idea of a relatively large region in the complex βd plane where the zero of the kd–βd equation is thought to lie (this can often be obtained by starting with the kd–βd diagram for the real case), we regard the function of βd, $f(\beta d, kd)$, whose zero we are attempting to find, as a function of the two real variables $\Re(\beta d)$, $\Im(\beta d)$ and vary the real and imaginary parts of βd separately with a relatively coarse grid, to locate the point in the region that gives a minimum value of $|f(\beta d, kd)|$. The search region and grid are then reduced in size and the procedure repeated to obtain a more refined estimate of the zero. The value of βd that minimizes $f(\beta d, kd)$ obtained after several repetitions of this procedure is then used as the starting guess for a quasi-Newton method with a finite-difference gradient [44, Appendix A] implemented in the IMSL subroutine UMINF, or for Müller's Method [45],[46] implemented in the IMSL subroutine ZANLY, to minimize $|f(\beta d, kd)|$ and thereby obtain a highly accurate value for the zero of $f(\beta d, kd)$. It should be noted that it is difficult to be certain that all complex zeroes of the kd–βd equation have been found in a given region of the complex βd plane, so that not all kd–βd curves may be present in the kd–βd diagrams shown in Section 8. A detailed description of a procedure for finding the

[13] Series of the form $\Sigma a_j Z_n(jx)$ where a_j can be a trigonometric function.

complex modes for determining the electromagnetic fields of Hertzian dipoles in layered media is given in [47], but the dispersion equation for this problem is considerably simpler than the equations encountered in our analyses of periodic arrays, and the applicability of the procedure in [47] to our problems is questionable.

The outline of the report is as follows. There are two main parts of the report. The first part, Sections 2 to 7, is devoted to the analysis, and the second part, Section 8, to the numerical results. In Section 2 we derive the kd–βd equations for the complex propagation constants on waves supported by 1D arrays of magnetodielectric spheres, lossless or lossy. Subsection 2.1 treats arrays with the effective electric and magnetic dipoles of the spheres oriented at right angles to each other and to the array axis. Subsection 2.2 considers arrays with the dipoles aligned with the array axis. Since in this case there is no coupling between the electric and magnetic dipoles, this is equivalent to considering 1D arrays of either electric or magnetic dipoles aligned with the array axis.

Section 3 is devoted to the kd–βd equations for the complex propagation constants of waves supported by 2D arrays of lossless or lossy magnetodielectric spheres. Subsection 3.1 deals with arrays with the effective electric and magnetic dipoles of the spheres at right angles to each other and to the array axis. There are two polarizations to be considered. In 3.1.1 the electric dipoles are taken to be in the plane of the array and the magnetic dipoles are perpendicular to the array plane, while in 3.1.2 the electric dipoles are perpendicular to the array plane and the magnetic dipoles are in the plane of the array. The kd–βd equation for this latter polarization can be obtained very simply from the kd–βd equation obtained in 3.1.1. Subsection 3.2 treats 2D arrays with the dipoles parallel to the array axis. Since in this case there is no coupling between the electric and magnetic dipoles, this is equivalent to considering 2D arrays of either electric or magnetic dipoles, with the dipoles parallel to the array axis.

In Section 4 we obtain the kd–βd equations that determine the complex propagation constants of traveling waves on 3D arrays of lossless or lossy magnetodielectric spheres. In Subsection 4.1 the effective electric and magnetic dipoles of the spheres are assumed to be perpendicular to each other and to the array axis, while in Subsection 4.2 the electric and magnetic dipoles are assumed to be parallel to the array axis. Since in this case there is no coupling between the electric and magnetic dipoles, this is equivalent to considering 3D arrays of either electric dipoles or magnetic dipoles, with the dipoles parallel to the array axis.

In Section 5 we obtain expressions for the effective constitutive parameters of a 3D cubic-lattice array regarded as a homogeneous medium, assuming that both $|\beta d| \ll 1$ and $kd \ll 1$ with β the propagation constant of a transverse wave supported by the array. Two such expressions are obtained, one from solving the kd–βd equation, and the other given by the Clausius-Mossotti relations.

Section 6 deals with partially finite 3D arrays, arrays that are finite in the direction of the array axis and infinite in the transverse directions. We consider the field excited by a plane wave in the direction of the array axis, incident from free space on a 3D partially finite periodic array of lossless or lossy magnetodielectric spheres with dipoles perpendicular to the array axis, and on a 3D partially finite periodic array of lossless or lossy electric or magnetic dipoles oriented parallel to the array axis. Previously obtained expressions for lossless dipoles are shown to be equally valid for partially finite arrays of lossy dipoles.

In Section 7 we discuss issues related to the bidirectionality and complex conjugates of waves supported by periodic arrays of lossless magnetodielectric inclusions. It is shown, consistent with [36], that if βd is a solution of a kd–βd equation, then so are $-\beta d$, $(\beta d)^*$, and $-(\beta d)^*$. However, for 1D and 2D arrays it may be necessary to choose alternative branches of the multivalued functions that appear in the kd–βd equation if $(\beta d)^*$ and $-(\beta d)^*$ are to satisfy the same kd–βd equation satisfied by βd and $-\beta d$.

Section 8 is devoted to presenting and discussing numerous kd–βd diagrams for 1D, 2D, and 3D periodic arrays of magnetodielectric spheres with equal permittivity and permeability, diamond spheres, and silver nanospheres.

Appendix A contains an analysis of complex waves on a 2D slab of magnetodielectric material above a ground plane. Even though the slab is a continuous structure and not periodic, considerable insight into several of the major issues of this report can be obtained by careful examination of the slab problem: 1) the derivation of the kd–βd equations for complex β by analytically continuing the corresponding kd–βd equations for real β; 2) the necessity of evaluating the multivalued functions that appear in the kd–βd equations for 1D and 2D arrays using branches other than the principal one if $(\beta d)^*$ is to always be a solution to the same dispersion equation as βd if the array elements are lossless; and 3) the divergence of the complex-wave fields obtained by direct summation of the fields scattered from the array dipoles. Appendix B is devoted to a discussion of the divergence of complex-wave fields obtained by direct summation of dipole fields of periodic arrays. Although the primary purpose of this report is to derive and solve dispersion equations for waves in the direction of the array axis with complex propagation constants, such waves have associated complex propagation constants in the direction (directions) transverse to the array axis. Accordingly, in Appendix C we present a general discussion of complex waves on uniform and periodic waveguides, and of the distinguishing features of fast and slow waves.

In closing this introduction, we briefly discuss some work related to ours.[14] Important mention should be made of J. Brown's 1960 article [4] and R.E. Collin's chapter on artificial dielectrics [5, ch. 12] consisting of periodic arrays of elements such as perfectly conducting spheres and disks. Although arrived at independently of Brown and Collin, our work can be seen as a major extension of their work to a full-wave analysis of time-harmonic dipole fields on periodic arrays of magnetodielectric elements. Although Brown's and Collin's treatment is almost completely restricted to static fields, the way they obtain the effective dielectric constants of artificial dielectrics via the interaction field, followed by an attempt to transform the interaction field summation to a rapidly convergent form, parallels our method of obtaining the propagation constants of traveling waves supported by periodic arrays. Simovski and He [48] analyzed a rectangular array of lossless, isotropic elements consisting of six Ω particles on the faces of a cubic unit cell. Their procedure for obtaining the dispersion equation for the eigenmodes of this rectangular lattice and for obtaining the effective parameters of a cubic lattice of the unit cells from the solution to the dispersion equation, is virtually identical to the procedure we developed independently in [20],[21] and extend

[14] Despite its title and its emphasis on the homogeneous solution for the propagation constants of waves on periodic structures, L. Brillouin's classic book [49] has very little if any similarity or applicability to our work. It is concerned for the most part with mechanical rather than electromagnetic interactions of particles, and with small periodic perturbations of continuous media. However, its discussion of non-rectangular lattices, as well as of propagation in arbitrary directions through periodic arrays may prove to be of interest in possible extensions of our own work at a later time. Although it might be thought that the well-established science of crystallography, the science of determining the arrangement of atoms in solids, with its focus on periodic lattices of atoms would have an important bearing on our work, that is not the case. The important use of X-ray diffraction techniques in crystallography to determine crystal structures is unrelated to the propagation of electromagnetic waves through periodic arrays that is the focus of our work. In X-ray diffraction each atom of a crystal scatters the wave fronts of the incoming wave as they arrive and so becomes surrounded by a series of scalar spherical wavelets whose interference or reinforcement with the spherical wavelets from the other atoms gives rise to a diffraction pattern which can then be related to the crystal's structure [50]. Crystal optics, the branch of optics treating the behavior of light in anisotropic media, has important applications to understanding and analyzing spatial dispersion: the dependence of the electric and magnetic susceptibility of media such as crystals on the propagation direction of light in the media [51]. Since the analysis of 3D arrays in this report focuses on axial propagation and the conditions under which the effective parameters derived from the solution of the axial propagation dispersion equations can characterize the arrays viewed as isotropic media, spatial dispersion is barely touched on here. However, spatial dispersion is in general an extremely important topic in treatments of metamaterials, and it will be the subject of forthcoming work.

here to lossy scatterers and complex waves. The principal difference between their work and ours in [20],[21] is that they obtain the dispersion equation using an approximate method for evaluating the infinite summations in the interaction field, whereas we use an exact, closed-form expression for these summations. The work of S. Tretyakov, especially [39, sec. 4.5, sec. 5.6], has been discussed at some length in [20],[21]. Little needs to be added to that discussion here since Tretyakov does not treat complex waves (although there is nothing in his formalism to prevent that), the principal subject of this report, or periodic arrays of magnetodielectric inclusions. The work of Alù and Engheta, in particular [43], has a very strong family resemblance to our own and has been acknowledged above in connection with the analytic continuation procedure to obtain complex waves that plays a central role in the analysis of this report. The focus of their work is somewhat different from ours, however. Alù and Engheta are primarily concerned with propagation along chains of small lossy or lossless electrically-polarizable particles, not necessarily spheres, rather than chains of magnetodielectric particles, and do not consider 2D and 3D arrays. Rather than emphasize the dependence of the propagation constant on "frequency" as we do, they investigate how the properties of the propagating mode supported by the chain depend on the polarizability of the particles. This enables them to delineate regimes for leaky-modes and guided-modes that are applicable to small polarizable particles of any shape, so that their work establishes the basis for using particle shape as a design variable if desired. Although not specifically concerned with traveling waves on periodic arrays of discrete scatterers, A. Hessel's in-depth mathematically-oriented treatment of guided waves and traveling wave antennas in [52, ch. 10] is an excellent reference on the general subject. Whereas our focus is almost exclusively on the longitudinal characteristics of the traveling waves that we investigate, Hessel's treatment deals with the properties of traveling waves in all directions, transverse as well as longitudinal, and in so doing establishes the foundation for understanding the waves in terms of their complex-plane representations, something that we touch on only briefly in Appendices A and C. The book on traveling wave antennas by Walter [53] has some useful basic information on fast and slow waves, and an extensive treatment of their antenna applications. Finally, reference should be made here to photonic crystals. Photonic crystals are optical artificial periodic dielectrics whose micro-structure has been engineered to control the properties (propagation, transmission, reflection, band gaps, etc.) of light incident on the crystals [6]–[8]. Although the analysis of photonic crystals by casting Maxwell's equations in the form of eigenequations that are solved computer-numerically by sophisticated discretization schemes [7],[8] is very different from our analysis of periodic arrays, the generality of photonic crystal analysis can yield important insights into matters of common interest such as the structure of dispersion diagrams.

2 1D ARRAYS

In this section we investigate waves with complex propagation constants supported by 1D periodic arrays of lossless and lossy magnetodielectric spheres. In Subsection 2.1 it is assumed that the spheres can be modeled by pairs of crossed electric and magnetic dipoles. In Subsection 2.2 we consider traveling waves supported by 1D periodic arrays of lossless and lossy magnetodielectric spheres with the dipole axes aligned parallel with the array axis. This reduces simply to traveling waves supported by a 1D array of either electric or magnetic dipoles aligned with the array axis because an electric (magnetic) dipole has no radial or longitudinal magnetic (electric) field [38, secs. 8.5, 8.6] and so there is no coupling of the electric dipoles with the magnetic dipoles of arrays with both the electric and magnetic dipoles aligned with the array axis. (For the same reason it is unnecessary to consider 1D arrays of electric and magnetic dipoles with the electric (magnetic)

dipoles in the direction of the array axis and the magnetic (electric) dipoles perpendicular to the array axis.)

2.1 ELECTRIC AND MAGNETIC DIPOLES PERPENDICULAR TO THE ARRAY AXIS

In this subsection we investigate the complex propagation constants of traveling waves supported by 1D periodic arrays of lossless and lossy magnetodielectric spheres. It is assumed that the spheres can be modeled by pairs of crossed electric and magnetic dipoles perpendicular to each other, and that a spherical electromagnetic dipole field incident on a sphere will excite an electric (magnetic) dipole proportional to, and in the direction of, the electric (magnetic) field at the sphere center. As noted in the Introduction, although we refer in this and the following sections of the report as "magnetodielectric spheres," and assume that the spheres are homogeneous, the analyses that we perform apply equally well to any radially symmetric array elements or to elements that can be modeled as a pair of electric and magnetic dipoles at right angles to each other and the traveling wave direction provided that the dipoles are uncoupled and that an incident electric (magnetic) field at the element center in the direction of the electric (magnetic) dipole excites only the electric (magnetic) dipole field. The radius of the spheres is denoted by a, and the relative permittivity and permeability of the spheres are denoted by ϵ_r and μ_r, respectively, where ϵ_r and μ_r are in general complex. We denote the separation between the centers of adjacent spheres by d, take the z axis to be the axis of the array, and assume an excitation of the array with an x-directed electric field and a y-directed magnetic field. We begin in exactly the same way as we did in our analysis of traveling waves with real propagation constants supported by 1D periodic arrays of lossless spheres [27] by obtaining expressions for the x-directed electric field and the y-directed magnetic field at the center of the reference sphere at $z = 0$ resulting from the electric and magnetic fields scattered from all the other spheres in the array.[15] In so doing we make use of the scattering equations [27, eq. 31]

$$b_{e,n} = S_e \, E_{0x}^{0n} \tag{2.1a}$$

$$b_{m,n} = S_m \, \frac{H_{0y}^{0n}}{Y_0}. \tag{2.1b}$$

that relate the coefficients $b_{e,n}$ ($b_{m,n}$) of the electric (magnetic) dipole waves scattered from the nth sphere to the incident electric (magnetic field) $E_{0x}^{0n}\,\hat{\mathbf{x}}$ ($H_{0y}^{0n}/Y_0\,\hat{\mathbf{y}}$) at the center of the nth sphere. In (2.1) S_e (S_m) is the normalized magnetodielectric sphere electric (magnetic) dipole scattering coefficient. "Normalized" means that $b_{e,n}$ ($b_{m,n}$) is the coefficient of $\exp(ikr)/(kr)$ in the outgoing electric (magnetic) dipole field in response to the incident field $E_{0x}^{0n}\,\hat{\mathbf{x}}$ ($H_{0y}^{0n}/Y_0\,\hat{\mathbf{y}}$) at the center of

[15] All other components cancel because of the symmetry of the array lattice.

the x- (y-) directed electric (magnetic) dipole.[16] We then obtain the following equations

$$(kd)^3 = S_e\Bigg[\sum_{n=1}^{\infty}\left(\frac{\mathrm{e}^{\mathrm{i}(k+\beta)dn}+\mathrm{e}^{-\mathrm{i}(\beta-k)dn}}{n}\right)\left((kd)^2+\frac{\mathrm{i}kd}{n}-\frac{1}{n^2}\right)$$

$$+\,q\,(kd)\sum_{n=1}^{\infty}\left(\frac{\mathrm{e}^{\mathrm{i}(k+\beta)dn}-\mathrm{e}^{-\mathrm{i}(\beta-k)dn}}{n}\right)\left(kd+\frac{\mathrm{i}}{n}\right)\Bigg] \tag{2.2a}$$

and

$$(kd)^3 = S_m\Bigg[\sum_{n=1}^{\infty}\left(\frac{\mathrm{e}^{\mathrm{i}(k+\beta)dn}+\mathrm{e}^{-\mathrm{i}(\beta-k)dn}}{n}\right)\left((kd)^2+\frac{\mathrm{i}kd}{n}-\frac{1}{n^2}\right)$$

$$+\,\frac{1}{q}\,(kd)\sum_{n=1}^{\infty}\left(\frac{\mathrm{e}^{\mathrm{i}(k+\beta)dn}-\mathrm{e}^{-\mathrm{i}(\beta-k)dn}}{n}\right)\left(kd+\frac{\mathrm{i}}{n}\right)\Bigg] \tag{2.2b}$$

where

$$q = \frac{b_{m,0}}{b_{e,0}}. \tag{2.3}$$

In (2.2) β is the real propagation constant of the wave supported by the array.

In the procedure we followed in our analysis of traveling waves with real propagation constants supported by lossless spheres we were able to obtain closed-form expressions for the summations in (2.2). For complex β this is no longer possible as in fact the summations diverge. Accordingly, we rewrite (2.2) in a form that gives the same result for real β as that obtained in [27] but which can be analytically continued into the complex β plane.[17] To do this we introduce the polylogarithm functions [54],[55]

$$\mathrm{Li}_N(z) = \sum_{k=1}^{\infty}\frac{z^k}{k^N}, \quad |z|<1 \tag{2.4}$$

which can be analytically continued into the complex z plane by means of the iterative equations

$$\mathrm{Li}_N(z) = \int_0^z \frac{\mathrm{Li}_{N-1}(t)}{t}\mathrm{d}t \tag{2.5a}$$

and

$$\mathrm{Li}_1(z) = -\ln(1-z)\ . \tag{2.5b}$$

[16] As we noted at the beginning of this section of the report, although we refer to the array elements as "magnetodielectric spheres," our analysis applies equally well to any array elements that can be modeled as a pair of crossed electric and magnetic dipoles such that an incident electric (magnetic) field in the direction of the electric (magnetic) dipole excites only the electric (magnetic) dipole field. If the array elements are homogeneous spheres then S_e and S_m are the normalized Mie dipole scattering coefficients [27, eqs. 30a,b],

$$S_e = -\mathrm{i}\frac{3}{2}b_1^{\mathrm{sc}}, \quad S_m = -\mathrm{i}\frac{3}{2}a_1^{\mathrm{sc}}$$

where b_1^{sc} and a_1^{sc} are the electric and magnetic Mie dipole scattering coefficients defined in Stratton [38, sec. 9.25, eqs. 11, 10]. If the array elements are not homogeneous magnetodielectric spheres then S_e and S_m must be known for the results of this and the following sections of the report to be applied.

[17] In Appendix A we justify this procedure by treating the problem of determining the complex waves that can be supported by a two-dimensional slab of magnetodielectric material over a perfectly conducting ground plane. Although this problem involves a continuous rather than a discrete periodic structure, the essential features of the continuous and discrete periodic problems are identical.

Efficient algorithms exist for calculating $\mathrm{Li}_N(z)$ for any complex z (see, for example, [56]). We also introduce the notation

$$F_{N+}(kd,\beta d) = \mathrm{Li}_N\left(\mathrm{e}^{\mathrm{i}(k+\beta)d}\right) + \mathrm{Li}_N\left(\mathrm{e}^{-\mathrm{i}(\beta-k)d}\right) \tag{2.6a}$$

$$F_{N-}(kd,\beta d) = \mathrm{Li}_N\left(\mathrm{e}^{\mathrm{i}(k+\beta)d}\right) - \mathrm{Li}_N\left(\mathrm{e}^{-\mathrm{i}(\beta-k)d}\right) . \tag{2.6b}$$

Then the kd–βd equations (2.2) can be written as

$$\begin{aligned}(kd)^3 = S_e\Big[&(kd)^2F_{1+}(kd,\beta d) + \mathrm{i}\,kdF_{2+}(kd,\beta d) - F_{3+}(kd,\beta d)\\ &+ q\,kd\Big(kdF_{1-}(kd,\beta d) + \mathrm{i}F_{2-}(kd,\beta d)\Big)\Big]\end{aligned} \tag{2.7a}$$

$$\begin{aligned}(kd)^3 = S_m\Big[&(kd)^2F_{1+}(kd,\beta d) + \mathrm{i}\,kdF_{2+}(kd,\beta d) - F_{3+}(kd,\beta d)\\ &+ \frac{1}{q}\,kd\Big(kdF_{1-}(kd,\beta d) + \mathrm{i}F_{2-}(kd,\beta d)\Big)\Big] .\end{aligned} \tag{2.7b}$$

Letting

$$\Sigma_1 = (kd)^2F_{1+}(kd,\beta d) + \mathrm{i}\,kdF_{2+}(kd,\beta d) - F_{3+}(kd,\beta d) \tag{2.8a}$$

and

$$\Sigma_2 = kd\Big(kdF_{1-}(kd,\beta d) + \mathrm{i}\,F_{2-}(kd,\beta d)\Big) \tag{2.8b}$$

in (2.7) and eliminating q we obtain the kd–βd equation

$$\frac{(kd)^3 - S_e\Sigma_1}{S_e\Sigma_2} = \frac{S_m\Sigma_2}{(kd)^3 - S_m\Sigma_1}. \tag{2.9}$$

As a special case of the kd–βd equation (2.9) for a 1D periodic array of lossless or lossy magnetodielectric spheres we can obtain the kd–βd equation for a 1D periodic array of electric or magnetic dipoles perpendicular to the array axis

$$(kd)^3 = S\Sigma_1 \tag{2.10}$$

where S is the normalized scattering coefficient of either the electric or the magnetic dipoles.

Using the basic mathematical relation that the sum of logarithms equals the logarithm of the corresponding product, an alternative expression for $F_{1+}(kd,\beta d)$ can be obtained from (2.6a) with $N = 1$,

$$F_{1+}(kd,\beta d) = -\mathrm{i}kd - \ln[2(\cos kd - \cos\beta d)] . \tag{2.11}$$

This expression is not equivalent to (2.6a) because the branch cuts of (2.6a) with $N = 1$ in the complex βd plane run from kd to $kd + \mathrm{i}\infty$ and from $-kd$ to $-kd - \mathrm{i}\infty$, whereas the branch cuts of (2.11) run from kd to 0 on top of the real βd axis and then to $\mathrm{i}\infty$ along the imaginary βd axis, and from $-kd$ to 0 below the real βd axis and then to $-\mathrm{i}\infty$ along the imaginary βd axis (see Fig. 1). As a result, in the regions 1 and 3 of the complex βd plane in Fig. 1, the imaginary part of $F_{1+}(kd,\beta d)$ given by (2.6a) is 2π greater than the value obtained with (2.11).

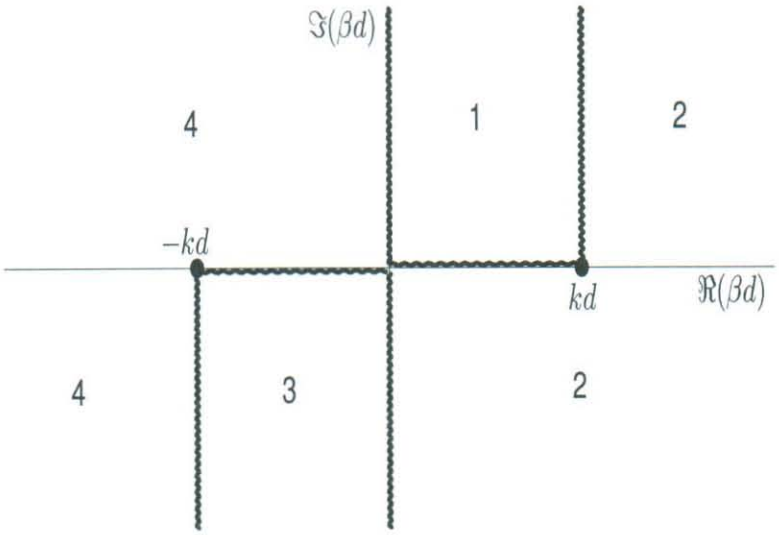

Figure 1: Branch cuts in the complex βd plane for the two alternative expressions for $F_{1+}(kd, \beta d)$.

2.2 DIPOLES PARALLEL TO THE ARRAY AXIS

In this subsection we consider the complex propagation constants of traveling waves on 1D periodic arrays of lossless and lossy magnetodielectric spheres with the dipoles parallel to the array axis. As noted in the introduction to this section, we need only consider 1D arrays of electric (or magnetic dipoles) separately since there is no coupling between the electric and magnetic dipoles. Our starting point is the kd–βd equation for real βd [26, eq. 94]

$$(kd)^3 = 2S \sum_{n=1}^{\infty} \left[\frac{\mathrm{e}^{\mathrm{i}(k+\beta)dn} + \mathrm{e}^{-\mathrm{i}(\beta-k)dn}}{n^2} \right] \left(-kd\mathrm{i} + \frac{1}{n} \right) \tag{2.12}$$

where S is the normalized dipole scattering coefficient. Instead of obtaining closed-form expressions for the summations as we did in [26] we rewrite (2.12) in terms of polylogarithm functions so that the kd-βd equation can be analytically continued into the complex βd plane

$$(kd)^3 = 2S \left[-kd\mathrm{i} F_{2+}(kd, \beta d) + F_{3+}(kd, \beta d) \right] \tag{2.13}$$

where $F_{2+}(kd, \beta d)$ and $F_{3+}(kd, \beta d)$ are defined by (2.6a), thereby obtaining the desired kd–βd equation for obtaining the normalized complex propagation constants βd.

3 2D ARRAYS

In this section we consider traveling waves supported by 2D periodic arrays of lossless and lossy magnetodielectric spheres. In Subsection 3.1 it is assumed that the spheres can be effectively modeled by pairs of crossed electric and magnetic dipoles, each of the dipoles perpendicular to the array axis. There are two polarizations of the electric dipoles to be considered, one where the

dipoles are in the array plane determined by the sphere centers and array axis, and the other where the dipoles are perpendicular to the array plane. These two polarizations are treated in 3.1.1 and 3.1.2, respectively. Since the electric and magnetic dipoles of one polarization are, apart from a sign change, the magnetic and electric dipoles, respectively, of the other polarization, the kd–βd equation for the polarization in which the electric dipoles are perpendicular to the array plane can be obtained very simply from the kd–βd equation for the polarization in which the electric dipoles are in the array plane. In Subsection 3.2 we consider traveling waves supported by 2D periodic arrays of lossless and lossy magnetodielectric spheres with the dipole axes aligned parallel with the array axis. This reduces simply to traveling waves supported by a 2D array of either electric or magnetic dipoles aligned with the array axis because an electric (magnetic) dipole has no radial or longitudinal magnetic (electric) field [38, secs. 8.5, 8.6] and so there is no coupling of the electric dipoles with the magnetic dipoles of arrays with both electric and magnetic dipoles aligned with the array axis. (For the same reason it is unnecessary to consider 2D arrays of electric and magnetic dipoles with the electric (magnetic) dipoles in the direction of the array axis and the magnetic (electric) dipoles perpendicular to the array axis.)

3.1 ELECTRIC AND MAGNETIC DIPOLES PERPENDICULAR TO THE ARRAY AXIS

3.1.1 ELECTRIC DIPOLES IN THE ARRAY PLANE

We choose the array axis to be the z axis of a Cartesian coordinate system with equispaced columns of magnetodielectric spheres parallel to the x axis located at $z = nd, n = 0, \pm 1, \pm 2, \cdots$. In each column the spheres are centered at $x = mh, m = 0, \pm 1, \pm 2, \cdots$. The effective electric and magnetic dipole components of each sphere are oriented in the x and y direction, respectively, so that the electric dipoles lie in the xz plane, the array plane. We assume an excitation of the array with the electric field parallel to the x axis and the magnetic field parallel to the y axis, and such that all the spheres in any column of the array are excited identically.

Our starting point is the pair of equations [20, eqs. 8.22a,b] obtained by expressing the electric and magnetic field at the center of the reference sphere at $x = 0, y = 0, z = 0$ as the sum of the electric and magnetic fields scattered from all the other elements of the array,

$$(kh)^3 = S_e \Bigg\{ \sum_{\substack{n=-\infty \\ n\neq 0}}^{\infty} \mathrm{e}^{\mathrm{i}n\beta d} \Bigg(\sum_{m=-\infty}^{\infty} \frac{\mathrm{e}^{\mathrm{i}kh\rho_{mn}}}{\rho_{mn}} \Bigg[\frac{-2\mathrm{i}}{\rho_{mn}} \left(kh + \frac{\mathrm{i}}{\rho_{mn}} \right) \frac{m^2}{\rho_{mn}^2} + \left((kh)^2 + \frac{\mathrm{i}kh}{\rho_{mn}} - \frac{1}{\rho_{mn}^2} \right) \frac{(nd/h)^2}{\rho_{mn}^2} \Bigg] - q \sum_{m=-\infty}^{\infty} \frac{\mathrm{e}^{\mathrm{i}kh\rho_{mn}}}{\rho_{mn}} \left((kh)^2 + \frac{\mathrm{i}kh}{\rho_{mn}} \right) \frac{nd/h}{\rho_{mn}} \Bigg) - 4\mathrm{i} \sum_{m=1}^{\infty} \frac{\mathrm{e}^{\mathrm{i}kh\rho_{m0}}}{\rho_{m0}^2} \left(kh + \frac{\mathrm{i}}{\rho_{m0}} \right) \Bigg\} \tag{3.1a}$$

and

$$(kh)^3 = S_m \Bigg\{ \sum_{\substack{n=-\infty \\ n\neq 0}}^{\infty} \mathrm{e}^{\mathrm{i}n\beta d} \Bigg[\sum_{m=-\infty}^{\infty} \frac{\mathrm{e}^{\mathrm{i}kh\rho_{mn}}}{\rho_{mn}} \left((kh)^2 + \frac{\mathrm{i}kh}{\rho_{mn}} - \frac{1}{\rho_{mn}^2} \right) - \frac{1}{q} \sum_{m=-\infty}^{\infty} \frac{\mathrm{e}^{\mathrm{i}kh\rho_{mn}}}{\rho_{mn}} \left((kh)^2 + \frac{\mathrm{i}kh}{\rho_{mn}} \right) \frac{nd/h}{\rho_{mn}} \Bigg]$$

$$+ 2 \sum_{m=1}^{\infty} \frac{\mathrm{e}^{\mathrm{i}kh\rho_{m0}}}{\rho_{m0}} \left((kh)^2 + \frac{\mathrm{i}kh}{\rho_{m0}} - \frac{1}{\rho_{m0}^2} \right) \Bigg\} \tag{3.1b}$$

where

$$\rho_{mn} = \sqrt{m^2 + (nd/h)^2} \tag{3.2}$$

$$\rho_{m0} = m \tag{3.3}$$

and S_e, S_m, and q are as in Section 2. Continuing just as we did when the normalized propagation constant βd is real, from [20, eq. 8.25]

$$\begin{aligned} \sum_{\substack{n=-\infty \\ n\neq 0}}^{\infty} \mathrm{e}^{\mathrm{i}n\beta d} \sum_{m=-\infty}^{\infty} \frac{\mathrm{e}^{\mathrm{i}kh\rho_{mn}}}{\rho_{mn}} \Bigg[& \frac{-2\mathrm{i}}{\rho_{mn}} \left(kh + \frac{\mathrm{i}}{\rho_{mn}} \right) \frac{m^2}{\rho_{mn}^2} \\ & + \left((kh)^2 + \frac{\mathrm{i}kh}{\rho_{mn}} - \frac{1}{\rho_{mn}^2} \right) \frac{(nd/h)^2}{\rho_{mn}^2} \Bigg] \\ = 2 \sum_{n=1}^{\infty} \cos(n\beta d) \Bigg[& \mathrm{i}\pi (kh)^2 H_0^{(1)}(nkd) \\ - 4 \sum_{m=1}^{\infty} & \left[(2\pi m)^2 - (kh)^2 \right] K_0 \left(n(d/h) \sqrt{(2\pi m)^2 - (kh)^2} \right) \Bigg] \end{aligned} \tag{3.4}$$

from [20, eq. 8.29]

$$\begin{aligned} \sum_{\substack{n=-\infty \\ n\neq 0}}^{\infty} \mathrm{e}^{\mathrm{i}n\beta d} \sum_{m=-\infty}^{\infty} \frac{\mathrm{e}^{\mathrm{i}kh\rho_{mn}}}{\rho_{mn}} & \left((kh)^2 + \frac{\mathrm{i}kh}{\rho_{mn}} \right) \frac{nd/h}{\rho_{mn}} \\ = \sum_{n=1}^{\infty} 2\mathrm{i} \sin(n\beta d) \Bigg(& - \pi (kh)^2 H_1^{(1)}(nkd) \\ + 4\mathrm{i}(kh) \sum_{m=1}^{\infty} & \sqrt{(2\pi m)^2 - (kh)^2}\, K_1 \left(n(d/h) \sqrt{(2\pi m)^2 - (kh)^2} \right) \Bigg) \end{aligned} \tag{3.5}$$

from [20, eq. 8.32]

$$\begin{aligned} \sum_{\substack{n=-\infty \\ n\neq 0}}^{\infty} \mathrm{e}^{\mathrm{i}n\beta d} \sum_{m=-\infty}^{\infty} \frac{\mathrm{e}^{\mathrm{i}kh\rho_{mn}}}{\rho_{mn}} & \left((kh)^2 + \frac{\mathrm{i}kh}{\rho_{mn}} - \frac{1}{\rho_{mn}^2} \right) \\ = 2 \sum_{n=1}^{\infty} \cos(n\beta d) \Bigg\{ & \frac{\mathrm{i}\pi (kh)^2}{2} \left[H_0^{(1)}(nkd) - H_2^{(1)}(nkd) \right] \\ + 2 \sum_{m=1}^{\infty} \Bigg[& \left[(2\pi m)^2 + (kh)^2 \right] K_0 \left(n(d/h) \sqrt{(2\pi m)^2 - (kh)^2} \right) \\ - & \left[(2\pi m)^2 - (kh)^2 \right] K_2 \left(n(d/h) \sqrt{(2\pi m)^2 - (kh)^2} \right) \Bigg] \Bigg\} \end{aligned} \tag{3.6}$$

from [20, eq. 8.33]

$$4\sum_{m=1}^{\infty}\frac{\mathrm{e}^{\mathrm{i}khm}}{m}\frac{-\mathrm{i}}{m}\left(kh+\frac{\mathrm{i}}{m}\right)=4\;kh\;\mathrm{Cl}_2(kh)+4\;\mathrm{Cl}_3(kh)+\mathrm{i}\pi(kh)^2-\mathrm{i}\frac{2}{3}(kh)^3 \tag{3.7}$$

and from [20, eq. 8.36]

$$\begin{aligned}&2\sum_{m=1}^{\infty}\frac{\mathrm{e}^{\mathrm{i}khm}}{m}\left((kh)^2+\frac{\mathrm{i}kh}{m}-\frac{1}{m^2}\right)\\&=-2\left((kh)^2\ln\left[2\sin\left(\frac{kh}{2}\right)\right]+kh\mathrm{Cl}_2(kh)+\mathrm{Cl}_3(kh)\right)+\mathrm{i}\left[\frac{\pi}{2}(kh)^2-\frac{2}{3}(kh)^3\right]\end{aligned} \tag{3.8}$$

for $0<kh<2\pi$. In (3.4)-(3.8), $H_n^{(1)}$ is the Hankel function of the first kind of order n, K_n is the modified Bessel function of order n, and the Clausen functions $\mathrm{Cl}_2(kh)$ and $\mathrm{Cl}_3(kh)$ are defined and given by [54]

$$\mathrm{Cl}_2(a)\equiv\sum_{n=1}^{\infty}\frac{\sin na}{n^2}=\frac{1}{2\mathrm{i}}\left(\mathrm{Li}_2(\mathrm{e}^{\mathrm{i}a})-\mathrm{Li}_2(\mathrm{e}^{-\mathrm{i}a})\right),\quad 0<a\le\pi \tag{3.9a}$$

$$\mathrm{Cl}_2(a)=-\mathrm{Cl}_2(2\pi-a),\quad \pi\le a<2\pi \tag{3.9b}$$

$$\mathrm{Cl}_3(a)\equiv\sum_{n=1}^{\infty}\frac{\cos na}{n^3}=\frac{1}{2}\left(\mathrm{Li}_3(\mathrm{e}^{\mathrm{i}a})+\mathrm{Li}_3(\mathrm{e}^{-\mathrm{i}a})\right),\quad 0<a<\pi \tag{3.9c}$$

$$\mathrm{Cl}_3(a)=\mathrm{Cl}_3(2\pi-a),\quad \pi\le a<2\pi \tag{3.9d}$$

with the dilogarithm and trilogarithm functions, Li_2 and Li_3, given by (2.4) and (2.5).

To obtain analytically continuable and rapidly convergent expressions for the Schlömilch series

$$\sum_{n=1}^{\infty}\cos(n\beta d)H_0^{(1)}(nkd),\ \sin(n\beta d)H_1^{(1)}(nkd),\ \sum_{n=1}^{\infty}\cos(n\beta d)H_2^{(1)}(nkd) \tag{3.10}$$

in (3.4), (3.5), and (3.6), following Linton [57] we introduce the notation

$$\cos(\psi_m)=\beta_m=\frac{\beta d+2m\pi}{kd} \tag{3.11}$$

$$\sin(\psi_m)=\mathrm{i}\sqrt{\beta_m^2-1}\,. \tag{3.12}$$

We choose the branch cuts of $\sqrt{\beta_m^2-1}$ in the complex β_m plane to run from 1 to $1+\mathrm{i}\infty$ and from -1 to $-1-\mathrm{i}\infty$ with the appropriate branch of $\sqrt{\beta_m^2-1}$ defined by

$$-\frac{3\pi}{2}<\arg(\beta_m-1)\le\frac{\pi}{2},\quad -\frac{\pi}{2}\le\arg(\beta_m+1)<\frac{3\pi}{2}\,. \tag{3.13}$$

Then from [57, eq. 22]

$$\sum_{n=1}^{\infty}\cos(n\beta d)H_0^{(1)}(nkd)=-\frac{1}{2}-\frac{\mathrm{i}}{\pi}\left(\gamma+\ln\frac{kd}{4\pi}\right)+\frac{1}{\mathrm{i}kd\sqrt{\beta_0^2-1}}$$

$$+\sum_{m=1}^{\infty}\left(\frac{1}{\mathrm{i}kd\sqrt{\beta_m^2-1}}+\frac{1}{\mathrm{i}kd\sqrt{\beta_{-m}^2-1}}+\frac{\mathrm{i}}{\pi m}\right) \tag{3.14}$$

from [57, eq. 43]

$$\sum_{n=1}^{\infty}\sin(n\beta d)H_1^{(1)}(nkd)=\frac{\beta_0}{\mathrm{i}\sqrt{\beta_0^2-1}}+\frac{1}{kd}\sum_{m=1}^{\infty}\left(\frac{\beta_m}{\mathrm{i}kd\sqrt{\beta_m^2-1}}+\frac{\beta_{-m}}{\mathrm{i}kd\sqrt{\beta_{-m}^2-1}}\right)+\frac{\mathrm{i}}{\pi}\frac{\beta d}{kd} \tag{3.15}$$

and from [57, eq. 42]

$$\sum_{n=1}^{\infty}\cos(n\beta d)H_2^{(1)}(nkd)=-\frac{2\beta_0^2-1}{kd\mathrm{i}\sqrt{\beta_0^2-1}}-\frac{2\mathrm{i}\beta_0}{kd}-\frac{1}{kd}\sum_{m=1}^{\infty}\left(\frac{2\beta_m^2-1}{\mathrm{i}\sqrt{\beta_m^2-1}}+\frac{2\beta_{-m}^2-1}{\mathrm{i}\sqrt{\beta_{-m}^2-1}}+\frac{\mathrm{i}8m\pi}{kd}\right)+\lambda_2 \tag{3.16}$$

where γ, referred to as C in [58], is the Euler constant [59, Table 1.1],

$$\gamma=0.5772156649\cdots \tag{3.17}$$

and

$$\lambda_2=\frac{1}{2\pi}\left[B_0\left(\frac{\beta d}{2\pi}\right)-2\left(\frac{2\pi}{kd}\right)^2 B_2\left(\frac{\beta d}{2\pi}\right)\right] \tag{3.18}$$

with B_0 and B_2 the Bernoulli polynomials [58, eq. 9.62]

$$B_0(x)=1,\quad B_2(x)=x^2-x+\frac{1}{6}\,. \tag{3.19}$$

Truncating the series on the RHS of (3.14)-(3.16) at $m=10$ gives sufficient accuracy. Substituting (3.4)-(3.8) in (3.1) and eliminating q from (3.1a) and (3.1b) we obtain the kd–βd equation

$$\frac{(kh)^3-S_e\Sigma_1}{S_e\Sigma_2}=\frac{S_m\Sigma_2}{(kh)^3-S_m\Sigma_3}\,. \tag{3.20}$$

where

$$\begin{aligned}\Sigma_1 &= 2\pi\mathrm{i}(kh)^2\sum_{n=1}^{\infty}\cos(n\beta d)H_0^{(1)}(nkd)\\ &-8\sum_{n=1}^{\infty}\cos(n\beta d)\sum_{m=1}^{\infty}\left[(2\pi m)^2-(kh)^2\right]K_0\left(n(d/h)\sqrt{(2\pi m)^2-(kh)^2}\right)\\ &+4\,kh\,\mathrm{Cl}_2(kh)+4\,\mathrm{Cl}_3(kh)+\mathrm{i}\left[\pi(kh)^2-\frac{2}{3}(kh)^3\right]\end{aligned} \tag{3.21}$$

$$\begin{aligned}\Sigma_2 &= -2\pi\mathrm{i}(kh)^2\sum_{n=1}^{\infty}\sin(n\beta d)H_1^{(1)}(nkd)\\ &-8(kh)\sum_{n=1}^{\infty}\sin(n\beta d)\sum_{m=1}^{\infty}\sqrt{(2\pi m)^2-(kh)^2}\,K_1\left(n(d/h)\sqrt{(2\pi m)^2-(kh)^2}\right)\end{aligned} \tag{3.22}$$

and

$$\Sigma_3=\pi\mathrm{i}(kh)^2\left[\sum_{n=1}^{\infty}\cos(n\beta d)H_0^{(1)}(nkd)-\sum_{n=1}^{\infty}\cos(n\beta d)H_2^{(2)}(nkd)\right]$$

$$+ 4\sum_{n=1}^{\infty}\cos(n\beta d)\sum_{m=1}^{\infty}\left[\left[(2\pi m)^2+(kh)^2\right]K_0\left(n(d/h)\sqrt{(2\pi m)^2-(kh)^2}\right)\right.$$
$$\left.-\left[(2\pi m)^2-(kh)^2\right]K_2\left(n(d/h)\sqrt{(2\pi m)^2-(kh)^2}\right)\right]$$
$$-2(kh)^2\ln\left[2\sin\left(\frac{kh}{2}\right)\right]-2khCl_2(kh)-2Cl_3(kh)+\mathrm{i}\left[\frac{\pi}{2}(kh)^2-\frac{2}{3}(kh)^3\right]. \tag{3.23}$$

The rapidly convergent analytically continuable expressions (3.14)-(3.16) are used to calculate the corresponding Schlömilch series in (3.21)-(3.23). No special treatment is necessary for the Schlömilch series involving the modified Bessel functions K_0, K_1, and K_2 in (3.21)-(3.23) since even with complex βd these series converge rapidly because of the rapid decay of the modified Bessel functions with increasing n and m. Truncating these series at $n = 4$ and $m = 4$ gives sufficient accuracy.

As special cases of the kd–βd equation (3.20) we can obtain the kd–βd equation for a 2D array of electric dipoles in the plane of the array and perpendicular to the array axis

$$(kh)^3 = S_e\Sigma_1 \tag{3.24}$$

and the kd–βd equation for a 2D array of magnetic dipoles perpendicular to the plane of the array

$$(kh)^3 = S_m\Sigma_3\,. \tag{3.25}$$

3.1.2 ELECTRIC DIPOLES PERPENDICULAR TO THE ARRAY PLANE

As shown in [20, sec. 8.2] the kd–βd equation for a 2D array of magnetodielectric spheres with the electric dipoles polarized perpendicular to the array plane can be obtained from the kd–βd equation for a 2D array of magnetodielectric spheres with the electric dipoles in the array plane simply by interchanging Σ_1 and Σ_3. Thus

$$\frac{(kh)^3-S_e\Sigma_3}{S_e\Sigma_2}=\frac{S_m\Sigma_2}{(kh)^3-S_m\Sigma_1} \tag{3.26}$$

where Σ_1, Σ_2, and Σ_3 are given (3.21)-(3.23).

As special cases of the kd–βd equation (3.26) we can obtain the kd–βd equation for a 2D array of magnetic dipoles in the plane of the array and perpendicular to the array axis

$$(kh)^3 = S_m\Sigma_1 \tag{3.27}$$

and the kd–βd equation for a 2D array of electric dipoles perpendicular to the plane of the array

$$(kh)^3 = S_e\Sigma_3\,. \tag{3.28}$$

3.2 DIPOLES PARALLEL TO THE ARRAY AXIS

As we noted in the introduction to this section, there is no need to consider arrays with both electric and magnetic dipoles parallel to the array axis since there is no coupling between the electric and magnetic dipoles. Without loss of generality we can consider 2D arrays of electric dipoles parallel to the array axis. Our starting point is the kd–βd equation [20, eq. 7.21] obtained by expressing

the electric field incident on the reference electric dipole at the origin as the sum of electric dipole waves scattered from all the other electric dipoles in the array

$$(kh)^3 = S\Bigg\{ \sum_{\substack{n=-\infty \\ n\neq 0}}^{\infty} \mathrm{e}^{\mathrm{i}n\beta d} \sum_{m=-\infty}^{\infty} \frac{\mathrm{e}^{\mathrm{i}kh\rho_{mn}}}{\rho_{mn}} \left[\frac{-2\mathrm{i}}{\rho_{mn}} \left(kh + \frac{\mathrm{i}}{\rho_{mn}} \right) \frac{(nd/h)^2}{\rho_{mn}^2} \right.$$

$$\left. + \left((kh)^2 + \frac{\mathrm{i}kh}{\rho_{mn}} - \frac{1}{\rho_{mn}^2} \right) \frac{m^2}{\rho_{mn}^2} \right] + 2 \sum_{m=1}^{\infty} \frac{\mathrm{e}^{\mathrm{i}khm}}{m} \left((kh)^2 + \frac{\mathrm{i}kh}{m} - \frac{1}{m^2} \right) \Bigg\} \tag{3.29}$$

where

$$\rho_{mn} = \sqrt{m^2 + (nd/h)^2}\,. \tag{3.30}$$

From [20, eq. 6.70]

$$\sum_{\substack{n=-\infty \\ n\neq 0}}^{\infty} \mathrm{e}^{\mathrm{i}n\beta d} \sum_{m=-\infty}^{\infty} \frac{\mathrm{e}^{\mathrm{i}kh\rho_{mn}}}{\rho_{mn}} \left[\frac{-2\mathrm{i}}{\rho_{mn}} \left(kh + \frac{\mathrm{i}}{\rho_{mn}} \right) \frac{(nd/h)^2}{\rho_{mn}^2} \right.$$

$$\left. + \left((kh)^2 + \frac{\mathrm{i}kh}{\rho_{mn}} - \frac{1}{\rho_{mn}^2} \right) \frac{m^2}{\rho_{mn}^2} \right]$$

$$= 2 \sum_{n=1}^{\infty} \cos(n\beta d) \Bigg\{ \frac{\mathrm{i}\pi}{2} (kh)^2 \left[H_0^{(1)}(|n|kd) + H_2^{(1)}(|n|kd) \right]$$

$$+ 2 \sum_{m=1}^{\infty} \Bigg[\left[(2\pi m)^2 + (kh)^2 \right] K_0 \left(|n|(d/h) \sqrt{(2\pi m)^2 - (kh)^2} \right)$$

$$\left. + \left[(2\pi m)^2 - (kh)^2 \right] K_2 \left(|n|(d/h) \sqrt{(2\pi m)^2 - (kh)^2} \right) \Bigg] \right\} \tag{3.31}$$

and from [20, eq. 6.73]

$$2 \sum_{m=1}^{\infty} \frac{\mathrm{e}^{\mathrm{i}khm}}{m} \left((kh)^2 + \frac{\mathrm{i}kh}{m} - \frac{1}{m^2} \right)$$

$$= -2 \left((kh)^2 \ln \left[2 \sin \left(\frac{kh}{2} \right) \right] + kh\, \mathrm{Cl}_2(kh) + \mathrm{Cl}_3(kh) \right) + \mathrm{i} \left[\frac{\pi}{2} (kh)^2 - \frac{2}{3} (kh)^3 \right] \tag{3.32}$$

for $0 < kh < 2\pi$ with the Clausen functions $\mathrm{Cl}_2(kh)$ and $\mathrm{Cl}_3(kh)$ given by (3.9). Substituting (3.31) and (3.32) in (3.29) we obtain the computational form of the kd–βd equation

$$(kh)^3 = S\,\{\mathcal{Q}\} \tag{3.33}$$

where

$$\mathcal{Q} = \mathrm{i}\pi (kh)^2 \left[\sum_{n=1}^{\infty} \cos(n\beta d) H_0^{(1)}(nkd) + \sum_{n=1}^{\infty} \cos(n\beta d) H_2^{(1)}(nkd) \right]$$

$$+ 4 \sum_{n=1}^{\infty} \cos(n\beta d) \sum_{m=1}^{\infty} \left[\left[(2\pi m)^2 + (kh)^2 \right] K_0 \left(n(d/h) \sqrt{(2\pi m)^2 - (kh)^2} \right) \right.$$

$$+ \left[(2\pi m)^2 - (kh)^2\right] K_2\left(n(d/h)\sqrt{(2\pi m)^2 - (kh)^2}\right)\Bigg]$$

$$- 2\left((kh)^2 \ln\left[2\sin\left(\frac{kh}{2}\right)\right] + kh\mathrm{Cl}_2(kh) + \mathrm{Cl}_3(kh)\right) + \mathrm{i}\left[\frac{\pi}{2}(kh)^2 - \frac{2}{3}(kh)^3\right] . \tag{3.34}$$

The Schlömilch series with $H_0^{(1)}$ and $H_2^{(1)}$ are evaluated using the analytically continuable expressions (3.14) and (3.16). The Schlömilch series with K_0 and K_2 can be truncated at $n = 4$ and $m = 4$ with sufficient accuracy.

4 3D ARRAYS

In this section we investigate waves with complex propagation constants supported by 3D periodic arrays of lossless and lossy magnetodielectric spheres. In Subsection 4.1 it is assumed that the spheres can be effectively modeled by pairs of crossed electric and magnetic dipoles, each of the dipoles perpendicular to the array axis. In Subsection 4.2 we consider traveling waves supported by 3D periodic arrays of lossless and lossy magnetodielectric spheres with the dipole axes aligned parallel with the array axis. This reduces simply to traveling waves supported by a 3D array of either electric or magnetic dipoles aligned with the array axis because an electric (magnetic) dipole has no radial or longitudinal magnetic (electric) field [38, secs. 8.5, 8.6] and so there is no coupling of the electric dipoles with the magnetic dipoles of arrays with both the electric and magnetic dipoles aligned with the array axis. (For the same reason it is unnecessary to consider 3D arrays of electric and magnetic dipoles with the electric (magnetic) dipoles in the direction of the array axis and the magnetic (electric) dipoles perpendicular to the array axis.)

4.1 ELECTRIC AND MAGNETIC DIPOLES PERPENDICULAR TO THE ARRAY AXIS

In this subsection we consider traveling waves supported by 3D periodic arrays of lossless and lossy magnetodielectric spheres. It is assumed that the spheres can be modeled by pairs of crossed electric and magnetic dipoles, each of the dipoles perpendicular to the array axis. The analysis performed here is equally applicable to any 3D periodic arrays whose elements can be modeled by a pair of crossed electric and magnetic dipoles at right angles to each other such that only an incident electric (magnetic) field at the element center in the direction of the electric (magnetic) dipole excites only the electric (magnetic) dipole field. We choose the array axis to be the z axis of a Cartesian coordinate system with equispaced planes of magnetodielectric spheres normal to the z axis located at $z = nd, n = 0, \pm 1, \pm 2, \cdots$. In each plane the spheres are centered at $x = mh, y = lh, l, m = 0, \pm 1, \pm 2, \cdots$. The effective electric and magnetic dipole components of each sphere are oriented in the x and y direction, respectively. We assume an excitation of the array with the electric field parallel to the x axis and the magnetic field parallel to the y axis, and such that all the spheres in any column of the array are excited identically.

Our starting point is the pair of equations [20, 9.28],[21, eqs. 35a,b] obtained by expressing the electric and magnetic field incident on the reference sphere at $x = 0, y = 0, z = 0$ as the sum of the electric and magnetic dipole waves scattered from all the other elements of the array

$$(kh)^3 = S_e\Bigg\{ \sum_{\substack{n=-\infty \\ n\neq 0}}^{\infty} \mathrm{e}^{\mathrm{i}n\beta d} \sum_{m,l=-\infty}^{\infty} \frac{\mathrm{e}^{\mathrm{i}kh\rho_{mln}}}{\rho_{mln}} \left[\frac{-2\mathrm{i}}{\rho_{mln}}\left(kh + \frac{\mathrm{i}}{\rho_{mln}}\right)\frac{m^2}{\rho_{mln}^2}\right.$$

$$+\left((kh)^2+\frac{\mathrm{i}kh}{\rho_{mln}}-\frac{1}{\rho_{mln}^2}\right)\frac{l^2+(nd/h)^2}{\rho_{mln}^2}\Bigg]$$

$$-q\sum_{\substack{n=-\infty\\n\neq 0}}^{\infty}\mathrm{e}^{\mathrm{i}n\beta d}\sum_{m,l=-\infty}^{\infty}\frac{\mathrm{e}^{\mathrm{i}kh\rho_{mln}}}{\rho_{mln}}\left((kh)^2+\frac{\mathrm{i}kh}{\rho_{mln}}\right)\frac{nd/h}{\rho_{mln}}$$

$$+\sum_{\substack{m,l=-\infty\\(m,l)\neq(0,0)}}^{\infty}\frac{\mathrm{e}^{\mathrm{i}kh\rho_{ml0}}}{\rho_{ml0}}\left[\frac{-2\mathrm{i}}{\rho_{ml0}}\left(kh+\frac{\mathrm{i}}{\rho_{ml0}}\right)\frac{m^2}{\rho_{ml0}^2}+\left((kh)^2+\frac{\mathrm{i}kh}{\rho_{ml0}}-\frac{1}{\rho_{ml0}^2}\right)\frac{l^2}{\rho_{ml0}^2}\right]\Bigg\} \tag{4.1a}$$

and

$$(kh)^3=S_m\Bigg\{\sum_{\substack{n=-\infty\\n\neq 0}}^{\infty}\mathrm{e}^{\mathrm{i}n\beta d}\sum_{m,l=-\infty}^{\infty}\frac{\mathrm{e}^{\mathrm{i}kh\rho_{mln}}}{\rho_{mln}}\left[\frac{-2\mathrm{i}}{\rho_{mln}}\left(kh+\frac{\mathrm{i}}{\rho_{mln}}\right)\frac{l^2}{\rho_{mln}^2}\right.$$

$$\left.+\left((kh)^2+\frac{\mathrm{i}kh}{\rho_{mln}}-\frac{1}{\rho_{mln}^2}\right)\frac{m^2+(nd/h)^2}{\rho_{mln}^2}\right]$$

$$-\frac{1}{q}\sum_{\substack{n=-\infty\\n\neq 0}}^{\infty}\mathrm{e}^{\mathrm{i}n\beta d}\sum_{m,l=-\infty}^{\infty}\frac{\mathrm{e}^{\mathrm{i}kh\rho_{mln}}}{\rho_{mln}}\left((kh)^2+\frac{\mathrm{i}kh}{\rho_{mln}}\right)\frac{nd/h}{\rho_{mln}}$$

$$+\sum_{\substack{m,l=-\infty\\(m,l)\neq(0,0)}}^{\infty}\frac{\mathrm{e}^{\mathrm{i}kh\rho_{ml0}}}{\rho_{ml0}}\left[\frac{-2\mathrm{i}}{\rho_{ml0}}\left(kh+\frac{\mathrm{i}}{\rho_{ml0}}\right)\frac{l^2}{\rho_{ml0}^2}+\left((kh)^2+\frac{\mathrm{i}kh}{\rho_{ml0}}-\frac{1}{\rho_{ml0}^2}\right)\frac{m^2}{\rho_{ml0}^2}\right]\Bigg\} \tag{4.1b}$$

where

$$\rho_{mln}=\sqrt{m^2+l^2+(nd/h)^2} \tag{4.2}$$

$$\rho_{ml0}=\sqrt{m^2+l^2} \tag{4.3}$$

and S_e, S_m, and q are as in Section 2. Proceeding just as we did in our analysis of traveling waves with real propagation constants supported by 3D arrays of lossless magnetodielectric spheres, from [20, eq. 9.30],[21, eq. 37]

$$\sum_{\substack{n=-\infty\\n\neq 0}}^{\infty}\mathrm{e}^{\mathrm{i}n\beta d}\sum_{m,l=-\infty}^{\infty}\frac{\mathrm{e}^{\mathrm{i}kh\rho_{mln}}}{\rho_{mln}}\left[\frac{-2\mathrm{i}}{\rho_{mln}}\left(kh+\frac{\mathrm{i}}{\rho_{mln}}\right)\frac{m^2}{\rho_{mln}^2}\right.$$

$$\left.+\left((kh)^2+\frac{\mathrm{i}kh}{\rho_{mln}}-\frac{1}{\rho_{mln}^2}\right)\frac{l^2+(nd/h)^2}{\rho_{mln}^2}\right]$$

$$+\sum_{\substack{m,l=-\infty\\(m,l)\neq(0,0)}}^{\infty}\frac{\mathrm{e}^{\mathrm{i}kh\rho_{ml0}}}{\rho_{ml0}}\left[\frac{-2\mathrm{i}}{\rho_{ml0}}\left(kh+\frac{\mathrm{i}}{\rho_{ml0}}\right)\frac{m^2}{\rho_{ml0}^2}+\left((kh)^2+\frac{\mathrm{i}kh}{\rho_{ml0}}-\frac{1}{\rho_{ml0}^2}\right)\frac{l^2}{\rho_{ml0}^2}\right]$$

$$=-2\pi\mathrm{i}(kh)-2\pi kh\frac{\sin kd}{\cos\beta d-\cos kd}$$

$$-4\pi\sum_{n=1}^{\infty}\cos(n\beta d)\sum_{\substack{m,l=-\infty\\(m,l)\neq(0,0)}}^{\infty}\left[(2\pi m)^2-(kh)^2\right]\frac{\mathrm{e}^{-n(d/h)\sqrt{(2\pi)^2(m^2+l^2)-(kh)^2}}}{\sqrt{(2\pi)^2(m^2+l^2)-(kh)^2}}$$

$$+ 2\pi \mathrm{i}(kh)^2 \sum_{l=1}^{\infty} H_0^{(1)}(lkh) - 8 \sum_{l,m=1}^{\infty} \left[(2\pi m)^2 - (kh)^2\right] K_0\left(l\sqrt{(2\pi m)^2 - (kh)^2}\,\right)$$

$$+ 4\ kh\ \mathrm{Cl}_2(kh) + 4\ \mathrm{Cl}_3(kh) + \mathrm{i}\pi(kh)^2 - \mathrm{i}\frac{2}{3}(kh)^3 \tag{4.4}$$

with the Clausen functions Cl_2 and Cl_3 given by equations (3.9), and with $0 < kh < 2\pi$. From [20, eq. 9.76],[21, eq. 41]

$$\sum_{\substack{n=-\infty \\ n\neq 0}}^{\infty} \mathrm{e}^{\mathrm{i}n\beta d} \sum_{m,l=-\infty}^{\infty} \frac{\mathrm{e}^{\mathrm{i}kh\rho_{mln}}}{\rho_{mln}} \left((kh)^2 + \frac{\mathrm{i}kh}{\rho_{mln}}\right) \frac{nd/h}{\rho_{mln}}$$

$$= 2\pi kh\ \frac{\sin\beta d}{\cos\beta d - \cos kd}$$

$$- 4\pi\ kh \sum_{n=1}^{\infty} \sin(n\beta d) \sum_{\substack{m,l=-\infty \\ (m,l)\neq(0,0)}}^{\infty} \mathrm{e}^{-n(d/h)\ \sqrt{(2\pi)^2(m^2+l^2) - (kh)^2}}\,. \tag{4.5}$$

Substituting (4.4) and (4.5) in (4.1), using [58, eq. 8.521(1)]

$$\sum_{l=1}^{\infty} J_0(lkh) = -\frac{1}{2} + \frac{1}{kh}\ ,\ 0 < kh < 2\pi \tag{4.6}$$

and eliminating q from (4.1a) and (4.1b) we obtain the kd–βd equation

$$-q = \frac{(kh)^3 - S_e\Sigma_1}{S_e\Sigma_2} = \frac{S_m\Sigma_2}{(kh)^3 - S_m\Sigma_1} \tag{4.7}$$

where

$$\Sigma_1 = -2\pi kh\ \frac{\sin kd}{\cos\beta d - \cos kd}$$

$$- 4\pi \sum_{n=1}^{\infty} \cos(n\beta d) \sum_{\substack{m,l=-\infty \\ (m,l)\neq(0,0)}}^{\infty} \left[(2\pi m)^2 - (kh)^2\right] \frac{\mathrm{e}^{-n(d/h)\ \sqrt{(2\pi)^2(m^2+l^2) - (kh)^2}}}{\sqrt{(2\pi)^2(m^2+l^2) - (kh)^2}}$$

$$- 2\pi(kh)^2 \sum_{l=1}^{\infty} Y_0(lkh) - 8 \sum_{l,m=1}^{\infty} \left[(2\pi m)^2 - (kh)^2\right] K_0\left(l\sqrt{(2\pi m)^2 - (kh)^2}\,\right)$$

$$+ 4\ kh\ \mathrm{Cl}_2(kh) + 4\ \mathrm{Cl}_3(kh) - \mathrm{i}\frac{2}{3}(kh)^3 \tag{4.8}$$

and

$$\Sigma_2 = 2\pi\ kh\ \frac{\sin\beta d}{\cos\beta d - \cos kd}$$

$$- 4\pi\ kh \sum_{n=1}^{\infty} \sin(n\beta d) \sum_{\substack{m,l=-\infty \\ (m,l)\neq(0,0)}}^{\infty} \mathrm{e}^{-n(d/h)\ \sqrt{(2\pi)^2(m^2+l^2) - (kh)^2}}\,. \tag{4.9}$$

In (4.6)-(4.9), J_0 and Y_0 are the ordinary Bessel functions of the first and second kind. This kd–βd equation is analytically continuable into the complex βd plane as it stands simply by using the cosine and sine of a complex argument. Truncating the series in Σ_1 and Σ_2 with the decaying

exponential and with K_0 at $n = m = l = 4$ yields sufficient accuracy. The series $\Sigma Y_0(lkh)$ in Σ_1 is evaluated by [58, eq. 8.522(3)]

$$\sum_{l=1}^{\infty} Y_0(lkh) = -\frac{1}{\pi}\left(\gamma + \ln\frac{kh}{4\pi}\right) - 2\sum_{l=1}^{\infty}\left[\frac{1}{\sqrt{(2\pi l)^2 - (kh)^2}} - \frac{1}{2\pi l}\right], \quad 0 < kh < 2\pi \tag{4.10}$$

with γ the Euler constant given by (3.17). Truncating the series on the RHS of (4.10) at $l = 10$ gives sufficient accuracy for our purposes.

As special cases of the kd–βd equation (4.7) we can obtain the kd–βd equation for a 3D array of electric or magnetic dipoles perpendicular to the array axis

$$(kh)^3 = S\Sigma_1 \,. \tag{4.11}$$

where S is the normalized scattering coefficient of either the electric or the magnetic dipoles.

4.2 DIPOLES PARALLEL TO THE ARRAY AXIS

In this subsection we consider the complex propagation constants of traveling waves on 3D periodic arrays of lossless and lossy magnetodielectric spheres with the dipoles parallel to the array axis. As noted in the introduction to this section, we need only consider 3D arrays of electric (or magnetic dipoles) separately since there is no coupling between the electric and magnetic dipoles. Our starting point is the kd–βd equation [20, eq. 7.21]

$$\begin{aligned}(kh)^3 = S\Bigg\{ &\sum_{\substack{n=-\infty\\ n\neq 0}}^{\infty} \mathrm{e}^{\mathrm{i}n\beta d} \sum_{m,l=-\infty}^{\infty} \frac{\mathrm{e}^{\mathrm{i}kh\rho_{mln}}}{\rho_{mln}}\left[\frac{-2\mathrm{i}}{\rho_{mln}}\left(kh + \frac{\mathrm{i}}{\rho_{mln}}\right)\frac{(nd/h)^2}{\rho_{mln}^2}\right.\\ &\left. + \left((kh)^2 + \frac{\mathrm{i}kh}{\rho_{mln}} - \frac{1}{\rho_{mln}^2}\right)\frac{m^2 + l^2}{\rho_{mln}^2}\right]\\ &+ \sum_{\substack{m,l=-\infty\\ (m,l)\neq(0,0)}}^{\infty} \frac{\mathrm{e}^{\mathrm{i}kh\rho_{ml0}}}{\rho_{ml0}}\left((kh)^2 + \frac{\mathrm{i}kh}{\rho_{ml0}} - \frac{1}{\rho_{ml0}^2}\right)\Bigg\}\end{aligned} \tag{4.12}$$

where S is the normalized electric dipole scattering coefficient,

$$\rho_{mln} = \sqrt{m^2 + l^2 + (nd/h)^2} \tag{4.13a}$$

and

$$\rho_{ml0} = \sqrt{m^2 + l^2}\,. \tag{4.13b}$$

From [20, eq. 7.64]

$$\begin{aligned}\sum_{\substack{n=-\infty\\ n\neq 0}}^{\infty} \mathrm{e}^{\mathrm{i}n\beta d} \sum_{m,l=-\infty}^{\infty} \frac{\mathrm{e}^{\mathrm{i}kh\rho_{mln}}}{\rho_{mln}}&\left[-\frac{2\mathrm{i}}{\rho_{mln}}\left(kh + \frac{\mathrm{i}}{\rho_{mln}}\right)\frac{(nd/h)^2}{\rho_{mln}^2}\right.\\ &\left. + \left((kh)^2 + \frac{\mathrm{i}kh}{\rho_{mln}} - \frac{1}{\rho_{mln}^2}\right)\frac{m^2 + l^2}{\rho_{mln}^2}\right]\end{aligned}$$

$$= 16\pi^3 \sum_{n=1}^{\infty} \cos(n\beta d) \sum_{m,l=-\infty}^{\infty} \frac{(m^2+l^2)\, \mathrm{e}^{-n(d/h)\, \sqrt{(2\pi)^2(m^2+l^2)-(kh)^2}}}{\sqrt{(2\pi)^2(m^2+l^2)-(kh)^2}} \tag{4.14}$$

and from [20, eq. 7.71]

$$\sum_{\substack{m,l=-\infty \\ (m,l)\neq(0,0)}}^{\infty} \frac{\mathrm{e}^{\mathrm{i}kh\sqrt{m^2+l^2}}}{\sqrt{m^2+l^2}} \left((kh)^2 + \frac{\mathrm{i}kh}{\sqrt{m^2+l^2}} - \frac{1}{m^2+l^2} \right)$$

$$= \pi \mathrm{i} (kh)^2 \sum_{l=1}^{\infty} \left[H_0^{(1)}(lkh) - H_2^{(1)}(lkh) \right]$$

$$+ 4 \sum_{l,m=1}^{\infty} \left(\left[(2\pi m)^2 + (kh)^2 \right] K_0 \left(l\sqrt{(2\pi m)^2 - (kh)^2} \right) \right.$$

$$\left. - \left[(2\pi m)^2 - (kh)^2 \right] K_2 \left(l\sqrt{(2\pi m)^2 - (kh)^2} \right) \right)$$

$$-2 \left((kh)^2 \ln \left[2 \sin \left(\frac{kh}{2} \right) \right] + kh\mathrm{Cl}_2(kh) + \mathrm{Cl}_3(kh) \right) + \mathrm{i} \left[\frac{\pi}{2}(kh)^2 - \frac{2}{3}(kh)^3 \right] . \tag{4.15}$$

Substituting (4.14) and (4.15) in (4.12) and using (4.6) and [20, eqs. B.13]

$$\sum_{l=1}^{\infty} J_2(lkh) = \frac{1}{kh}, \quad 0 < kh < 2\pi \tag{4.16}$$

we obtain the kd–βd equation

$$(kh)^3 = S\{\mathcal{Q}\} \tag{4.17}$$

where

$$\mathcal{Q} = 16\pi^3 \sum_{n=1}^{\infty} \cos(n\beta d) \sum_{m,l=-\infty}^{\infty} \frac{(m^2+l^2)\, \mathrm{e}^{-n(d/h)\, \sqrt{(2\pi)^2(m^2+l^2)-(kh)^2}}}{\sqrt{(2\pi)^2(m^2+l^2)-(kh)^2}}$$

$$- \pi (kh)^2 \left[\sum_{l=1}^{\infty} Y_0(lkh) - \sum_{l=1}^{\infty} Y_2(lkh) \right]$$

$$+ 4 \sum_{l,m=1}^{\infty} \left[\left[(2\pi m)^2 + (kh)^2 \right] K_0 \left(l\sqrt{(2\pi m)^2 - (kh)^2} \right) \right.$$

$$\left. - \left[(2\pi m)^2 - (kh)^2 \right] K_2 \left(l\sqrt{(2\pi m)^2 - (kh)^2} \right) \right]$$

$$- 2 \left((kh)^2 \ln \left[2 \sin \left(\frac{kh}{2} \right) \right] + kh\mathrm{Cl}_2(kh) + \mathrm{Cl}_3(kh) \right) - \mathrm{i} \frac{2}{3}(kh)^3 . \tag{4.18}$$

In (4.15)-(4.18), J_n, Y_n, K_n, and $H_n^{(1)}$, are the nth order ordinary Bessel functions of the first and second kind, the modified Bessel function, and the Hankel function of the first kind, respectively, and Cl_2 and Cl_3 are the Clausen functions given by (3.9). The kd–βd equation is analytically continuable into the complex βd plane as it stands simply by using the cosine of a complex argument.

Truncating the series in $\mathcal{Q}$ with the decaying exponential and with K_0 at $n = m = l = 4$ yields sufficient accuracy. The series $\Sigma Y_0(lkh)$ is evaluated by (4.10) while the series $\Sigma Y_2(lkh)$ is evaluated by [20, eqs. B.14 - B.15],[21, eq. A9]

$$\sum_{l=1}^{\infty} Y_2(lkh) \approx 2 \sum_{m=1}^{\infty} \frac{\mathrm{e}^{-2q_m}}{kh \sinh q_m} + \lambda_2 \tag{4.19}$$

where

$$\sinh q_m = \sqrt{\beta_m^2 - 1} \tag{4.20a}$$

$$\beta_m = \frac{2m\pi}{kh} \tag{4.20b}$$

$$\lambda_2 = \frac{1}{2\pi}\left[B_0(0) - 2\left(\frac{2\pi}{kh}\right)^2 B_2(0)\right] = \frac{1}{2\pi}\left[1 - 2\left(\frac{2\pi}{kh}\right)^2 \frac{1}{6}\right] \tag{4.20c}$$

and B_0 and B_2 are the Bernoulli polynomials given by (3.19). Truncating the series on the RHS of (4.19) at $m = 10$ gives sufficient accuracy.

5 EFFECTIVE PERMITTIVITY AND PERMEABILITY

When the magnetodielectric spheres of a 3D cubic-lattice array are sufficiently close so that both $\beta d \ll 1$ and $kd \ll 1$ where β is the real propagation constant of a transverse traveling wave supported by the array, we argue in [20, sec. 9.3],[21, sec. 3.2] that the array can be regarded macroscopically as a homogeneous medium, which we refer to as the array medium. (See, however, Footnote 23 below.) The array medium is characterized by an effective or bulk relative permittivity $\epsilon_{\mathrm{r}}^{\mathrm{eff}}$ and effective relative permeability $\mu_{\mathrm{r}}^{\mathrm{eff}}$ that determine the propagation constant of a traveling wave in the direction of the array axis perpendicular to the orientations of the crossed electric and magnetic dipoles by which the spheres are modeled.[18] We then show how $\epsilon_{\mathrm{r}}^{\mathrm{eff}}$ and $\mu_{\mathrm{r}}^{\mathrm{eff}}$ can be obtained from the parameters available to us in solving the kd–βd equation.[19] For complex βd the assumption that $\beta d \ll 1$ is replaced by the assumption that $|\beta d| \ll 1$, the final expressions for the effective constitutive parameters are the same as for real βd, and the derivation of these expressions differs only slightly from that of the derivation for real βd. Accordingly we can omit most of the details here.

[18] In general the array medium is anisotropic and $\epsilon_{\mathrm{r}}^{\mathrm{eff}}$ and $\mu_{\mathrm{r}}^{\mathrm{eff}}$ do not determine the propagation of waves traveling in directions other than along the array axis. If the array elements are radially symmetric magnetodielectric spheres then the directions of the effective electric and magnetic dipoles of the array are established by the traveling wave, and as the number of spheres per unit volume becomes large ($kd \ll 1$ as well as $\beta d \ll 1$) the array medium becomes increasingly isotropic. If, however, the directions of the effective electric and magnetic dipoles of the array elements are fixed independently of the traveling wave, as they are for split-ring resonators for example, then the array medium is anisotropic no matter how closely spaced the elements.

[19] At the time of writing [20] and [21] we were unfortunately unaware that in their 2003 paper [48], Simovski and He had developed a method for obtaining the effective parameters from the dispersion equation for a traveling wave supported by a cubic-lattice array of magnetodielectric elements (cubic unit cells with an Ω-shaped perfectly conducting particle on each face) that is essentially the same as ours. The principal difference between their method and ours is that their expressions for the effective parameters are based on a form of the dispersion equation obtained by approximating the infinite summations involved, whereas our method is based on the exact dispersion equation obtained using closed-form expressions for the infinite summations.

As in [20, eq. 9.93],[21, eq. 56] the starting point is the relation, valid for transverse plane waves[20]

$$\frac{\beta d}{kd} = \sqrt{\mu_{\rm r}^{\rm eff}\ \epsilon_{\rm r}^{\rm eff}} \tag{5.1}$$

where, as throughout, we shall assume that the sign of the square root is chosen to keep the real part of β positive in the $\exp(\mathrm{i}\beta z)$ dependence. [20, eq. 9.100],[21, eq. 62] is replaced by

$$\frac{m}{p} = \frac{\mu_{\rm r}^{\rm eff} - 1}{\epsilon_{\rm r}^{\rm eff} - 1}\ \frac{\sqrt{\epsilon_{\rm r}^{\rm eff}\mu_{\rm r}^{\rm eff}}}{\mu_{\rm r}^{\rm eff}}\ c \tag{5.2}$$

where c is the speed of light, and

$$\frac{m}{p} = c\,q \tag{5.3}$$

as before, where q is defined by (2.3) and obtained from (4.7).

From (5.3) and (5.2) we obtain

$$\frac{\mu_{\rm r}^{\rm eff} - 1}{\epsilon_{\rm r}^{\rm eff} - 1}\ \frac{\sqrt{\epsilon_{\rm r}^{\rm eff}\mu_{\rm r}^{\rm eff}}}{\mu_{\rm r}^{\rm eff}} = q\ . \tag{5.4}$$

Equations (5.1) and (5.4) form a pair of simultaneous equations which can be solved for the two unknowns $\epsilon_{\rm r}^{\rm eff}$ and $\mu_{\rm r}^{\rm eff}$. Letting $\mathcal{R} = \beta d/(kd)$ we obtain as in [20, eq. 9.107, 9.108],[21, eq. 68]

$$\epsilon_{\rm r}^{\rm eff} = \frac{\mathcal{R}(\mathcal{R}+q)}{1+\mathcal{R}\,q}\,, \quad \mu_{\rm r}^{\rm eff} = \frac{\mathcal{R}(1+\mathcal{R}\,q)}{\mathcal{R}+q}\ . \tag{5.5}$$

It should be noted that if the opposite choice of the sign of the square root in (5.1) is made, then βd, $\mathcal{R}$, and q change sign so that $\epsilon_{\rm r}^{\rm eff}$ and $\mu_{\rm r}^{\rm eff}$ given by (5.5) remain the same.[21]

In [20, sec. 9.2],[21, sec. 3.2] we also obtain expressions for the bulk permittivity and permeability of the array medium based on the Clausius-Mossotti relation [35, sec. 8-1], [60, sec. 2-4], assuming that $\beta d \ll 1$ and $kd \ll 1$, and that the transverse spacing of the array elements h equals the spacing d in the direction of the array axis. These expressions are derived with no reference to

[20]For a 3D array of electric or magnetic dipoles parallel to the array axis (direction of propagation), Maxwell's equations show that the array is not characterized by a homogeneous, isotropic, scalar permittivity and permeability satisfying 5.1 and 5.2.

[21]It might appear from the expressions (5.5) for the bulk parameters that for lossless arrays, as the light line is approached by the dispersion curve so that $\mathcal{R} \approx 1$ (and $\epsilon_{\rm r}^{\rm eff}$ and $\mu_{\rm r}^{\rm eff}$ become reciprocals), both $\epsilon_{\rm r}^{\rm eff}$ and $\mu_{\rm r}^{\rm eff}$ should approach the value of +1. However, a little thought and numerical examples such as [20, figs. 37 and 38; figs. 39 and 40],[21, figs. 25 and 26; figs. 27 and 28] show that when the light line is approached by a backward-wave (negative-slope) segment of the kd–βd diagram, both $\epsilon_{\rm r}^{\rm eff}$ and $\mu_{\rm r}^{\rm eff}$ are negative. Furthermore, numerical results show that $\epsilon_{\rm r}^{\rm eff}$ and $\mu_{\rm r}^{\rm eff}$ approach the value of -1 as the light line is approached by a backward-wave segment of the dispersion curve, only for array spheres of equal relative permittivity and permeability. For array spheres of unequal relative permittivity and permeability, $\epsilon_{\rm r}^{\rm eff}$ approaches a value different from -1 (and, of course, $\mu_{\rm r}^{\rm eff}$ approaches the reciprocal value). How is it that the computer-program implementation of (5.5) gives results that are so much at variance with what one might expect from a cursory examination of (5.5)? The answer is simply that $\mathcal{R}$ and q are not independent of one another and if the fine numerical details of their behavior are examined as the light line is approached by a backward-wave segment of the kd–βd diagram, the apparent contradiction disappears. If, for example, we consider the case of [20, figs. 37 and 38],[21, figs. 25 and 26] where the relative permittivity and permeability of the array spheres are equal, then it is found from computer results that as the light line is approached by the backward-wave segment, q very nearly approaches the value of -1 and $\mathcal{R} \approx 1+\epsilon$, $|\epsilon| \ll 1$ so that $\mathcal{R}(\mathcal{R}+q) \approx \epsilon$, $1+\mathcal{R}\,q \approx -\epsilon$, and hence $\epsilon_{\rm r}^{\rm eff} = \mu_{\rm r}^{\rm eff} \approx -1$. A similar analysis can be performed for the case of array spheres with unequal relative permittivity and permeability.

the solution of the kd–βd equation and are equally valid here provided that $|\beta d| \ll 1$ and $kd \ll 1$:[22]

$$\epsilon_{\mathrm{r}}^{\mathrm{eff,CM}} = \frac{2B+3}{3-B} \tag{5.6}$$

$$\mu_{\mathrm{r}}^{\mathrm{eff,CM}} = \frac{2A+3}{3-A} \tag{5.7}$$

where

$$B = -\frac{6\pi i b_1^{\mathrm{sc}}}{(kd)^3} \tag{5.8}$$

$$A = -\frac{6\pi i a_1^{\mathrm{sc}}}{(kd)^3} \tag{5.9}$$

and b_1^{sc} and a_1^{sc} are the Mie electric and magnetic dipole scattering coefficients, respectively, given in [38, sec. 9.25, eqs. 11,10].

The derivations given in this section assume that $|\beta d|$ and $kd \ll 1$. In practice, however, as mentioned in the Introduction, these conditions can be relaxed somewhat to the "rule of thumb" that $|\beta d|$ and kd be less than about 1 [21, sec. 3.2].[23]

6 PARTIALLY FINITE ARRAYS

In [20, sec. 11],[21, sec. 5] we obtain expressions for the field at any point on the array axis (other than at elements of the array) excited by a plane wave incident from free space on a 3D partially finite periodic array of lossless magnetodielectric spheres. The array is finite in the direction of the

[22]The conditions needed in general to derive the Clausius-Mossotti effective parameter expressions are that there should be many dipoles in a macroscopic volume in which the phase and magnitude of the dipoles is approximately uniform. In the context of this report, these conditions take the form $|\beta d| \ll 1$ and $kd \ll 1$ which in practice can be relaxed to $|\beta d| \lesssim 1$ and $kd \lesssim 1$.

[23]Simovski [61] has shown that even if $|\beta d|$ and kd are both $\ll 1$ it is still possible that the effective parameters obtained from solving the dispersion equation for the propagation constant of a transverse traveling wave in the axial direction of a cubic-lattice array may not accurately characterize the array regarded as an isotropic, homogeneous medium. If, as for example in the first backward branch of the dispersion diagram shown in [22, fig. 2], $|\beta d|$ is changing very rapidly within a very small kd interval (frequency band), then even a small change in the dispersion diagram that can be expected if propagation in a direction other than axial is considered, can result in a large change in the associated values of the effective permittivity and permeability. Examining [22, figs. 3,4], for example, where the effective parameters corresponding to the dispersion diagram of [22, fig. 2] are plotted versus kd, it is seen that the effective parameters are changing extremely rapidly with kd in the vicinity of the kd interval when they are negative. Thus, the frequency interval where $|\beta d|$ is small and the effective parameters are both negative, may no longer be associated with negative effective parameters if propagation in a non-axial direction is considered. It should be emphasized, however, that the extremely narrow frequency band of the dispersion diagram backward branch in the example of [22] we have referred to here, is by no means typical, and for wider frequency bands with slower variation of $|\beta d|$ with frequency, the effective parameters obtained from the solution to the axial propagation dispersion equation can be expected to reasonably well characterize the array regarded as an isotropic, homogeneous medium when both $|\beta d|$ and kd are small . One further important point should be noted here. The Clausius-Mossotti expressions for the effective parameters are derived with no reference to the propagation direction. Consequently, the frequency regions where the effective parameters obtained from the solution of the axial-propagation dispersion equation can be expected to be a good characterization of the array regarded as an isotropic medium, are such that these effective parameters agree reasonably well with the Clausius-Mossotti effective parameters. Thus a combined plot of the dispersion equation effective parameters and the Clausius-Mossotti effective parameters is a very useful tool for estimating the frequency regions where the array can be expected to behave as a quasi-isotropic medium, and conversely where isotropy cannot be expected to hold. In the example of [22] cited in this footnote, it is seen that the plots of the dispersion equation effective parameters increasingly diverge from the Clausius-Mossotti effective parameter plots as the doubly-negative kd interval is approached, a clear indication that isotropy may not hold in the doubly-negative kd region.

array axis and infinite in the directions transverse to the array axis. The direction of incidence of the illuminating plane wave is parallel to the array axis, normal to the interface between the array and free space. The spheres are modeled by pairs of crossed electric and magnetic dipoles, each of the dipoles perpendicular to the array axis. The expressions obtained for the field on the array axis in [20, sec. 11],[21, sec. 5] are completely independent of the kd–βd equation and are equally valid as they stand for a 3D partially finite periodic array of lossless or lossy magnetodielectric spheres.

The corresponding expression for the field on the array axis of a 3D partially finite periodic array of electric dipoles parallel to the array axis, applicable to either lossless or lossy dipoles, is given in [20, sec. 11.2]. The same expression is valid as well for a 3D partially finite array of magnetic dipoles parallel to the array axis.

7 BIDIRECTIONALITY AND COMPLEX CONJUGATES OF WAVES

In this section we discuss the bidirectionality and complex conjugates of the propagation constants of traveling waves in the direction of the array axis supported by 1D, 2D, and 3D periodic arrays of lossless scatterers. Our starting point is the paper [36] (also see Appendix C) in which it is proved that a reciprocal (lossy or lossless) waveguide (uniform or periodic) that supports a traveling wave with propagation constant β also supports a corresponding traveling wave with propagation constant $-\beta$, and that for every traveling wave with a complex propagation constant β on a lossless reciprocal uniform or periodic waveguide there exists a corresponding traveling wave with complex conjugate propagation constant β^*. Regarding bidirectionality, it is clear from the analysis we have presented in Sections 2, 3, and 4, either from inspection of the starting summations or of the final forms of the dispersion equations, that if βd is a solution of the dispersion equation for a 1D, 2D, or 3D array, then so is $-\beta d$. More complicated, however, is the relation of our results to the above complex conjugate propagation constant theorem. For the lossless 3D arrays considered in this report, it is easy to show that if βd is a complex solution to the dispersion equation then so is $(\beta d)^*$. For the lossless 1D and 2D arrays we have considered, however, numerical results show that $(\beta d)^*$ is not necessarily a solution to the same dispersion equation satisfied by complex βd. However, in these 1D and 2D cases, $(\beta d)^*$ is a solution to the dispersion equation when the multivalued functions that appear in the dispersion equation are evaluated with branches other than the principal one. We first look at the 3D arrays, and then discuss the 2D and 1D arrays.

Consider the kd–βd equation (4.7) for the 3D array of magnetodielectric spheres with the dipoles oriented perpendicular to the array axis. Dividing the LHS and RHS of (4.7) by S_e and S_m, respectively, we obtain

$$\frac{\dfrac{(kh)^3}{S_e} - \Sigma_1}{\Sigma_2} = \frac{\Sigma_2}{\dfrac{(kh)^3}{S_m} - \Sigma_1} \,. \tag{7.1}$$

Referring to (4.8) let

$$\Sigma_1' = \Sigma_1 + \mathrm{i}\frac{2}{3}(kh)^3 \,. \tag{7.2}$$

Then, using the relations [20, eq. 4.61],[21, eq. 45]

$$S_e = \frac{3}{2}\sin\psi_e \, \mathrm{e}^{\mathrm{i}\psi_e}, \quad S_m = \frac{3}{2}\sin\psi_m \, \mathrm{e}^{\mathrm{i}\psi_m} \tag{7.3}$$

where ψ_e and ψ_m are the phases of the normalized lossless Mie scattering coefficients S_e and S_m, respectively, we see that

$$\frac{(kh)^3}{S_e} - \Sigma_1 = \frac{2}{3}(kh)^3 \ \frac{\cos\psi_e}{\sin\psi_e} - \Sigma_1' \tag{7.4a}$$

and

$$\frac{(kh)^3}{S_m} - \Sigma_1 = \frac{2}{3}(kh)^3 \ \frac{\cos\psi_m}{\sin\psi_m} - \Sigma_1' \tag{7.4b}$$

so that the dispersion equation (4.7) is equivalent to

$$\frac{\frac{2}{3}(kh)^3 \ \frac{\cos\psi_e}{\sin\psi_e} - \Sigma_1'}{\Sigma_2} = \frac{\Sigma_2}{\frac{2}{3}(kh)^3 \ \frac{\cos\psi_m}{\sin\psi_m} - \Sigma_1'} \ . \tag{7.5}$$

Referring to (4.8) and (4.9) we see that changing βd to $(\beta d)^*$ changes both sides of (7.5) to their complex conjugates, so that if βd is a solution of (7.5) then so is $(\beta d)^*$. Exactly the same line of reasoning applied to a 3D array of dipoles parallel to the array axis shows that if βd is a solution of the kd–βd equation (4.17) then so is $(\beta d)^*$.

Next, let us consider 2D arrays. Just as investigating the propagation of waves on a 2D slab in Appendix A gives much insight into the analytic continuation procedure that plays a central role in the main body of the report, so our treatment of the slab can also give us considerable insight into a wave with propagation constant $(\beta d)^*$ corresponding to one with propagation constant βd. The kd–βd equation derived in Appendix A for a TE wave supported by a 2D slab is

$$\tan\gamma d = \frac{\gamma d}{\mathrm{i}\mu_r\gamma_0 d} \tag{7.6}$$

with

$$\gamma d = [(kd)^2 - (\beta d)^2]^{1/2} \tag{7.7a}$$

$$\gamma_0 d = [(k_0 d)^2 - (\beta d)^2]^{1/2} \tag{7.7b}$$

and

$$(kd)^2 = \omega^2\mu\epsilon = (k_0)^2\mu_r\epsilon_r \ . \tag{7.7c}$$

If $(\beta d)^*$ is substituted for βd in (7.6), $\tan(\gamma d)$, γd, and $\gamma_0 d$ all change into their complex conjugates, but the factor of i in the denominator of the RHS of (7.6) remains unchanged. Hence $(\beta d)^*$ is not a solution of (7.6) as it stands. However, if the alternative branch for the square root function defining $\gamma_0 d$ is used, then instead of $\gamma_0 d$ in (7.6) we have $-\gamma_0 d$ and $(\beta d)^*$ is then a solution of the modified form of (7.6). Much the same idea applies to the kd–βd equation (3.20) for a 2D array of magnetodielectric spheres with the electric dipoles in the plane of the array. The term $\mathrm{i}\sqrt{\beta_0^2 - 1}$ appears in the expressions (3.14), (3.15) and (3.16) for calculating the Schlömilch series that appear in Σ_1, Σ_2, and Σ_3 given by (3.21)-(3.23). Referring to (3.11)

$$\mathrm{i}\sqrt{\beta_0^2 - 1} = \frac{kd}{\gamma_0} \tag{7.8}$$

(note that k, the free-space wave number in the main body of the report is identical to k_0 in Appendix A). Exactly analogous to the way $(\beta d)^*$ is a solution of the slab dispersion equation (7.6) if the alternative branch for the square root function defining γ_0 is used, so if $-\sqrt{\beta_0^2 - 1}$ is substituted for $\sqrt{\beta_0^2 - 1}$ in (3.14), (3.15), and (3.16), and these expressions then substituted in

(3.20), then $(\beta d)^*$ is found to be a solution of the modified form of (3.20) when βd is a solution of the original form of (3.20). The same conclusion holds for the kd–βd equation (3.26) of the 2D array of magnetodielectric spheres with the electric dipoles perpendicular to the plane of the array, and the kd–βd equation (3.33) of a 2D array of electric dipoles parallel to the array axis. Although in general this report does not consider propagation in the direction transverse to the array axis, for the 2D arrays considered in this report propagation in the direction y normal to the plane of the array is seen to be given by $e^{i\gamma_0 y} = e^{i(k^2 - \beta^2)^{1/2} y}$. This wave is proper or improper if $\Im(\gamma_0)$ is positive or negative, respectively.

In the case of 1D arrays, consideration of waves supported by a magnetodielectric rod does not give any insight into why β^* is often not a solution of the same dispersion equation satisfied by β unless alternate branches of the dispersion function are taken into account, unlike the situation for the 2D slab that we have just discussed. (For the magnetodielectric rod, it is easy to see from the expressions for the dispersion equations for TE, TM, HE, and HM modes given in [62, sec. 3.2] that if β is a solution of the dispersion equation then so is β^*.[24]) However, just as in the 2D continuous and periodic cases, if βd is a solution of the kd–βd equation for the 1D array, then so is $(\beta d)^*$ provided that branches of the multivalued functions other than the principal ones are used when the kd–βd function is evaluated.

Refer to the kd–βd equation, (2.9), for a 1D array of magnetodielectric spheres with dipoles oriented perpendicular to the array axis. In this equation Σ_1 and Σ_2 are defined in terms of sums and differences of the polylogarithm functions $\mathrm{Li}_N(z), N = 1, 2, 3$. To obtain higher order branches of the multivalued functions that appear in Σ_1 and Σ_2 we need expressions for the higher order branches of $\mathrm{Li}_N(z)$ given the principal values of these functions. Since $\mathrm{Li}_1(z) = -\ln(1-z)$, higher order branches of $\mathrm{Li}_1(z)$ are obtained simply by adding integer multiples of $2\pi\mathrm{i}$ to the principal value of $-\ln(1-z)$. To obtain the relation of the higher order branches of $\mathrm{Li}_2(z)$ and $\mathrm{Li}_3(z)$ to their principal values we proceed as follows. The polylogarithm functions satisfy the differential recursion relation [63, eq. 18]

$$z\frac{\mathrm{dLi}_s(z)}{\mathrm{d}z} = \mathrm{Li}_{s-1}(z)\,. \tag{7.10}$$

Let

$$\mathrm{Li}_n(z) = \mathrm{Li}_n(z)_{\text{principal}} + 2m\pi\mathrm{i} f(n)\ln^{n-1}(z)\,. \tag{7.11}$$

Then from (7.10) $f(n)$ satisfies the recursion relation

$$f(n+1) = \frac{f(n)}{n}\,, \quad f(1) = 1. \tag{7.12}$$

Then $f(2) = 1$, $f(3) = \frac{1}{2}$, and

$$\mathrm{Li}_2(z) = \mathrm{Li}_2(z)_{\text{principal}} + 2m\pi\mathrm{i}\ln(z), \quad m = 0, \pm1, \pm2, \cdots \tag{7.13a}$$

and

$$\mathrm{Li}_3(z) = \mathrm{Li}_3(z)_{\text{principal}} + m\pi\mathrm{i}\ln^2(z), \quad m = 0, \pm1, \pm2, \cdots\,. \tag{7.13b}$$

[24] As an example, the dispersion equation for TE modes [62, eq. 3.2-17a] is

$$\frac{J_1(ha)}{haJ_0)ha)} = -\frac{K_1(qa)}{qaK_0(qa)} \tag{7.9}$$

where a is the rod radius, J_0 and J_1 are the ordinary Bessel functions of order 0 and 1, respectively, K_0 and K_1 are the modified Bessel functions of order 0 and 1, respectively, $ha = \sqrt{n^2(k_0a)^2 - (\beta a)^2}$, $qa = \sqrt{(n^2-1)(k_0a)^2 - (ha)^2}$, and $n = \sqrt{\epsilon_r\mu_r}$ is the refractive index of the rod material. Changing β to β^* has the effect of changing both sides of (7.9) to their complex conjugates so that if (7.9) is satisfied by β it is also satisfied by β^*.

Since the logarithm function in (7.13) itself has branches, (7.13) can be more completely written as

$$\mathrm{Li}_2(z) = \mathrm{Li}_2(z)_{\text{principal}} + 2m\pi\mathrm{i}\ln(z) - 4mk\pi^2, \quad m = 0, \pm1, \pm2, \cdots, \quad k = 0, \pm1, \pm2, \cdots \tag{7.14a}$$

and

$$\mathrm{Li}_3(z) = \mathrm{Li}_3(z)_{\text{principal}} + m\pi\mathrm{i}\ln^2(z) - 4mk\pi^2\ln(z) - 4mk^2\pi^3\mathrm{i}, \quad m = 0, \pm1, \pm2, \cdots,$$
$$k = 0, \pm1, \pm2, \cdots \ . \tag{7.14b}$$

Equation (7.14a) is identical to [55, eq. 3.13]. Using (7.14) it is then a simple matter to evaluate (2.9) for any choice of branches. In practice the branches given by (7.13) have been found sufficient to show numerically that if βd is a solution of (2.9) evaluated with the principal branches of the multivalued functions then $(\beta d)^*$ is also a solution of (2.9) provided branches other than the principal can be chosen. Of course the same conclusion holds for the kd–βd equation, (2.13), for a 1D array of dipoles parallel to the array axis.

In Appendix C it is shown that, for lossless reciprocal waveguides, the only difference between the full propagation behavior (that is, combined longitudinal and transverse propagation) of the β and $-\beta^*$ waves decaying in the positive z direction is the sign of the phase. This result follows from the general theorem, derived from Maxwell's equations, which states that for every solution $(\mathbf{E}, \mathbf{H})$ on a lossless reciprocal waveguide there is another solution $(\mathbf{E}^*, -\mathbf{H}^*)$ [36]. Also, since it can be shown [36], as discussed at the beginning of this section, that if a reciprocal waveguide has a complex-wave solution with propagation constant in the z direction β, then there exists a corresponding solution with propagation constant in the z direction $-\beta$. Therefore, it is of interest to know when and why $(\beta d)^*$ is a solution of the same principal-branch 1D and 2D kd–βd equation as is satisfied by βd, and when it is not. As to "when?", a considerable number of numerical examples support (but do not necessarily establish) the conclusion that in the fast-wave region $(\beta d)^*$ is never a solution of the principal-branch dispersion equation satisfied by βd. (It is, as stated above, always a solution of the dispersion equation evaluated with alternative branches of the multivalued functions involved.) In the slow-wave region, $(\beta d)^*$ is generally a solution of exactly the same principal-branch dispersion equation satisfied by βd, apart from some examples where the magnitude of the imaginary part of a solution βd is very large, or when $\Re(\beta d)$ is very close to the light line. We are unable at the present time to support these conclusions analytically. One possible conjecture based on the physics is that in the fast-wave region, solutions of the kd–βd equations for our 1D and 2D arrays of magnetodielectric spheres correspond to improper "leaky waves" that are not part of the complete set of modes and thus are not all found as solutions to the principal-branch dispersion equation. The slow-wave solutions, on the other hand, generally correspond to proper waves that are part of the complete set of modes and thus it can be expected that all possible solutions are determined by the principal-branch dispersion equation, except where $\Im(\beta d)$ is too large or $\Re(\beta d)$ is very close to kd (the light line).

Tamir and Oliner [64] (see Appendix C) have looked into the question of whether physically realistic sources can produce a significant amount of energy in the four complex waves decaying in the positive z direction, the two proper complex waves (outgoing and incoming) and the two improper complex waves (outgoing and incoming). They find that the two proper complex waves can be appreciably excited by realistic sources. In addition, in the near-field region of waveguides, the outgoing improper complex wave (the classic leaky wave) can dominate the fields. However, the incoming improper complex wave cannot apparently be excited by finite-magnitude sources of finite extent. In particular, if β refers to a proper complex wave, then both the β and $-\beta^*$ waves can

be excited to an appreciable extent by finite sources. However, if β refers to an improper outgoing wave (leaky wave), it can be appreciably excited by realistic sources but the corresponding $-\beta^*$ improper incoming wave cannot.

8 NUMERICAL RESULTS

In this section we present a variety of kd–βd diagrams obtained with high-accuracy computer implementations of the expressions derived in the previous sections. Our objective in this section is primarily to display a representative selection of kd–βd diagrams without attempting to give physical explanations of the behavior shown in these diagrams. Alù and Engheta in a series of papers [65],[66],[43],[67] have made an important contribution towards obtaining physical understanding of the behavior of dispersion diagrams of periodic arrays of electric dipoles in terms of nanocircuit and nanotransmission lines. Further work along these lines is needed for arrays of magnetodielectric spheres for which both electric and magnetic dipoles and their interactions must be taken into account.

The examples of dispersion diagrams we show here are for the most part designed to demonstrate what happens when the dispersion diagrams obtained in our previous papers and reports [27],[20],[21] under the assumption that βd is real, are extended to allow for complex βd. Some important notations and conventions used in our plots of the dispersion diagrams are as follows. We consistently use solid and dashed lines to plot $\Re(\beta d)$ and $\Im(\beta d)$, respectively, and use dotted lines to plot light lines ($kd = \Re(\beta d)$). Harmonic time dependence of $\exp(-\mathrm{i}\omega t)$, $\omega > 0$ is assumed. In the description of the arrays, a denotes the radius of the magnetodielectric spheres, and d denotes the distance between the centers of adjacent array elements. We plot $\Re(\beta d)$ in the interval $[0, \pi]$. Thus the sign of $\Im(\beta d)$ corresponding to this positive ($+z$ direction) phase velocity determines whether the wave is a "forward" [$\Im(\beta d) > 0$] or "backward" [$\Im(\beta d) < 0$] complex wave [17]. If we required that $\Im(\beta d)$ always be positive, then $\Re(\beta d)$ would be negative for "backward" waves and $\Re(\beta d)$ would have to be plotted in the interval $[-\pi, \pi]$ instead of in the interval $[0, \pi]$.

The group velocity $[cd(kd)/d\Re(\beta d)]$ is not necessarily in the direction of decay of the complex wave because the proof of the equality between group and energy-transport velocities requires that β be real [68]. Moreover, for proper complex waves on lossless arrays, the total energy transport across an xy plane (z = constant plane) is zero. Also, the proof of the equality between group and energy-transport velocities applies to continuous media and thus requires not only that β be real, but also that $\beta d \ll 1$ and $kd \ll 1$. Therefore, in reference to complex waves, the terms "forward" and "backward" simply denote that the phase velocity and exponential decay are in the same or opposite directions, respectively, and not necessarily that the phase and group velocities are in the same and opposite directions. For the portions of the kd–βd diagrams where β is real, the wave corresponding to a positive (negative) slope of the kd–βd diagram is often referred to as a "forward" ("backward") wave. However, in this paper we will reserve the terms "forward" and "backward" wave solely for complex waves as defined above, and use positive and negative group velocity as synonymous with positive and negative slope of the portions of the k–β diagram where β is real.

As we have noted, the polylogarithm functions in the 1D array kd–βd equations, and the square root functions in the 2D array kd–βd equations are multivalued. Obviously, time and space do not allow us to calculate and show the dispersion diagrams for all choices of the branches of these multivalued functions. Accordingly we show kd–βd diagrams corresponding to a choice of branches other than the principal branches of these multivalued functions for only a small selection of arrays. (See especially the kd–βd diagrams in Subsubsections 8.3.1 and 8.3.2 for 1D and 2D arrays of silver nanospheres with the electric dipoles oriented parallel to the array axis. Also see Mode 3 in Fig.

4.) As noted in the Introduction, because of the difficulty of finding complex zeroes of the kd–βd equation in a given region of the complex βd plane, it is possible for all the arrays considered that there are curves additional to those shown in the kd–βd diagrams of this section of the paper.

8.1 MAGNETODIELECTRIC SPHERE ARRAYS

8.1.1 LINEAR (1D) ARRAYS OF MAGNETODIELECTRIC SPHERES

In this subsubsection we consider two linear arrays, one with $\epsilon_r = \mu_r = 10$, and the other with $\epsilon_r = \mu_r = 20$. For a linear array of magnetodielectric spheres with $\epsilon_r = \mu_r = 10$, $a/d = 0.45$, and the dipoles transverse to the array axis, the kd–βd diagram for βd real is given in [27, fig. 12]. In Fig. 2 we show the first branch of this diagram with a positive-slope segment for kd from 0.724 to 0.884 in which βd increases from the light line to π at $kd = 0.884$ ($ka = 0.398$) close to the resonance frequency of $kd = 0.900$ ($ka = 0.405$), followed by a negative-slope segment for kd from 0.884 to 0.959 where βd decreases from π to the light line. The extension of this diagram into the fast-wave region is shown in Fig. 3. This extension has two distinct components. In the upper one ($kd > 0.928$), the backward-wave $\Re(\beta d)$ portion of Fig. 2 crosses the light line, decreases to 0 at $kd = 0.960$, and then increases again as a forward wave to the light line at $kd = 0.998$ where it ends. In this portion of the kd–βd diagram $\Im(\beta d)$ decreases from 0 to -1.28 as $\Re(\beta d)$ decreases from the light line to 0 (the backward-wave segment), then changes sign and increases to 2.26 as $\Re(\beta d)$ increases to the light line (the forward-wave segment). The end of the plots of $\Re(\beta d)$ and $\Im(\beta d)$ at $kd = 0.998$ deserves comment. This is not the end of the entire kd–βd diagram. As kd continues to increase a new branch of the kd–βd diagram begins at $kd \approx 1.22$ (we do not show this) but in the kd interval from 0.998 to 1.22 we have been unable to find any discrete wave at all. This stop-band interval beginning at the light line is seen repeatedly in other 1D and 2D array figures of this section of the paper. Unless our numerical search routine for complex zeroes of the kd–βd equation has overlooked some solutions, it appears that in these frequency ranges of 1D and 2D figures with no solutions of the kd–βd equation, the only fields that can exist are the "space waves" from the continuous spectra corresponding to integrals in the complex βd plane along the branch cuts of the kd–βd equation (see Appendix A). These space waves require external sources for their excitation. If, for example, a 1D array of magnetodielectric spheres is excited by an external source, then in addition to discrete traveling waves that can channel some of the incident energy along the array, there will also be a continuous spectrum of scattered fields in other directions, the space waves. In certain frequency ranges external sources can excite only these space waves. These are exactly the frequency ranges where there are no solutions to the kd–βd equation. (For 3D arrays the kd–βd equations do not contain functions with branch cuts so that there are only discrete modes. Consequently none of the 3D kd–βd diagrams display stop bands beginning at the light line.) The lower component of the extension of the kd–βd diagram of Fig. 2 into the fast-wave region begins with a backward-wave segment, at first near vertical until it reaches the $\Re(\beta d)$ curve of Fig. 2 with which it is then almost identical for a narrow frequency range. The negative-slope segment then takes off from the $\Re(\beta d)$ curve of Fig. 2 at $kd \approx 0.872$, and decreases to 0 at $kd = 0.916$, following which there is a forward-wave segment that ends at the light line at $kd \approx 0.930$. What is particularly interesting here is that there is a small section of the backward-wave segment in the slow-wave region where βd is complex, a transition region referred to in [69] as "the winding down of the leaky-wave solution." [25] Despite the similarity between this backward-wave segment of

[25] The structure analyzed in [69] is very different from ours, being a dielectric-filled rectangular waveguide with an asymmetric slit in its top wall and with an air-filled parallel plate stub guide above, and the frequency behavior is the opposite of ours.

Fig. 3 and the transition region of [69, figs. 3,4] we do not want to assert that the backward-wave segment in the fast-wave region of Fig. 3 corresponds to a leaky wave; that is, an outward-energy-propagating improper complex wave.[26] In this paper we consider only the longitudinal propagation constants of waves propagating in the direction of the array axis and do not attempt in general to investigate the behavior of these waves in the direction(s) transverse to the array axis. In Fig. 4 we show the kd–βd diagram for the same array but with additional modes displayed, demonstrating the complexity of the kd–βd diagram for complex waves. Mode 3 in Fig. 4 was obtained using (2.11) instead of (2.6a) for calculating $F_{1+}(kd, \beta d)$.

As an example to demonstrate the importance that both magnetic and electric dipoles play in the structure of the dispersion diagram, we show the kd–βd diagrams corresponding to Figs. 2 and 3 when magnetic dipoles are omitted in the calculations. The Mie electric dipole scattering coefficient was computed as before but the Mie magnetic dipole scattering coefficient was set equal to zero. In Fig. 5 we show the dispersion diagram obtained when βd is restricted to be real and in Fig. 6 we show the dispersion diagram obtained when βd is allowed to be complex. Comparison of corresponding figures shows the great difference between the diagrams obtained with and without the presence of magnetic dipoles. The βd curve of Fig. 5 terminates at the value of $\beta d = \pi$ with a negative-slope segment from $\beta d = 1.203$ ($kd = 0.900$) to $\beta d = \pi$ ($kd = 0.884$). In Fig. 6 we see that for $kd < 0.900$ the dispersion diagram is double-valued, the initial positive-slope section with $\Im(\beta d) = 0$, and a section with $\Re(\beta d) = \pi$ and $\Im(\beta d)$ decreasing from 2.49 at $kd = 0.800$ to 0 at $kd = 0.884$. The upper part, $kd = 0.935$ to 0.972, of the extension of the dispersion diagram into the fast-wave region with $\Re(\beta d)$ increasing from 0 to the light line is very similar to the corresponding segment in Fig. 3. As in Fig. 3 there is no continuation of the kd–βd diagram after $\Re(\beta d)$ reaches the light line. The lower part of the extension into the fast-wave region is a backward-wave segment that begins in the slow-wave region at $\Re(\beta d) = 1.230$ ($kd = 0.900$) starting at a point on the lower branch of the dispersion curve and then crosses the light line into the fast-wave region. As in Fig. 3 this results in there being a small interval where $\Re(\beta d)$ is in the slow-wave region and $\Im(\beta d)$ is not zero, a behavior, as noted in our discussion of Fig. 3, similar to the transition region of [69, figs. 3,4] with the small portion of this segment in the slow-wave region referred to as "the winding down of the leaky-wave solution."

For a linear array of magnetodielectric spheres with $\epsilon_r = \mu_r = 20$, $a/d = 0.45$, and the dipoles transverse to the array axis, the first branch of the kd–βd diagram for βd real is given in [27, fig. 15] which we reproduce here as Fig. 7. The extension of this diagram for complex βd is shown in Fig. 8. The principal features of Fig. 8 are very similar to those of Fig. 3 for the 1D $\epsilon_r = \mu_r = 10$ array, allowing for the lower frequency region of Fig. 8. The lower branch of the diagram goes to π at $ka = 0.211$ ($kd = 0.469$) close to the resonance frequency of the spheres at $ka = 0.214$ ($kd = 0.475$). The most interesting feature is the portion of the diagram for kd between 0.476 and 0.481, the backward-wave segment for $\Re(\beta d)$ that takes off from the first branch of the diagram, crosses the light line, and continues into the fast-wave region with $\Re(\beta d)$ decreasing to 0. There is again a small section of this segment in the slow-wave region where βd is complex, the transition region referred to in [69] as "the winding down of the leaky-wave solution." In Fig. 9 we show the kd–βd diagram for the same array but with additional modes displayed. The essential features of this figure are similar to those of Fig. 4. As in Fig. 4, Mode 3 in Fig. 9 was obtained using (2.11) instead of (2.6a) for calculating $F_{1+}(kd, \beta d)$.

For a linear array of magnetodielectric spheres with $\epsilon_r = \mu_r = 20$, $a/d = 0.45$, and the electric dipoles parallel to the array axis, the kd–βd diagram for βd real is given in [20, fig. 41] which we reproduce here as Fig. 10. The extension of this diagram into the fast-wave region is shown in Fig.

[26] A detailed treatment of leaky waves and leaky-wave antennas can be found in [37].

11. For kd between 0.407 and 0.453, βd is complex with $\Re(\beta d)$ describing a fish hook from the light line into the fast-wave region and then back again to the light line. Note that the bottom of the fish hook is not a continuation of a slow-wave region curve into the fast-wave region but begins at the light line. Note also that this portion of the fish hook is a negative-slope wave but $\Im(\beta d)$ is positive. For kd between 0.453 and 0.484, βd is real, increasing from the light line to π close to the resonance frequency of the spheres at $ka = 0.214$ ($kd = 0.475$). For values of $kd > 0.484$, there is a strongly attenuated wave with $\Re(\beta d)$ remaining equal to π and $\Im(\beta d)$ increasing rapidly.

8.1.2 2D ARRAYS OF MAGNETODIELECTRIC SPHERES

For βd real, the kd–βd diagram for a 2D array of magnetodielectric spheres with $\epsilon_r = \mu_r = 20$, $a/d = 0.45$, and the electric dipoles parallel or perpendicular to the plane of the array, is given in [20, fig. 36],[21, fig. 24] and is reproduced here as Fig. 12. Its extension for complex βd is shown in Fig. 13. The lower branch of the diagram goes to π at $kd = 0.449$ ($ka = 0.202$) fairly close to the resonance frequency of the spheres at $kd = 0.475$ ($ka = 0.213$) while the negative-slope branch of the diagram starts at $kd = 0.472$ ($ka = 0.212$). The bandgap between $kd = 0.4487$ and 0.4721 in Fig. 12 is seen to correspond to an attenuated wave with $\Re(\beta d) = \pi$ and $\Im(\beta d)$ increasing from 0.0 to 1.35 at the center of the bandgap. The behavior of the dispersion diagram from $kd = 0.486$ to 0.495 is especially interesting, and we show a detail of this region in Fig. 14. We have encountered behavior like this before in Figs. 3, 6, and 8, where a fast-wave region upper segment with $\Re(\beta d)$ increasing from 0 to the light line is joined to the curve of $\Re(\beta d)$ in the slow-wave region by a backward-wave segment which includes a small transition interval in the slow-wave region where βd is complex. Note that, as in Figs. 3, 6, and 8, there is a cut-off of the kd–βd diagram at the upper frequency of the plot. In Fig. 15 we show the kd–βd diagram for the same array but with an additional mode displayed. Note the high attenuation of this mode (Mode 2) compared with that of Mode 1. Figure 16 is a more detailed version of Fig. 15.

8.1.3 3D ARRAYS OF MAGNETODIELECTRIC SPHERES

For βd real, the kd–βd diagram for a 3D array of magnetodielectric spheres with $\epsilon_r = \mu_r = 20$, $a/d = 0.45$, and the electric and magnetic dipoles normal to the array axis is given in [20, fig. 37],[21, fig. 25] and is reproduced here as Fig. 17. When complex solutions of the kd–βd equation are allowed we obtain the kd–βd diagram of Fig. 18. Mode 1 is identical to the dispersion curve of Fig. 17, and an additional mode with high attenuation is shown, also obtained as a solution to the kd–βd equation. Mode 1 goes to π at $kd = 0.450$ ($ka = 0.203$) close to the resonance frequency of the spheres at $kd = 0.475$ ($ka = 0.213$). This figure demonstrates that complex modes can be supported by lossless 3D structures. No total power is carried by these modes, however.

In Fig. 19 we show the dispersion diagrams for the principal mode of Fig. 18 when the permeability of the spheres has a loss tangent of 0.002 and 0.02. The real part of the dispersion diagrams are so close to the dispersion diagram when the loss tangent is zero that even though the three curves are plotted in Fig. 19 it is impossible to distinguish them. The permeability loss tangents of 0.002 and 0.02 do, however, result in an imaginary part of the propagation constant βd as shown in the dashed line for the 0.002 loss tangent and the dot-dashed line for the 0.02 loss tangent. For the 0.002 loss tangent, the imaginary part of βd results in a power loss per wavelength [$-20\log_{10}(\exp(-2\pi|\Im(\beta d)|/kd)) = -20(2\pi|\Im(\beta d)|/kd)\ln 10$] of between 2.04 and 4.96 dB per wavelength in the negative-slope segment of the dispersion diagram, while for the 0.02 loss tangent, the imaginary part of βd results in a proportionally greater maximum power loss of between 20.1 and 50.1 dB per wavelength. For a linear array with $\epsilon_r = \Re(\mu_r) = 10$ (not shown), the power loss

for a 0.002 permeability loss tangent lies between 1.00 and 1.34 dB per wavelength, and for a 0.02 permeability loss tangent the power loss lies between 10.0 and 13.4 dB per wavelength. Currently we are not aware of any magnetodielectric material at frequencies above a few hundred MHz with both relative permittivity and permeability having real parts reasonably close to the same value of about 10 or greater, and a permeability loss tangent sufficiently small, that can be used for the fabrication of low-loss, isotropic doubly negative (DNG) materials. (For values of the real parts of the permittivity and permeability appreciably less than 10, it does not appear possible to obtain solutions of the kd–βd equation with both $|\beta d|$ and $kd < 1$ as required for the array to reasonably approximate a DNG homogeneous isotropic medium.)

8.1.4 EFFECTIVE PARAMETERS FOR 3D ARRAYS OF MAGNETODIELECTRIC SPHERES

In Figs. 20 and 21 we show the kd–βd diagrams and plots of the real and imaginary parts of the corresponding effective parameters, ϵ_r^{eff} and μ_r^{eff}, for two 3D cubic-lattice arrays of magnetodielectric spheres: 1) a lossless array with $\epsilon_r = (13.8, 0.0)$ and $\mu_r = (11.0, 0.0)$; and 2) a lossy array with $\epsilon_r = (13.8, 0.1)$ and $\mu_r = (11.0, 0.0)$. In both arrays the dipoles are perpendicular to the array axis and $a/d = 0.4$. βd is complex for the lossless as well as for the lossy array. For clarity the plots in both figures have been limited to the range $0.7 \leq kd \leq 0.9$. In the real βd dispersion diagram for the first array there are stop-bands in the intervals $kd = [0.7893, 0.8078]$ and $kd = [0.8738, 0.8812]$ where no wave with a real β can propagate. In Fig. 20, in these frequency intervals βd is complex so that the wave attenuates. In the interval $kd = [0.7893, 0.8078]$ $\Re(\beta d) = \pi$ and $\Im(\beta d)$ increases from 0 to 0.301 and then decreases to 0. In the interval $kd = [0.8738, 0.8812]$, $\Re(\beta d) = 0$ and $|\Im(\beta d)|$ increases from 0 to 0.091 and then decreases to 0 and thus is too small to be seen in the scale of the plot (as are the corresponding imaginary parts of the effective parameters). In the first and second positive-slope branches of the kd–βd diagram, $kd = [0.7, 0.7893]$ and $[0.8738, 0.9]$, it is seen from Fig. 21 that ϵ_r^{eff} and μ_r^{eff} are real and positive, while in the negative-slope branch, $kd = [0.8078, 0.8738]$, the effective parameters are both negative, an example of how a DNG medium can be formed from a periodic array of magnetodielectric spheres. Although in the interval $kd = [0.7893, 0.8078]$, $|\beta d|$ is too large for the array to behave as a continuous, homogeneous, isotropic medium, nevertheless viewed formally the complex values of the effective parameters are consistent with the complex value of βd in this interval and can yield a reflection coefficient for a slab of the array that is a reasonable approximation to the actual reflection coefficient. A consequence of the formal extension of the bulk parameters beyond the region where they are physically meaningful is, however, that the imaginary parts of ϵ_r^{eff} and μ_r^{eff} can become negative in this interval.

The effect of loss on the behavior of $\Re(\epsilon_r^{\text{eff}})$ is seen from Fig. 20 to be significant only in the bandgap region $kd = [0.7893, 0.8078]$. Whereas for the lossless array, $\Re(\epsilon_r^{\text{eff}})$ has a positive and negative infinite asymptote at $kd = 0.80875$, for the lossy array $\Re(\epsilon_r^{\text{eff}})$ is continuous (it drops down to -12.7, not shown in the figure, before increasing again) with a rather curious "V-shaped" dip at around $kd = 0.8013$. In the bandgap region the behavior of $\Im(\epsilon_r^{\text{eff}})$ is very different for the lossless and lossy arrays. For the lossy array, $\Im(\epsilon_r^{\text{eff}})$ is negative in the entire bandgap region, decreasing to -6.7 at $kd = 0.8066$ before increasing to 0 at $kd = 0.8078$. In contrast, for the lossy array $\Im(\epsilon_r^{\text{eff}})$ first decreases to -3.1 at $kd = .80$, then jumps suddenly to around 5 and increases rapidly to 19 at $kd = 0.80875$, and then decreases to 0.06 at $kd = 0.9$.

The effect of loss on the behavior of $\Re(\mu_r^{\text{eff}})$ is seen from Fig 21 to be significant only in the bandgap region, but the effect of loss is much less pronounced than it is on $\Im(\epsilon_r^{\text{eff}})$. The general shape of $\Re(\mu_r^{\text{eff}})$ for the lossless and lossy arrays is similar, but the peak value for the lossless array is about 15 as compared with about 6 for the lossy array. There is much more of an effect of loss

on $\Im(\mu_r^{\text{eff}})$ than on $\Re(\mu_r^{\text{eff}})$. For the lossless array $\Im(\mu_r^{\text{eff}})$ is positive throughout with a peak value of 7.8 reached rather abruptly at $kd = 0.790$ decreasing steadily to 0 at $kd = 0.8078$. For the lossy array, $\Im(\mu_r^{\text{eff}})$ increases steadily to a peak value of 4.2 at $kd = 0.7938$, then decreases rapidly to -2.9 at $kd = 0.8013$, after which it increases steadily to positive values at $kd = 0.8038$.

8.2 DIAMOND SPHERES

8.2.1 LINEAR (1D) ARRAYS OF DIAMOND SPHERES

In this subsubsection we consider two linear arrays of diamond spheres, the first with the dipoles normal to the array axis, and the second with the magnetic dipoles parallel to the array axis. For both arrays, $\epsilon_r = 5.84, \mu_r = 1$, $a/d = 0.45$. For the array with the dipoles transverse to the array axis, the dispersion diagram for real βd is shown in [20, fig. 18] which we reproduce here as Fig. 22. In Fig. 23 we show the extension of this dispersion diagram into the fast-wave region. The bandgap in Fig. 22, starting at $kd = 2.5733$ close to the first magnetic dipole resonance frequency of $kd = 2.787$ ($ka = 1.254$), is shown in Fig. 23 to correspond to a segment with $\Re(\beta d) = \pi$ and a small non-zero imaginary part. In the fast-wave region, $\Re(\beta d)$ decreases from the light line to 0 at $kd = 4.10$ and then starts to increase. (We have truncated the curve at $kd = 4.22$.) $\Im(\beta d)$ steadily increases in magnitude in the fast-wave region, negative in the backward-wave region and switching to positive when $\Re(\beta d)$ starts to increase from 0. In Fig. 24 we show the kd–βd diagram for the same array with two additional modes shown, both with high attenuation.

The kd–βd diagram for a 1D array of diamond spheres with the magnetic dipoles parallel to the array axis is given in [20, fig. 25] which we reproduce here as Fig. 25. The extension of this diagram into the fast-wave region is shown in Fig. 26. We see that $\Re(\beta d)$ begins at the light line when $kd = 2.407$, increases rather slowly in the fast-wave region with $\Im(\beta d)$ positive until $kd = 2.815$ where it crosses the light line and continues to increase in the slow-wave region until it reaches the value of π close to the magnetic dipole resonance frequency of $kd = 2.787$ ($ka = 1.254$). For this slow-wave region, $\Im(\beta d) = 0$ and this section of the curve is identical to the curve shown in Fig. 25. After $\Re(\beta d)$ reaches π it stays there for higher values of kd with $\Im(\beta d)$ then increasing so that the wave attenuates. Note that for this kd–βd diagram there is a lower cut-off frequency rather than the upper cut-off frequencies we have often encountered.

8.2.2 2D ARRAYS OF DIAMOND SPHERES

In this subsubsection we consider two 2D arrays of diamond spheres, the first with the electric dipoles in the plane of the array, and the second with the electric dipoles perpendicular to the array plane. As in the previous subsection, for both arrays, $\epsilon_r = 5.84$, $\mu_r = 1$, and $a/d = 0.45$. The dispersion diagram for a 2D array of diamond spheres with the electric dipoles in the plane of the array and βd real, is given in [20, fig. 19],[21, fig. 10] which is reproduced here as Fig. 27 and the corresponding dispersion diagram for complex βd is shown in Fig. 28. $\Re(\beta d)$ starts out very close to the light line, increasing to π at $kd = 2.220$ ($ka = 1.000$), somewhat lower than the first magnetic dipole resonance frequency of $kd = 2.787$ ($ka = 1.254$). This section of the curve is identical to the lower curve of Fig. 27. The bandgap in Fig. 27 is shown in Fig. 28 to correspond to a segment with $\Re(\beta d) = \pi$ and $\Im(\beta d)$ negative. At the upper end of the bandgap at $kd = 2.507$ ($ka = 1.128$), $\Im(\beta d)$ goes to zero where it remains until $\Re(\beta d)$ crosses the light line. This section of the curve is identical to the upper curve of Fig. 27. As kd continues to increase, $\Re(\beta d)$ enters the fast-wave region and $\Im(\beta d)$ becomes slightly negative (backward wave). After $\Re(\beta d)$ goes to zero and then starts to increase, $\Im(\beta d)$ switches to positive values (forward wave). In Fig. 29 we show the kd–βd diagram for the same array with four additional modes shown, all with high attenuation. Figure

30 is a detail of Fig. 29. Note that Mode 5 begins at the light line so that it has a lower cut-off frequency.

The dispersion diagram for the 2D array of diamond spheres with the electric dipoles perpendicular to the array plane and βd real is shown in [20, fig. 20],[21, fig. 11] and is reproduced here as Fig. 31, with the corresponding dispersion diagram for complex βd shown in Fig. 32. The behavior of the dispersion diagram in the fast-wave region is similar in essentials to that in Fig. 28, but with $\Im(\beta d)$ much larger in magnitude in the backward-wave region. In Fig. 33 we show the kd–βd diagram for the same array with five additional modes shown, all with high attenuation. Figure 34 is a detail of Fig. 33. Like Mode 5 in Figs. 29 and 30, Mode 6 begins at the light line so that it has a lower cut-off frequency.

The kd–βd diagram for a 2D array of diamond spheres with the magnetic dipoles parallel to the array axis and βd real is shown in [20, fig. 26],[21, fig. 14] and is reproduced here as Fig. 35, with the extension for complex waves given in Fig. 36. Notice that the dispersion diagram in Fig. 36 does not extend into the fast-wave region, unlike the dispersion diagram for a 1D array of diamond spheres with magnetic dipoles parallel to the array axis, Fig. 26. Although the dispersion diagram for βd real, Fig. 35, resembles the corresponding 1D dispersion diagram of Fig. 25 which does have an extension into the fast-wave region, the two dispersion diagrams are actually quite different in their behavior at the light line. In Fig. 35, βd approaches tangency to the light line, whereas in Fig. 25 βd is incident on the light line at a non-zero angle. The cut-off of the dispersion diagram of Fig. 35 when βd reaches π is continued for increasing kd by a wave with $\Re(\beta d) = \pi$ and $\Im(\beta d)$ increasing from 0. This continuation ends when $\Re(\beta d)$ crosses the light line at $kd = \pi$. This kd–βd diagram displays both lower and upper cut-off frequencies.

8.2.3 3D ARRAYS OF DIAMOND SPHERES

In this subsubsection we consider 3D arrays of diamond spheres with the dipoles transverse and parallel to the propagation direction. For transverse dipoles the dispersion diagram for real βd is given in [20, fig. 21],[21, fig. 12], reproduced here as Fig. 37, and the dispersion diagram for complex βd is shown in Fig. 38. The lower branch of the diagram goes to π at $kd = 2.024$ ($ka = 0.911$) considerably below the magnetic dipole resonance frequency of the spheres at $kd = 2.787$ ($ka = 1.254$). It is seen that the bandgaps in Fig. 37 where there is no unattenuated traveling wave correspond in Fig. 38 to regions where $\Im(\beta d) \neq 0$ and hence the wave is attenuated. The region $3.50 < kd < 3.77$ is interesting because there is a complex wave ($\Re[\beta d] > 0$) in the middle of the bandgap. In Fig. 39 shows the kd–βd diagram for the same array with five additional high attenuation modes. A detail of this figure is shown in Fig. 40.

The kd–βd curves for 3D arrays of diamond spheres with the dipoles parallel to the array axis and βd real are shown in [20, fig. 31],[21, fig. 15], reproduced here as Fig. 41, and the corresponding curves for complex βd are shown in Fig. 42. It is seen that for values of kd greater than the values where $\Re(\beta d)$ goes to π, $\Im(\beta d)$ increases steadily with $\Re(\beta d)$ remaining equal to π. (The curves continue upwards along $\Re(\beta d) = \pi$ but we have truncated them for clarity of presentation.) Both curves have lower cut-off frequencies.

8.3 SILVER NANOSPHERE ARRAYS

8.3.1 LINEAR (1D) ARRAYS OF SILVER NANOSPHERES

In this subsubsection we consider 1D arrays of silver nanospheres. As discussed in [20, sec. 12.4],[21, sec. 6.3] the dispersion diagrams were computed using the following Drude model for relative

permittivity which agrees quite well with the values of relative permittivity measured by Johnson and Christy [70] over the visible range of frequencies where lowest order traveling waves exist:

$$\epsilon_{\rm r} = \frac{\epsilon}{\epsilon_0} = 5.45 - 0.73\frac{\omega_p^2}{\omega(\omega + {\rm i}\gamma)} \tag{8.1}$$

with the plasma frequency $\omega_p = 1.72 \times 10^{16}$ and the loss parameter $\gamma = 8.35 \times 10^{13}$. To conform to the parameters used in [71], the radius a of the spheres was chosen to be 5 nm and the spheres were embedded in glass with a dielectric constant equal to 2.56 ($k = 1.6 \times \omega/c$). With these parameters the relative permittivity of the spheres in glass can be written from the Drude equation in (8.1) as

$$\epsilon_{\rm r} = \frac{\epsilon}{\epsilon_{\rm glass}} = 2.129 - \frac{0.0234}{(ka/1.6)[(ka/1.6) + 0.00139{\rm i}]}. \tag{8.2}$$

Our formulation in [20],[21] assumed real permittivity and real βd, and so only the real part of (8.2) was used in the calculations to obtain the kd–βd diagram. Here we use the complex value of $\epsilon_{\rm r}$ since βd is assumed to be complex.

The kd–βd curves for a 1D array of glass-embedded silver nanospheres and electric and magnetic dipoles perpendicular to the array axis, using only the real part of the permittivity and restricting βd to be real, are given in [20, fig. 28],[21, fig. 14] which we reproduce here as Fig. 43, with the corresponding curves for glass-embedded silver nanospheres using the complex values of the permittivity and complex βd are shown in Fig. 44. The parameter s is the free-space distance between the spheres so that $d = s + 2a$. Curves are shown for $s = 1$ nm ($a/d = 0.4545$) and $s = 4$ nm ($a/d = 0.3571$). The slow-wave region portions of the curves for $\Re(\beta d)$ from close to the light line to close to π are quite similar for the real and complex permittivity cases. Close to the light line, however, the behavior of the complex curves is quite different from what it is for the real permittivity curves. Whereas βd for the real permittivity curves decreases along the light line in the slow-wave region, in the complex permittivity dispersion curves $\Re(\beta d)$ crosses the light line into the fast-wave region, decreases to zero, and then increases again to meet the light line where the curves end. The fast-wave region traveling waves are significantly attenuated. The propagation constants also differ significantly for $\Re(\beta d)$ close to π. For the real permittivity nanospheres there is a sharp cut-off, while for the complex permittivity nanospheres for very low frequencies there is a strongly attenuated wave that gradually becomes less attenuated as the frequency increases and a region with small attenuation begins.

The kd–βd curves for a 1D array of glass-embedded silver nanospheres and electric dipoles parallel to the array axis with only the real part of the permittivity used and βd real are given in [20, fig. 32],[21, fig. 20] which we reproduce here as Fig. 45. The corresponding curves for glass-embedded silver nanospheres using complex permittivity and complex βd are shown in Fig. 46. The addition of loss and the extension of the dispersion diagram into the fast-wave region results in marked changes from the lossless dispersion diagram. The low-frequency portion of the lossless diagram very close to the light line is eliminated and replaced by a small "fish-hook" section in the fast-wave region. This fish-hook region is shown in detail in Fig. 47. Note the discontinuity of the real and imaginary parts of βd at the light line. Following this fast-wave fish hook there is a long positive-slope slow-wave region with $\Im(\beta d)$ small. Then $\Im(\beta d)$ begins to increase steadily. First there is a frequency range for which $\Re(\beta d)$ remains fairly close to π, after which with increasing frequency $\Re(\beta d)$ decreases as a negative-slope wave to the light line with $\Im(\beta d)$ steadily increasing to very large values (not shown in the figure).

As an example of the various kd–βd diagrams that are obtained when alternative branches of the dilogarithm and trilogarithm functions are employed, in Fig. 48 we show the curves of Fig. 46

(in black) along with a number of curves (in color) obtained with different choices of the parameters $m_2 = 0, \pm 1$ and $m_3 = 0, \pm 1$, $(m_2, m_3) \neq (0, 0)$, in (7.13*a*) and (7.13*b*). Note the curious behavior of these alternative branch curves which end suddenly.

8.3.2 2D ARRAYS OF SILVER NANOSPHERES

The kd–βd curves for 2D arrays of glass-embedded lossless silver nanospheres with electric and magnetic dipoles perpendicular to the array axis, the electric dipoles parallel to the array plane, only the real part of the permittivity used, and βd real, are given in [20, fig. 29],[21, fig. 17] which we reproduce here as Fig. 49. The corresponding curve for complex βd and lossy silver nanospheres and $s = 1$ nm ($a/d = 0.4545$) is shown in Fig. 50. The behavior of the lossy dispersion diagram is different in an important respect from that of the 1D case. Close to the light line there are two distinct branches of the diagram. The plot of the upper branch of $\Re(\beta d)$ crosses the light line and decreases asymptotically to zero as kd increases, while the imaginary part of βd becomes increasingly negative. For low frequencies the lower branch starts out very close to the light line just as it does for the lossless case with $\Im(\beta d) = 0$, but then as kd continues to increase there is a small region in the slow-wave region (kd from ≈ 0.182 to 0.216) where there is a complex wave with positive $\Im(\beta d)$. Close to $\Re(\beta d) = \pi$ the behavior of the dispersion diagram is similar to that of Fig. 28, where for very low frequencies there is a strongly attenuated wave that gradually becomes less attenuated as the frequency increases until $kd \approx 0.190$ and a weakly attenuated region begins. In Fig. 51 we show the kd–βd diagram for the same array but with multiple modes displayed. The corresponding dispersion diagrams for the larger sphere separation distance, $s = 4$ nm, are similar in all important respects to those of the $s = 1$ dispersion diagram apart from an expected displacement of the curve to higher frequencies, and are not shown here.

For comparison with Fig. 50, in Fig. 52 we show the extension of the kd–βd diagram of Fig. 49 for complex βd but using only the real part of the permittivity instead of the complex permittivity used to obtain the dispersion diagram of Fig. 50. Instead of $\Re(\beta d)$ increasing from the light line and then hooking back to it as it does in Fig. 50, $\Re(\beta d)$ continues to increase smoothly to π, joining up with the upper branch of the diagram at $\Re(\beta d) = 1.09$. Also, almost all the portion of the dispersion diagram of Fig. 50 down along $\Re(\beta d) \approx \pi$ is eliminated. The small branch of $\Im(\beta d)$ going to the left of the $\Im(\beta d)$ axis at around $kd = 0.2$ corresponds to the very small interval of $\Re(\beta d)$ along $\Re(\beta d) = \pi$ in this range of kd.

The kd–βd curves for 2D arrays of glass-embedded lossless silver nanospheres with electric and magnetic dipoles perpendicular to the array axis and the electric dipoles perpendicular to the array plane are given in [20, fig. 29],[21, fig. 29] which we reproduce here as Fig. 53. The corresponding curve for lossy silver nanospheres and $s = 1$ nm ($a/d = 0.4545$) is shown in Fig. 54. Again there are two branches of the lossy dispersion diagram. The behavior of the upper branch here is very similar to that of the dispersion diagrams for the 1D array of silver nanospheres shown in Fig. 44 with $\Re(\beta d)$ continuing to decrease from the light line in the fast-wave region to zero before increasing to meet the light line again where the curve ends. The behavior of the lower branch of the lossy dispersion diagram resembles that of Fig. 50, starting out for low frequencies very close to the light line just as it does for the lossless case with $\Im(\beta d)$ close to 0, but then as kd continues to increase entering a small region in the slow-wave region (kd from ≈ 0.324 to 0.326) where there is a complex wave with positive $\Im(\beta d)$. The behavior of the diagram close to $\Re(\beta d) = \pi$ is similar to that shown in Figs. 28 and 32. In Fig. 55 we show the kd–βd diagram for the same array but with multiple modes displayed. For the larger separation distance, $s = 4$ nm, the dispersion diagram shown in Fig. 56 is completely similar to that of the smaller separation diagram in Fig. 54 apart from an expected shift in the direction of higher frequency. The kd–βd curves for 2D

arrays of glass-embedded silver nanospheres with electric dipoles parallel to the array axis, only the real part of the permittivity used, and βd real, are given in [20, fig. 21],[21, fig. 33] which we reproduce here as Fig. 57. The corresponding curves (in black) for complex βd and lossy silver nanospheres are shown in Fig. 58. Just as for the 1D case of a glass-embedded silver nanosphere array with electric dipoles parallel to the array axis, there is a very marked difference between the real permittivity and lossy dispersion diagrams. For the lossy case, $\Re(\beta d)$ begins at the light line as in the real permittivity case and increases as a forward wave with fairly small positive $\Im(\beta d)$ until $\Re(\beta d)$ approaches π. Then $\Im(\beta d)$ steadily increases and $\Re(\beta d)$ exhibits a curious behavior, first remaining close to π as the frequency increases, then decreasing to about 2.5, and then remaining close to there with increasing kd. In contrast to the 1D case of a glass-embedded silver nanosphere array with electric dipoles parallel to the array axis (Figs. 46 and 47) there does not appear to be any fish-hook extension of the $\Re(\beta d)$ curves into the fast-wave region close to the light line.

In this same figure, for the $s = 1$ nm array we show kd–βd curves obtained when the Schlömilch series with $H_0^{(1)}$ and $H_2^{(1)}$ in (3.34) are evaluated using (3.14) and (3.16) using an alternative branch of $\sqrt{\beta_0^2 - 1}$ rather than the principal branch. The red curves are obtained when $-\sqrt{\beta_0^2 - 1}$ is used instead of $+\sqrt{\beta_0^2 - 1}$ in both (3.14) and (3.16), and the green [blue] curves are obtained when $-\sqrt{\beta_0^2 - 1}$ is used instead of $+\sqrt{\beta_0^2 - 1}$ in just (3.14) [(3.16)]. Solid and dotted lines are used to indicate $\Re(\beta d)$ and $\Im(\beta d)$, respectively. Of especial interest is the way in which the red curves continue the black curves obtained using the principal branch of $\sqrt{\beta_0^2 - 1}$. It is also seen that the green curves divide into two branches just to the right of the light line, with one branch for $\Re(\beta d)$ traveling up very close to the light line, and the other branch for both $\Re(\beta d)$ and $\Im(\beta d)$ joining up with the respective black curves. For the blue curve, $\Re(\beta d)$ decreases from 0.87 to 0 as kd increases from 0 to 0.21.

8.3.3 3D ARRAYS OF SILVER NANOSPHERES

The kd–βd curves for 3D arrays of glass-embedded silver nanospheres with electric and magnetic dipoles perpendicular to the array axis, only the real part of the permittivity used, and βd real, are given in [20, fig. 31],[21, fig. 19], reproduced here as Fig. 59, and the corresponding curves for lossy nanospheres and complex βd are shown in Fig. 60. As for the 1D and 2D cases, the behavior of the 3D lossy curves differ strongly from the corresponding real permittivity curves. For the complex permittivity case, as for the real permittivity case, the curves begin close to the light line, but $\Re(\beta d)$ instead of continuing to π increases only a little beyond 1.0 followed by an interval of increasing kd in which it crosses the light line and decreases to close to zero. After this, with still further increase in frequency, $\Re(\beta d)$ increases again, re-crosses the light line, and then remains quite close to the light line. $\Im(\beta d)$ is close to zero during the initial increase of $\Re(\beta d)$, then increases very rapidly to around 1.0 after which it decreases with increasing frequency to close to zero where $\Re(\beta d)$ begins its increase from close to zero, and remains increasingly close to zero thereafter.

The kd–βd curves for 3D arrays of glass-embedded silver nanospheres with the electric dipoles parallel to the array axis, only the real part of the permittivity used, and βd real, are given in [20, fig. 34],[21, fig. 22], reproduced here as Fig. 61, and the corresponding curves for lossy nanospheres and complex βd are shown in Fig. 62. The lossy dispersion diagrams differ greatly from the corresponding lossless diagrams. Instead of βd going from 0 to π in an extremely narrow frequency range, here for very low frequencies $\Re(\beta d)$ begins close to zero with $\Im(\beta d)$ very large. As the frequency increases $\Re(\beta d)$ begins to increase, crosses the light line, and continues to increase until close to π. The portion of the curves from a little before they cross the light line to where they reach close to π correspond to the curves for the lossless case. The imaginary part of βd is

fairly small in this portion of the dispersion curves. As kd continues to increase $\Im(\beta d)$ increases rapidly. $\Re(\beta d)$ stays close to π for awhile, and then decreases, somewhat rapidly at first and then much more slowly.

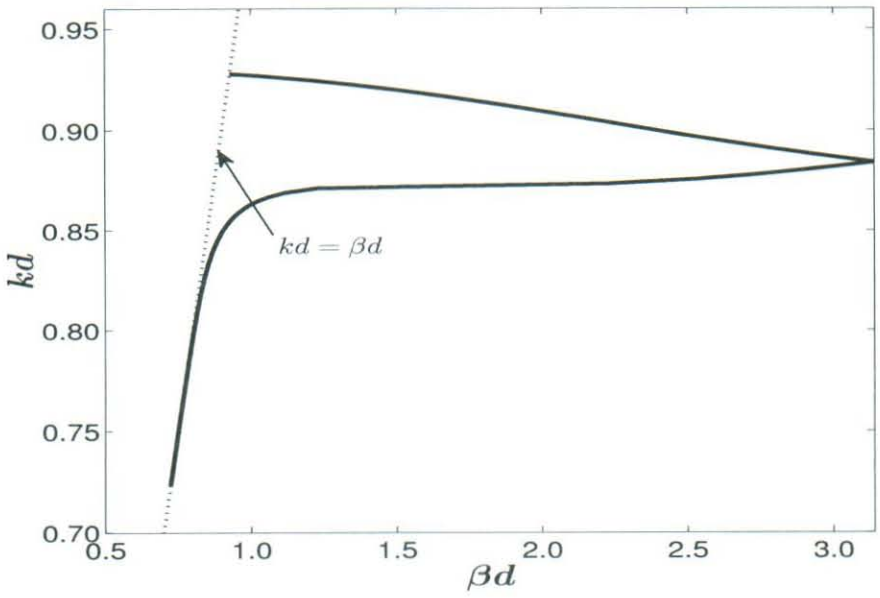

Figure 2: kd–βd diagram for a 1D periodic array of magnetodielectric spheres with $\epsilon_r = \mu_r = 10$, and $a/d = 0.45$; dipoles perpendicular to array axis; βd real.

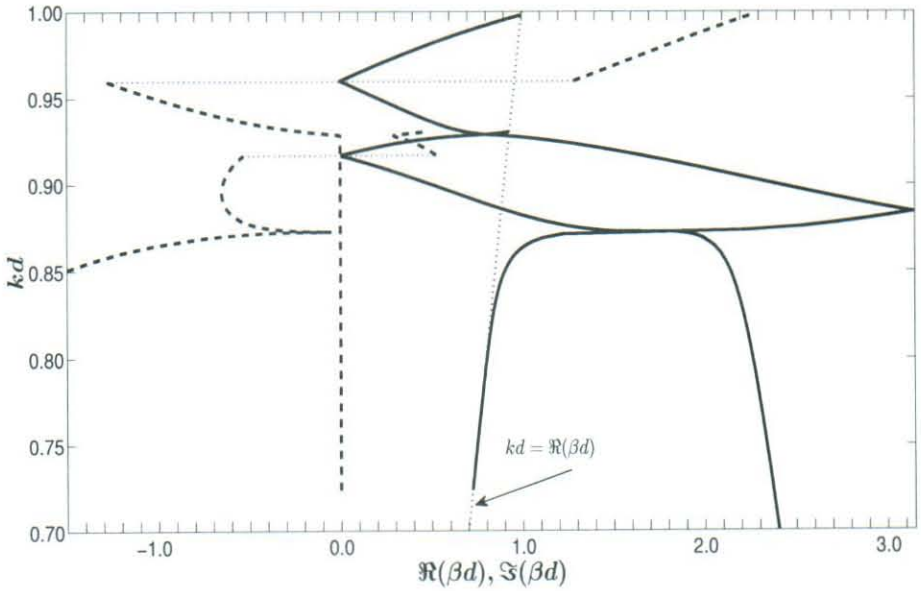

Figure 3: kd–βd diagram for a 1D periodic array of magnetodielectric spheres with $\epsilon_r = \mu_r = 10$, and $a/d = 0.45$; dipoles perpendicular to array axis; βd complex.

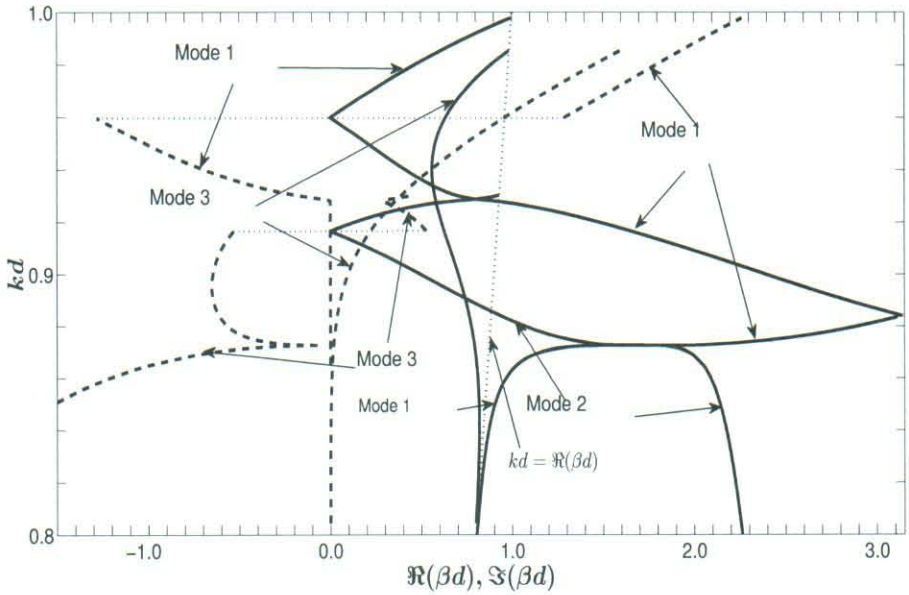

Figure 4: kd–βd diagram for a 1D periodic array of magnetodielectric spheres with $\epsilon_{\mathrm{r}} = \mu_{\mathrm{r}} = 10$, and $a/d = 0.45$; dipoles perpendicular to array axis; βd complex. Multiple modes shown.

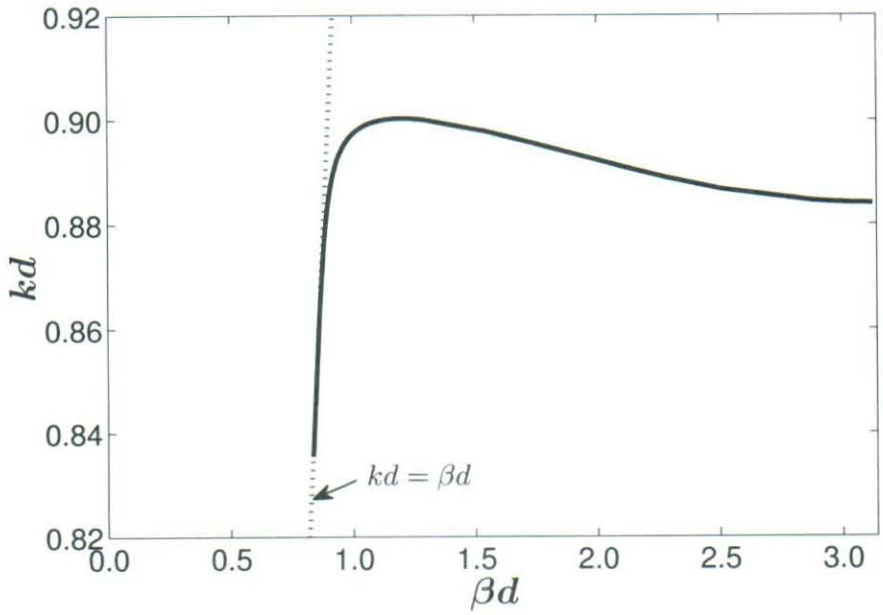

Figure 5: kd–βd diagram for a 1D periodic array of magnetodielectric spheres with $\epsilon_r = \mu_r = 10$, and $a/d = 0.45$; electric dipoles only; βd real.

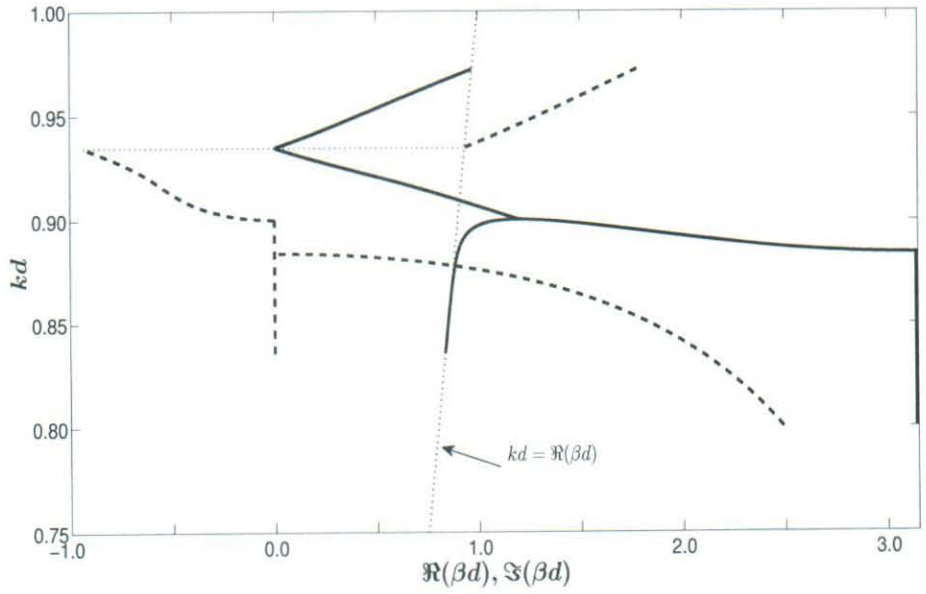

Figure 6: kd–βd diagram for a 1D periodic array of magnetodielectric spheres with $\epsilon_r = \mu_r = 10$, and $a/d = 0.45$; electric dipoles only; βd complex.

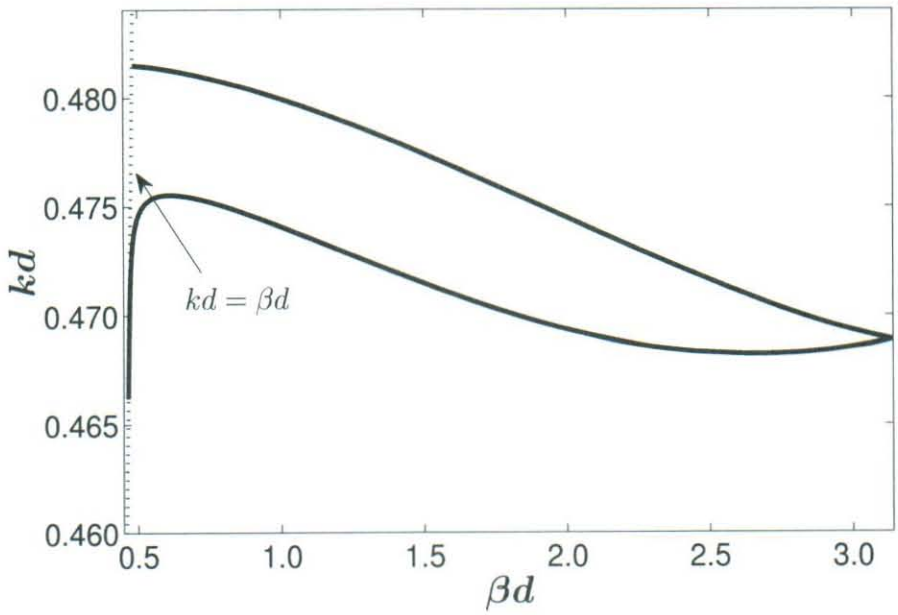

Figure 7: kd–βd diagram for a 1D periodic array of magnetodielectric spheres with $\epsilon_r = \mu_r = 20$, and $a/d = 0.45$; dipoles perpendicular to array axis; βd real.

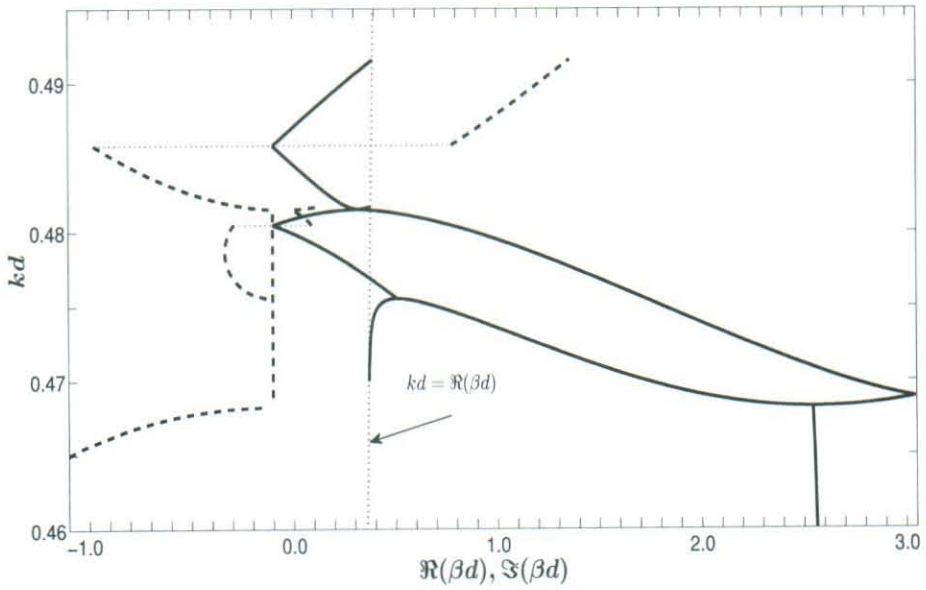

Figure 8: kd–βd diagram for a 1D periodic array of magnetodielectric spheres with $\epsilon_r = \mu_r = 20$, and $a/d = 0.45$; dipoles perpendicular to array axis; βd complex.

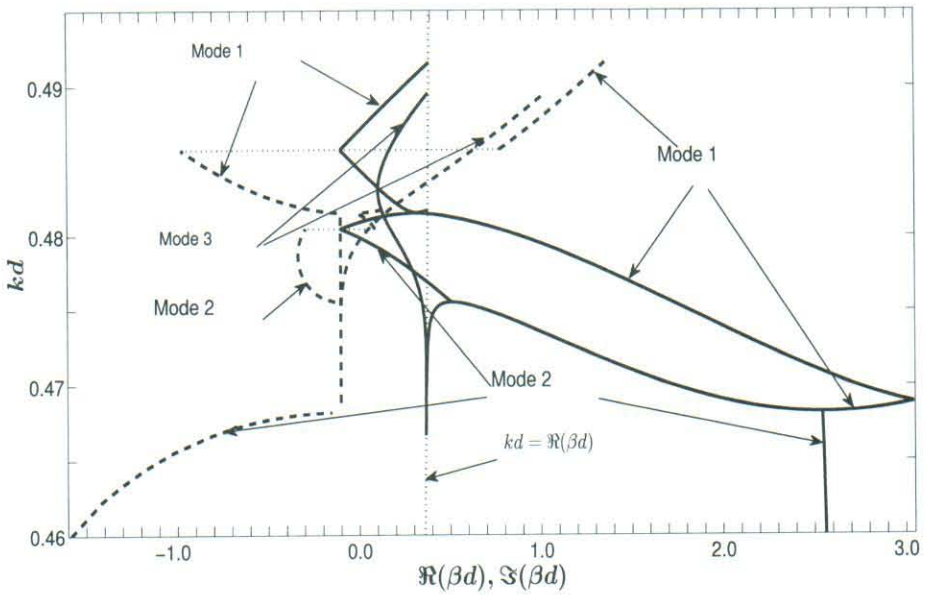

Figure 9: kd–βd diagram for a 1D periodic array of magnetodielectric spheres with $\epsilon_r = \mu_r = 20$, and $a/d = 0.45$; dipoles perpendicular to array axis; βd complex. Multiple modes shown.

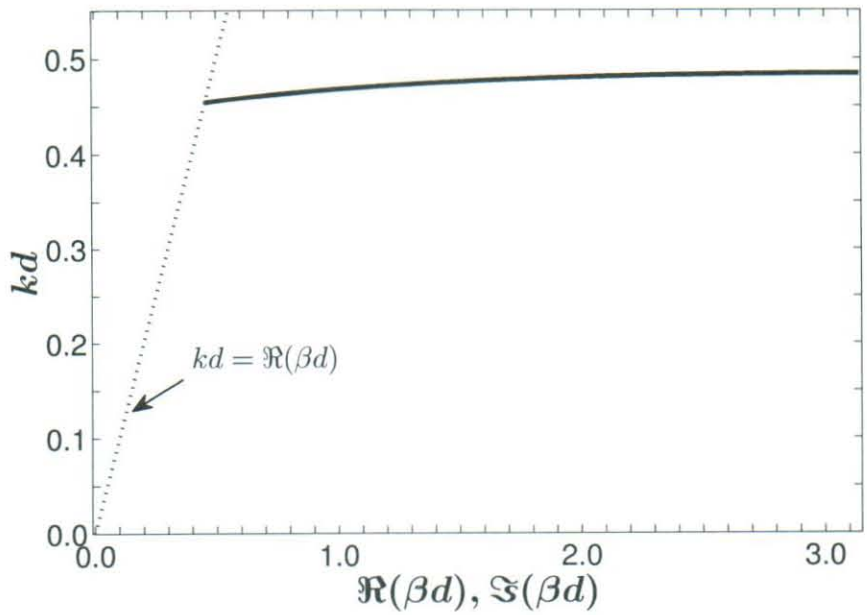

Figure 10: kd–βd diagram for a 1D periodic array of magnetodielectric spheres with $\epsilon_r = \mu_r = 20$ and $a/d = 0.45$; dipole moments parallel to propagation direction; βd real.

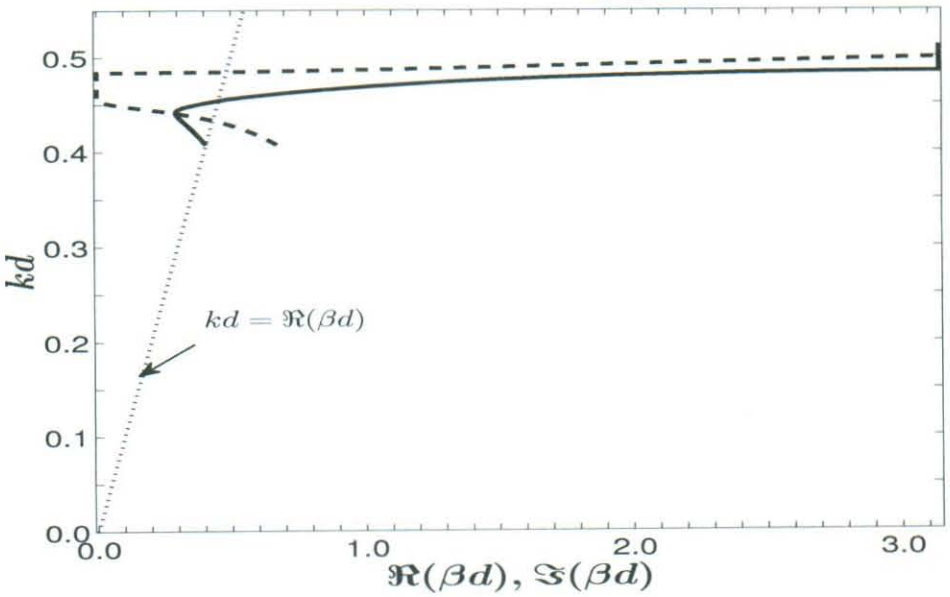

Figure 11: kd–βd diagram for a 1D periodic array of magnetodielectric spheres with $\epsilon_r = \mu_r = 20$ and $a/d = 0.45$; dipole moments parallel to propagation direction; βd complex.

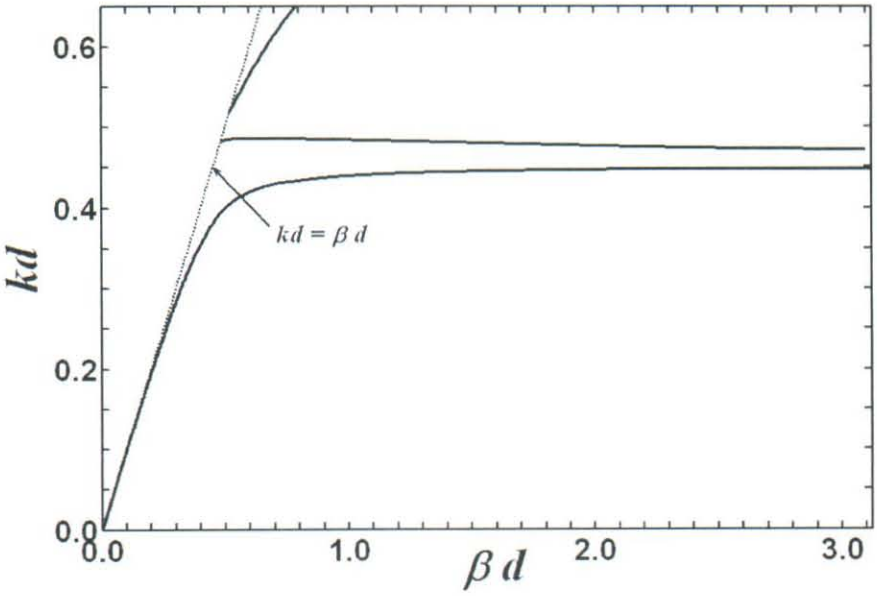

Figure 12: kd–βd diagram for a 2D square-lattice array of magnetodielectric spheres with $\epsilon_r = \mu_r = 20$ and $a/d = .45$; electric dipole moments parallel or perpendicular to the array plane; βd real.

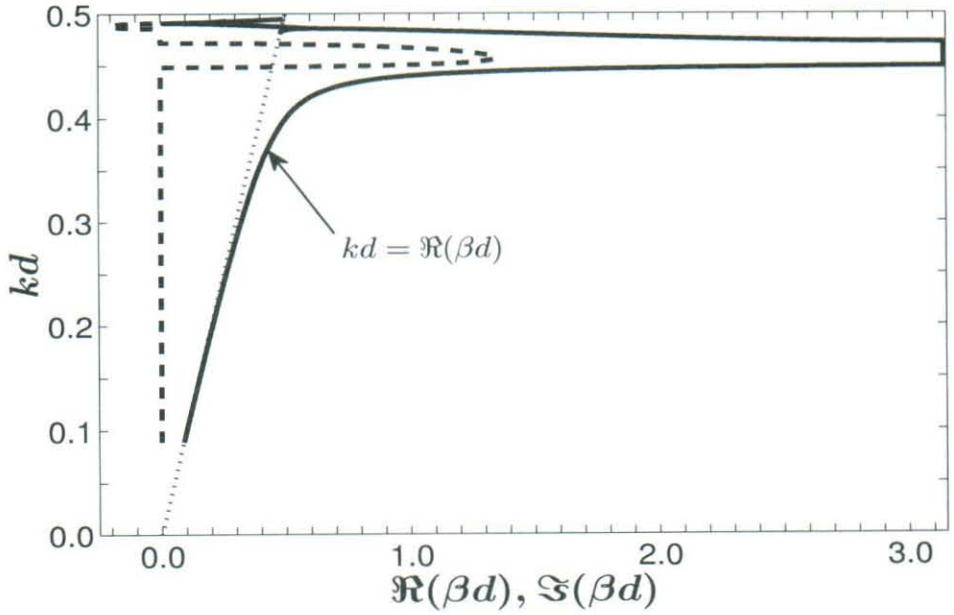

Figure 13: kd–βd diagram for a 2D square-lattice array of magnetodielectric spheres with $\epsilon_r = \mu_r = 20$ and $a/d = .45$; electric dipole moments parallel or perpendicular to the array plane; βd complex.

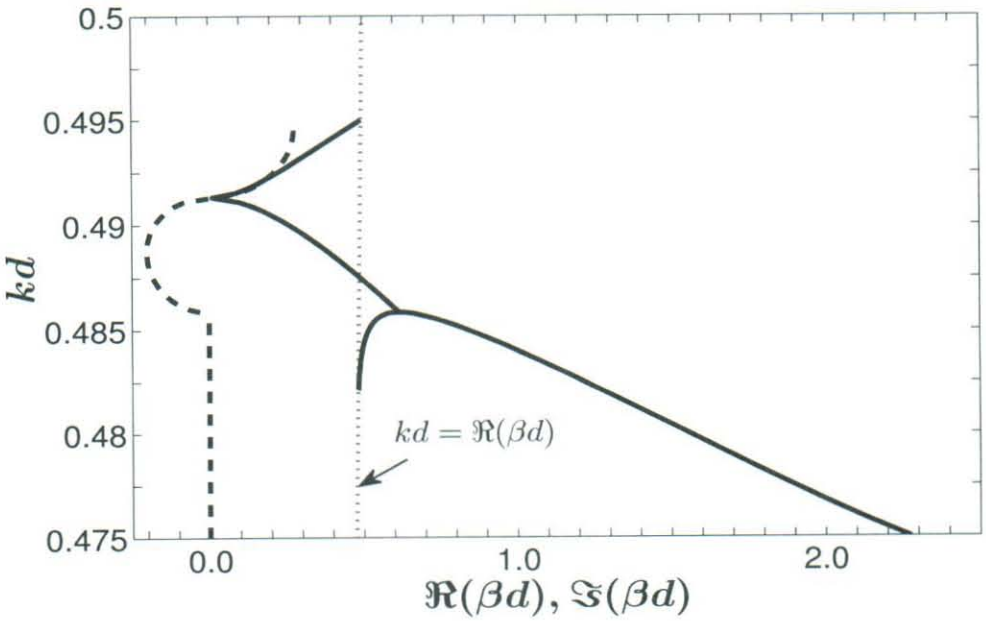

Figure 14: kd–βd diagram for a 2D square-lattice array of magnetodielectric spheres with $\epsilon_r = \mu_r = 20$ and $a/d = .45$; electric dipole moments parallel or perpendicular to the array plane; βd complex; detail.

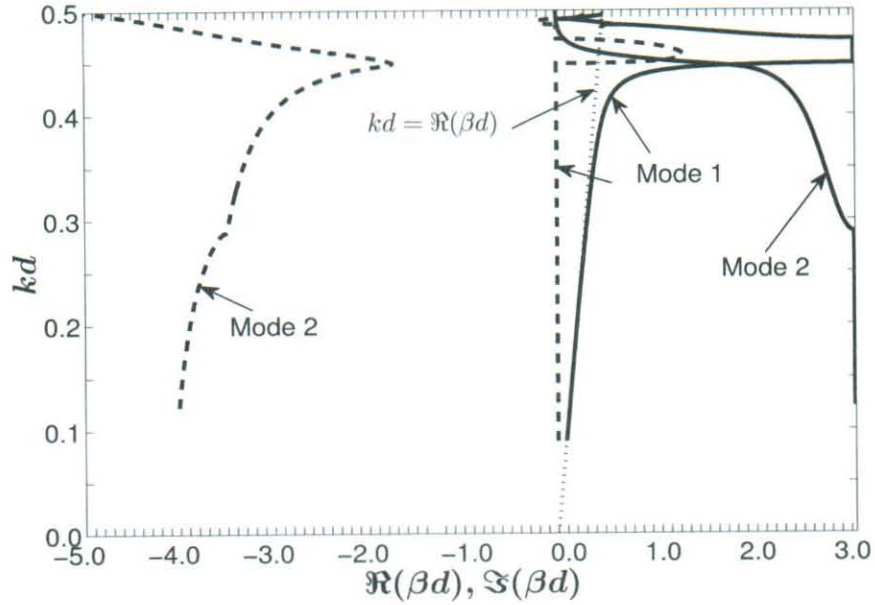

Figure 15: kd–βd diagram for a 2D square-lattice array of magnetodielectric spheres with $\epsilon_r = \mu_r = 20$ and $a/d = .45$; electric dipole moments parallel or perpendicular to the array plane; βd complex. Multiple modes shown.

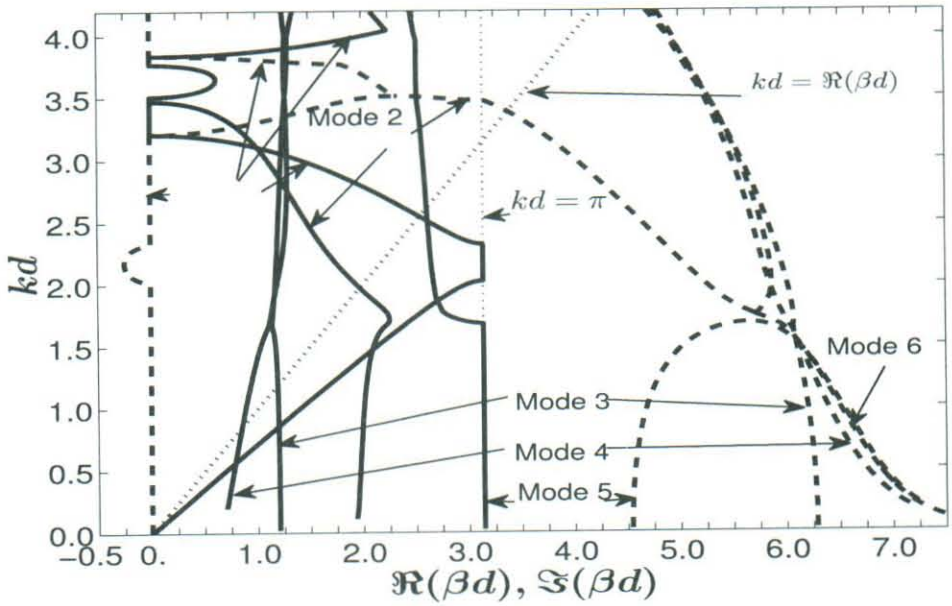

Figure 16: kd–βd diagram for a 2D square-lattice array of magnetodielectric spheres with $\epsilon_r = \mu_r = 20$ and $a/d = .45$; electric dipole moments parallel or perpendicular to the array plane; βd complex. Multiple modes shown; detail.

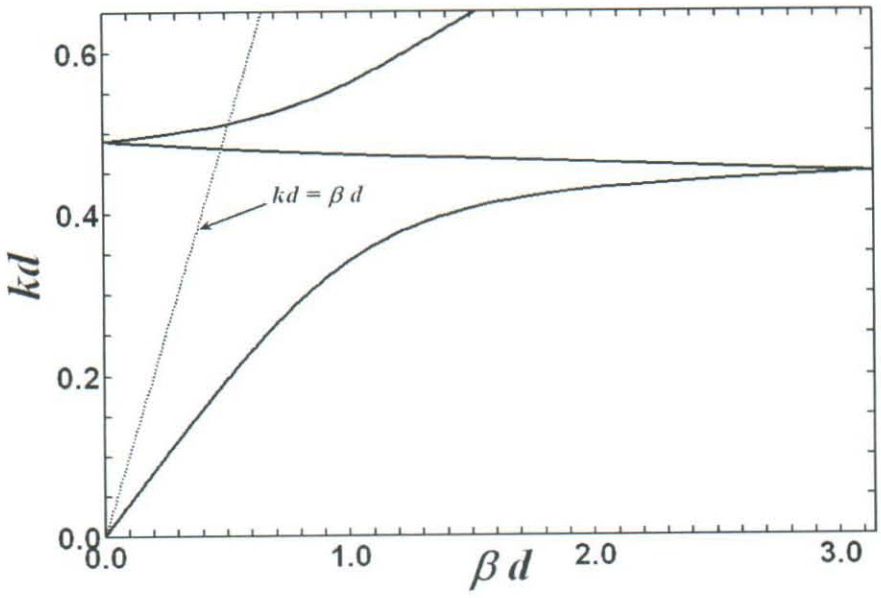

Figure 17: kd–βd diagram for a 3D cubic-lattice array of $\epsilon_r = \mu_r = 20$ magnetodielectric spheres (dipole moments normal to the propagation direction) with $a/d = .45$; βd real.

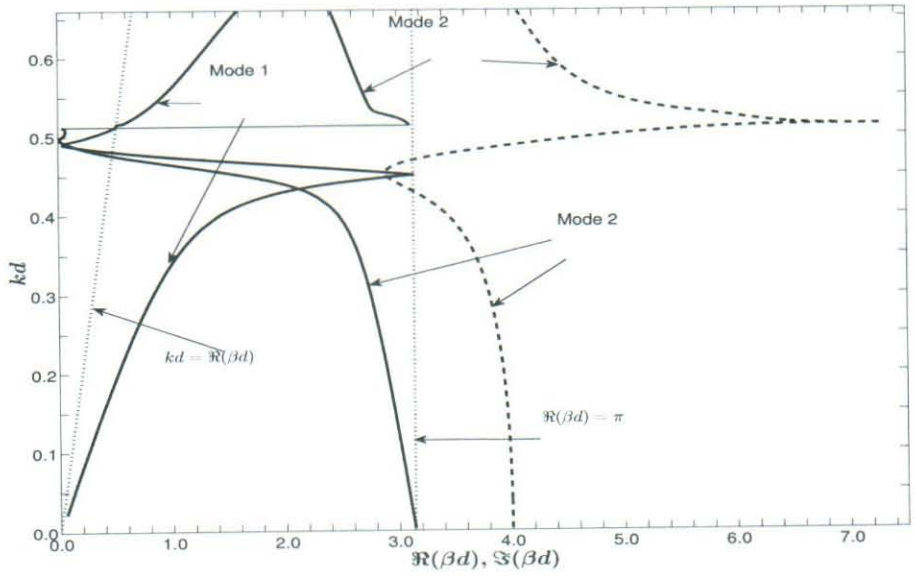

Figure 18: kd–βd diagram for a 3D cubic-lattice array of $\epsilon_r = \mu_r = 20$ magnetodielectric spheres (dipole moments normal to the propagation direction) with $a/d = .45$; βd complex. Multiple modes shown.

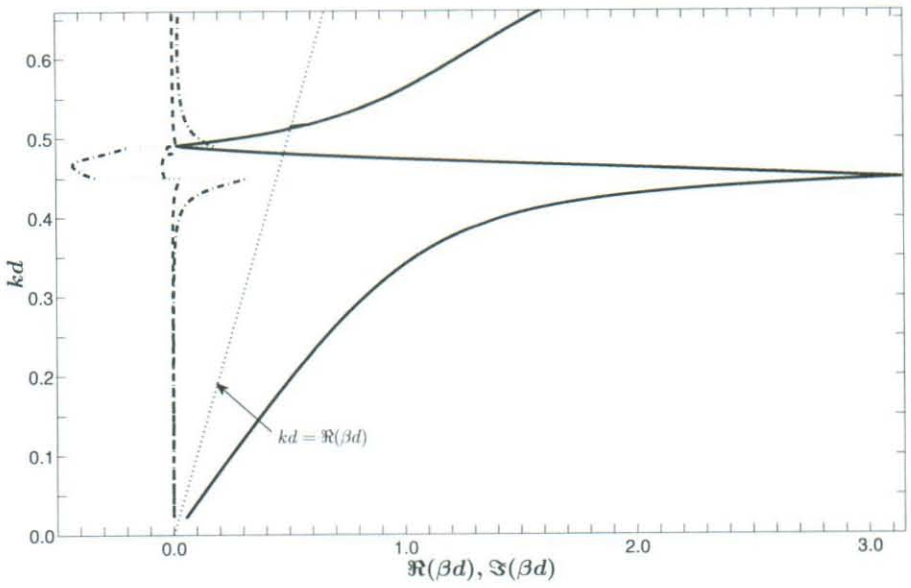

Figure 19: kd–βd diagram for 3D cubic-lattice arrays of ($\epsilon_r = 20.0, \mu_r = 20.0 + 0.04i$), ($\epsilon_r = 20.0, \mu_r = 20.0 + 0.4i$), magnetodielectric spheres (dipole moments normal to the propagation direction) with $a/d = .45$; βd complex.

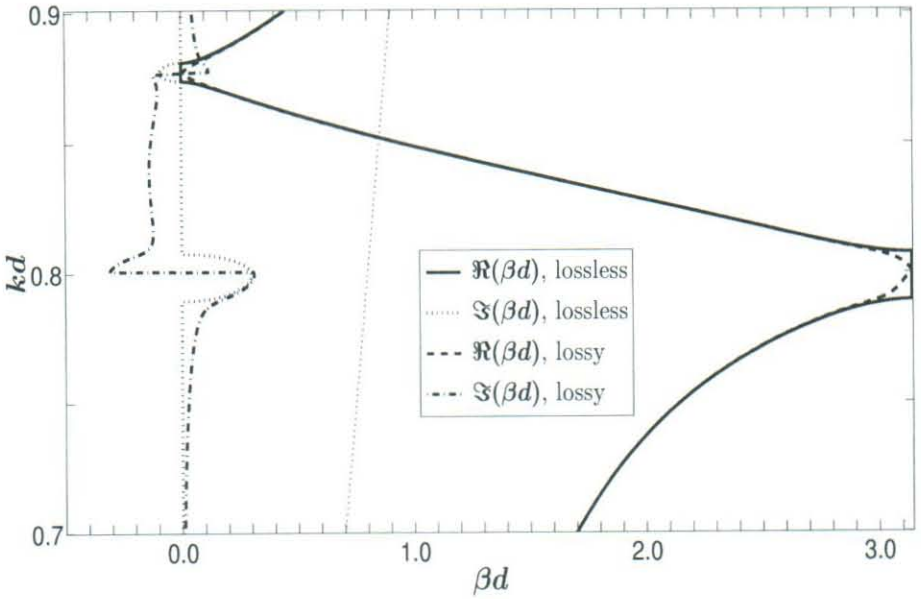

Figure 20: kd–βd curves for 3D cubic-lattice arrays of magnetodielectric spheres; 1) $\epsilon_{\rm r} = (13.8, 0.0)$, $\mu_{\rm r} = (11.0, 0.0)$; 2) $\epsilon_{\rm r} = (13.8, 0.1)$, $\mu_{\rm r} = (11.0, 0.0)$; dipole moments perpendicular to array axis; $a/d = 0.4$.

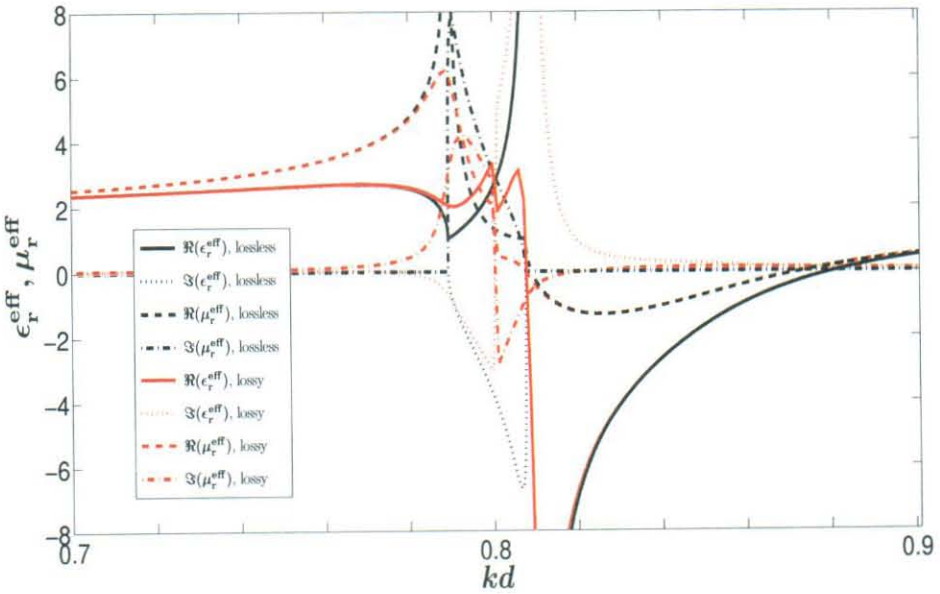

Figure 21: Effective permeability and permeability of 3D cubic-lattice arrays of magnetodielectric spheres; 1) $\epsilon_{\rm r} = (13.8, 0.0)$, $\mu_{\rm r} = (11.0, 0.0)$; 2) $\epsilon_{\rm r} = (13.8, 0.1)$, $\mu_{\rm r} = (11.0, 0.0)$; dipole moments perpendicular to array axis; $a/d = 0.4$.

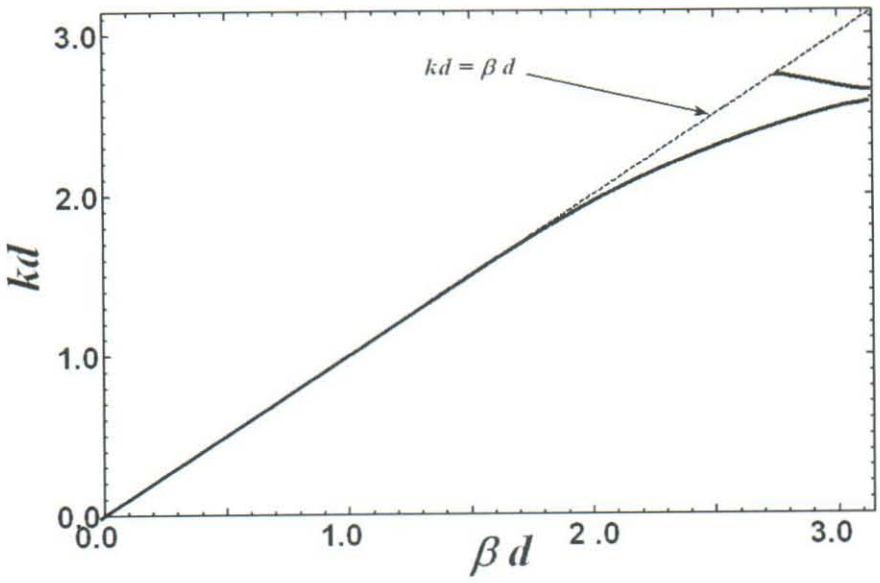

Figure 22: kd–βd diagram for a 1D periodic array of diamond spheres; dipole moments normal to the propagation direction; $a/d = .45$; βd real.

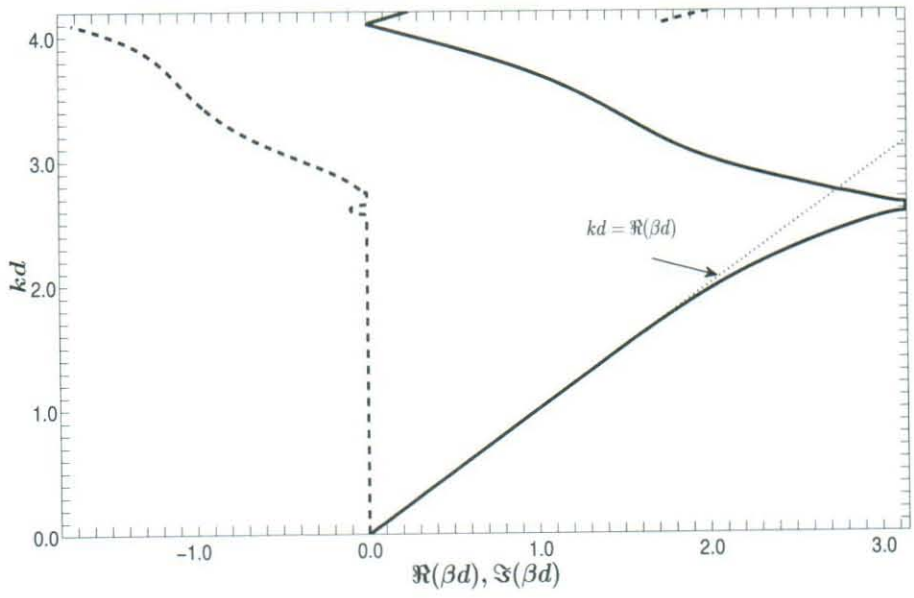

Figure 23: kd–βd diagram for a 1D periodic array of diamond spheres; dipole moments normal to the propagation direction; $a/d = .45$; βd complex.

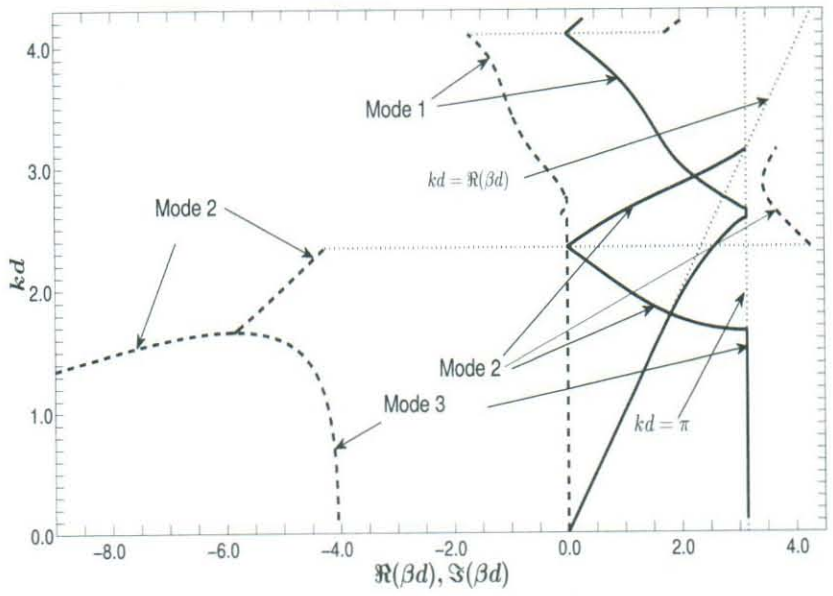

Figure 24: kd–βd diagram for a 1D periodic array of diamond spheres; dipole moments normal to the propagation direction; $a/d = .45$; βd complex. Multiple modes shown.

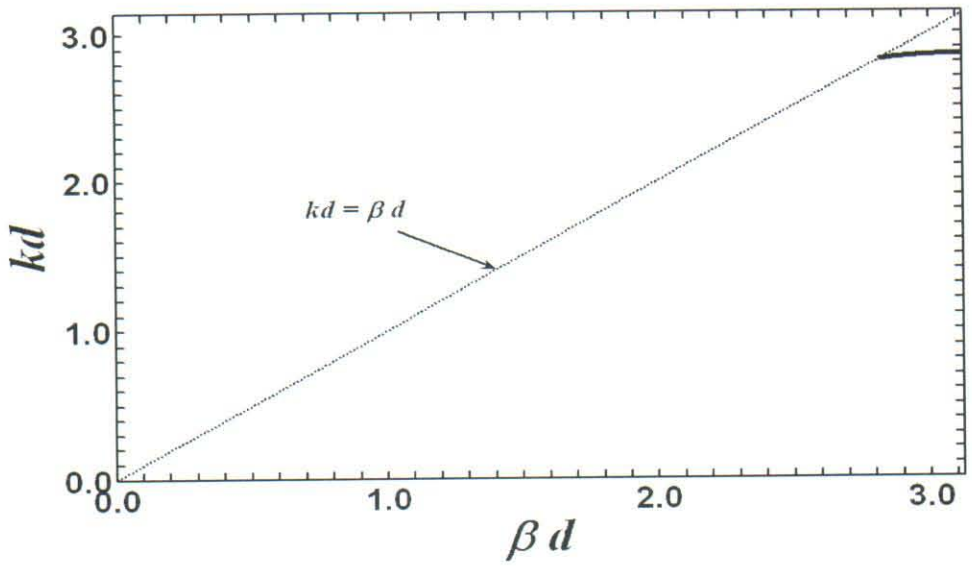

Figure 25: kd–βd diagram for a 1D periodic array of diamond spheres; magnetic dipole moments parallel to the propagation direction; $a/d = .45$; βd real.

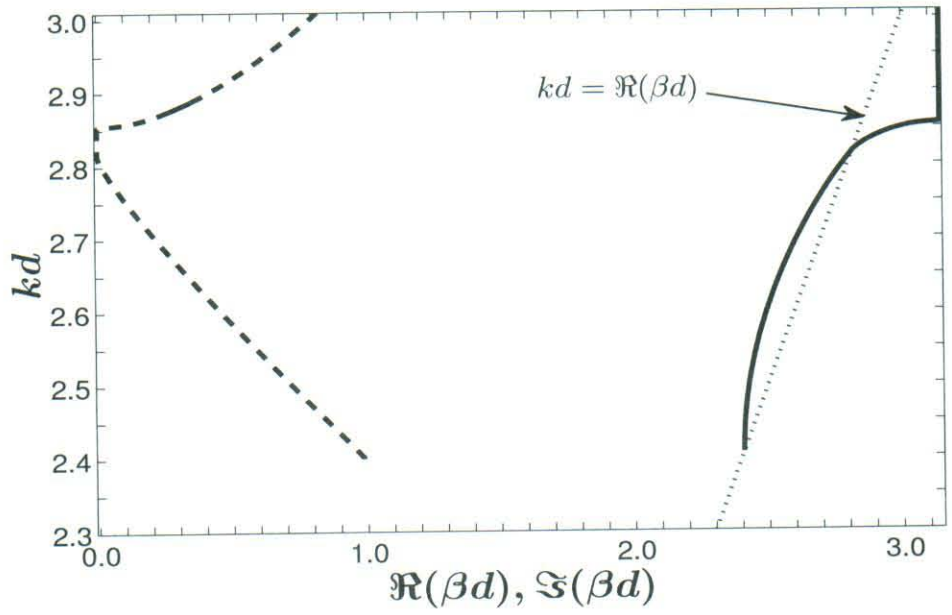

Figure 26: kd–βd diagram for a 1D periodic array of diamond spheres; magnetic dipole moments parallel to the propagation direction; $a/d = .45$; βd complex.

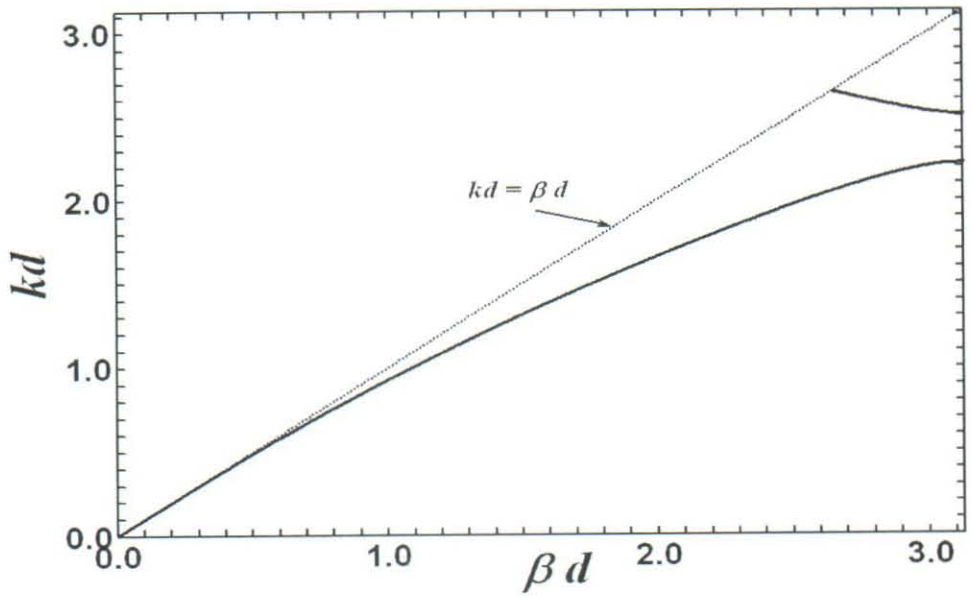

Figure 27: kd–βd diagram for a 2D square-lattice array of diamond spheres; electric dipole moments parallel to the array plane; $a/d = .45$; βd real.

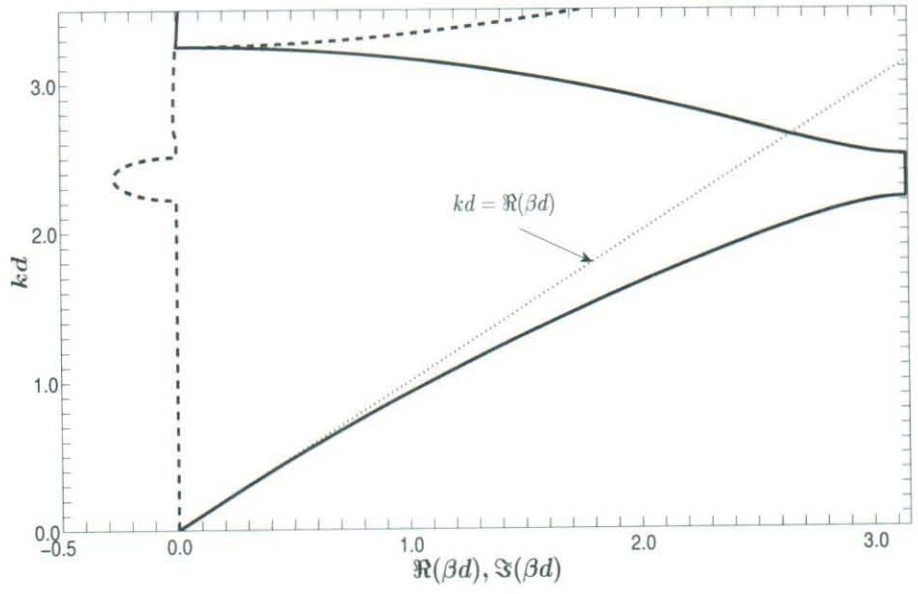

Figure 28: kd–βd diagram for a 2D square-lattice array of diamond spheres; electric dipole moments parallel to the array plane; $a/d = .45$; βd complex.

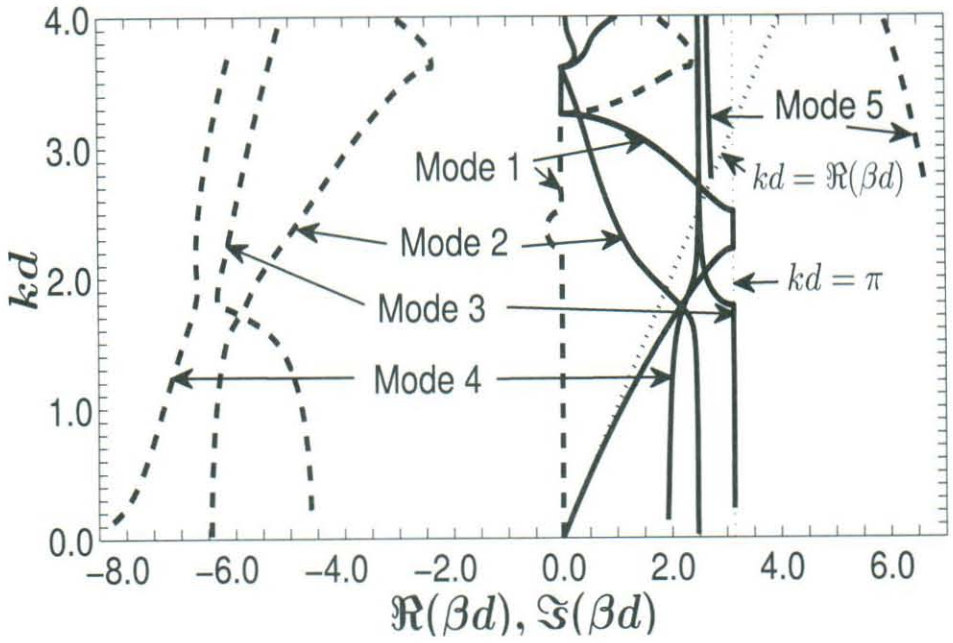

Figure 29: kd–βd diagram for a 2D square-lattice array of diamond spheres; electric dipole moments parallel to the array plane; $a/d = .45$; βd complex. Multiple modes shown.

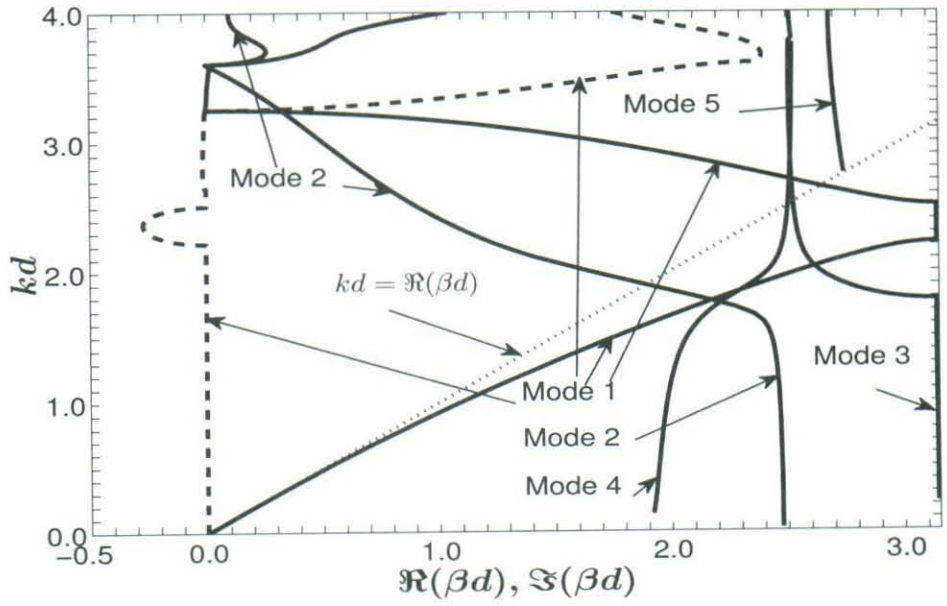

Figure 30: kd–βd diagram for a 2D square-lattice array of diamond spheres; electric dipole moments parallel to the array plane; $a/d = .45$; βd complex. Multiple modes shown; detail.

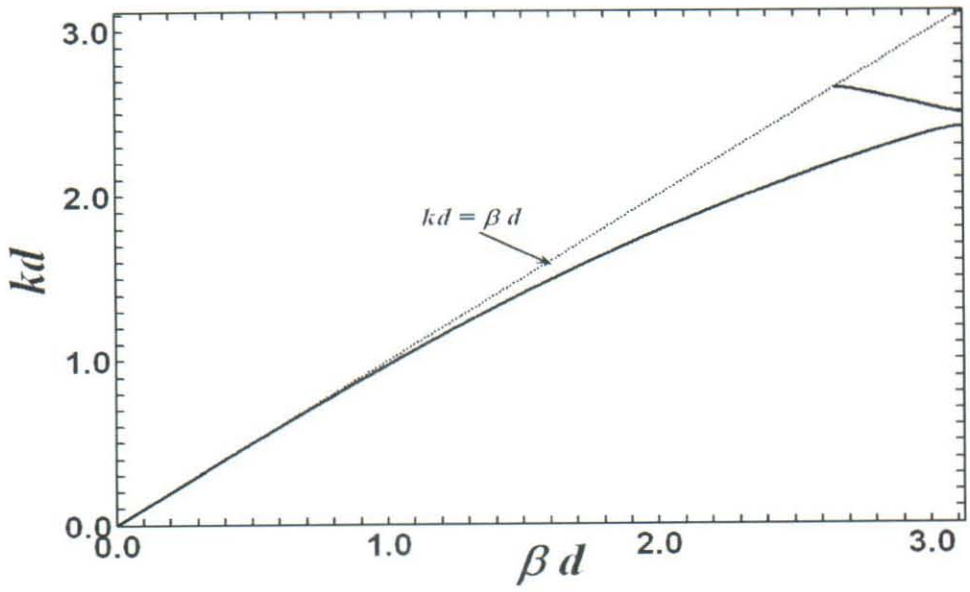

Figure 31: kd–βd diagram for a 2D square-lattice array of diamond spheres; electric dipole moments perpendicular to the array plane; $a/d = .45$; βd real.

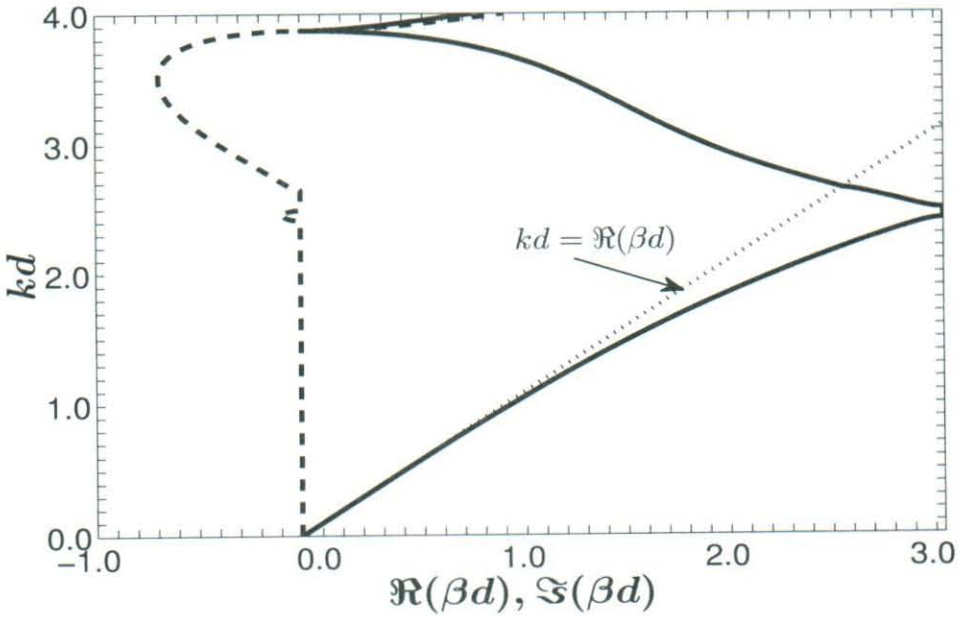

Figure 32: kd–βd diagram for a 2D square-lattice array of diamond spheres; electric dipole moments perpendicular to the array plane; $a/d = .45$; βd complex.

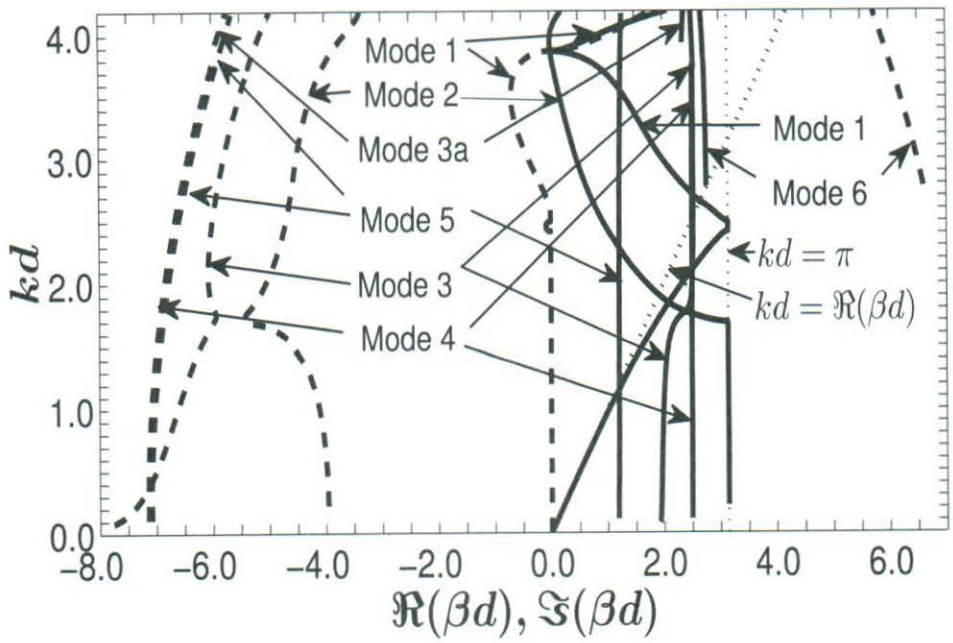

Figure 33: kd–βd diagram for a 2D square-lattice array of diamond spheres; electric dipole moments perpendicular to the array plane; $a/d = .45$; βd complex. Multiple modes shown.

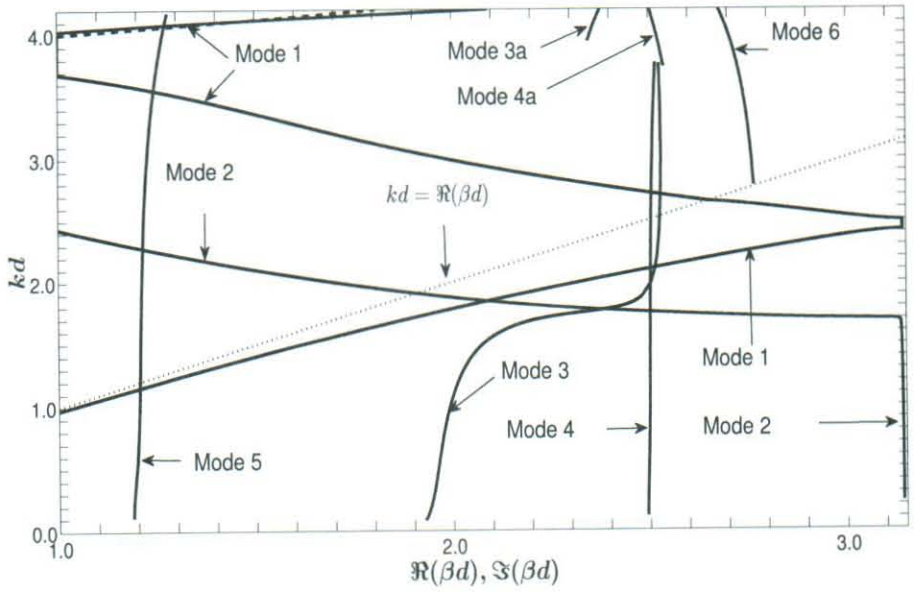

Figure 34: kd–βd diagram for a 2D square-lattice array of diamond spheres; electric dipole moments perpendicular to the array plane; $a/d = .45$; βd complex. Multiple modes shown; detail.

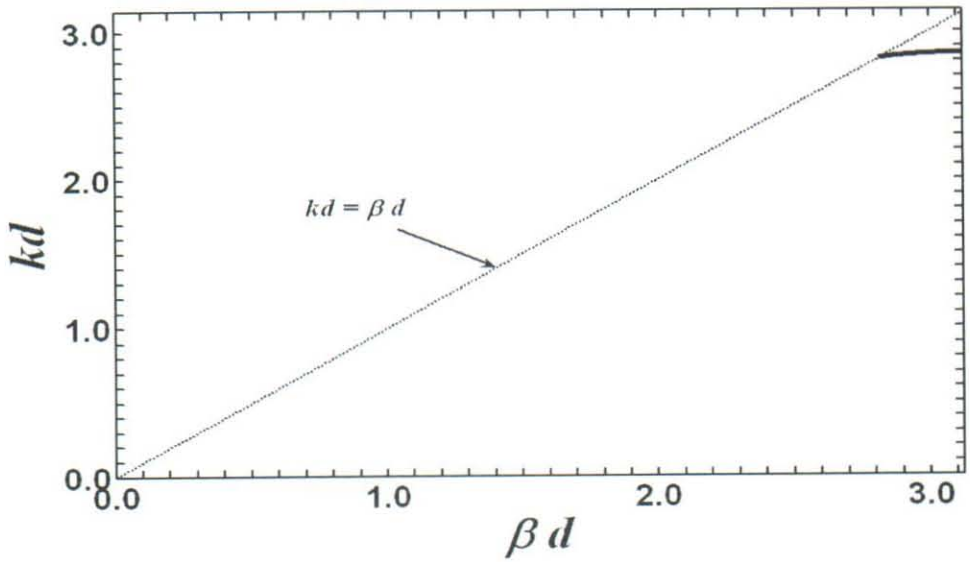

Figure 35: kd–βd diagram for a 2D square-lattice array of diamond spheres; magnetic dipole moments parallel to the propagation direction; $a/d = .45$; βd real.

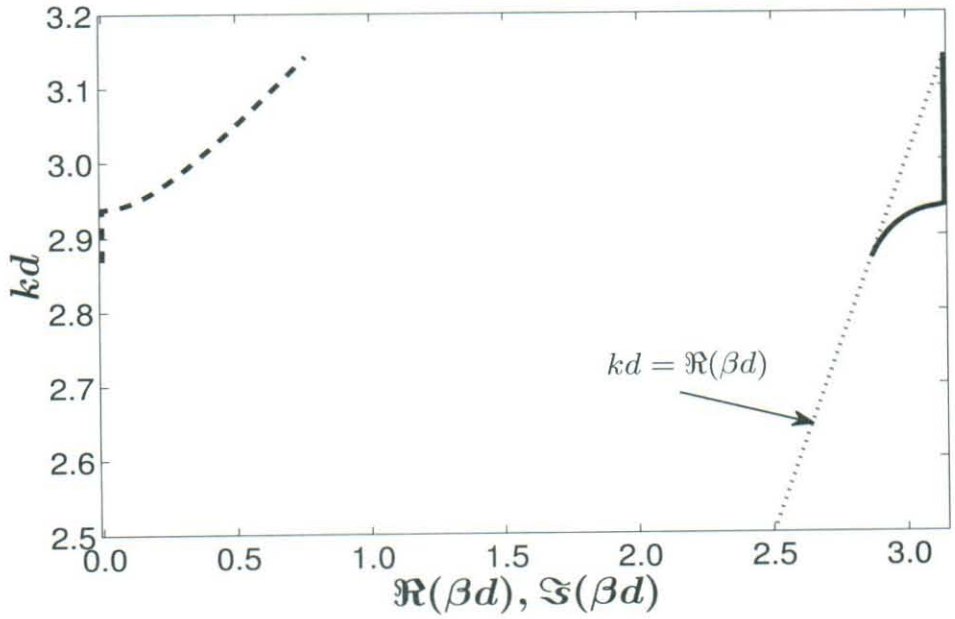

Figure 36: kd–βd diagram for a 2D square-lattice array of diamond spheres; magnetic dipole moments parallel to the propagation direction; $a/d = .45$; βd complex.

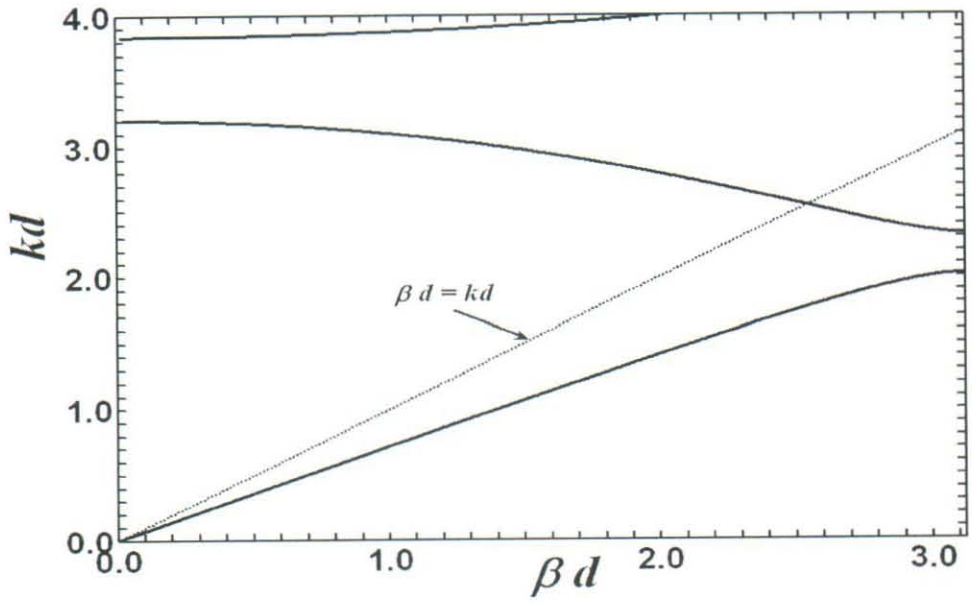

Figure 37: kd–βd diagram for a 3D cubic-lattice array of diamond spheres; dipole moments normal to the propagation direction; $a/d = .45$; βd real.

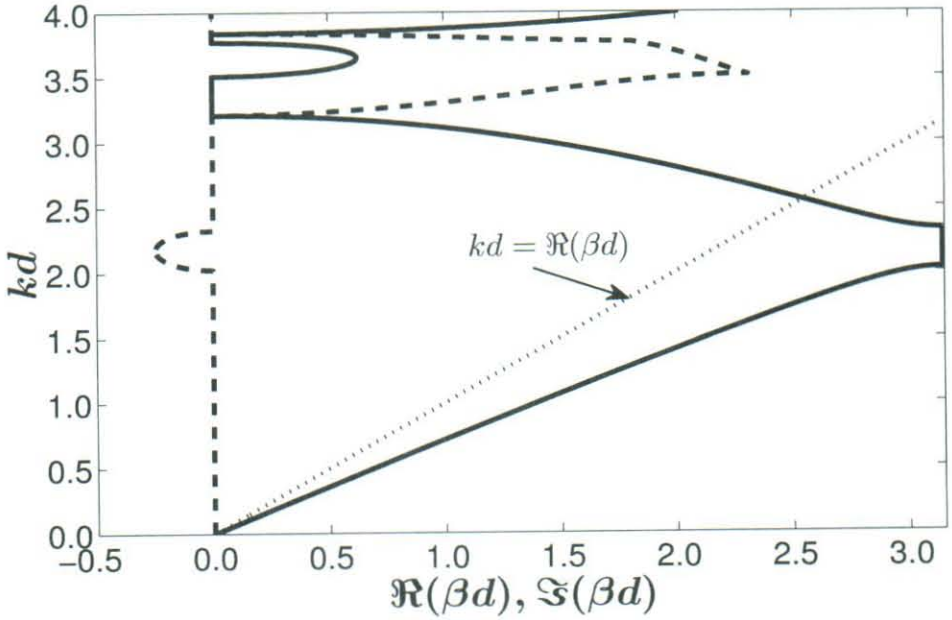

Figure 38: kd–βd diagram for a 3D cubic-lattice array of diamond spheres; dipole moments normal to the propagation direction; $a/d = .45$; βd complex.

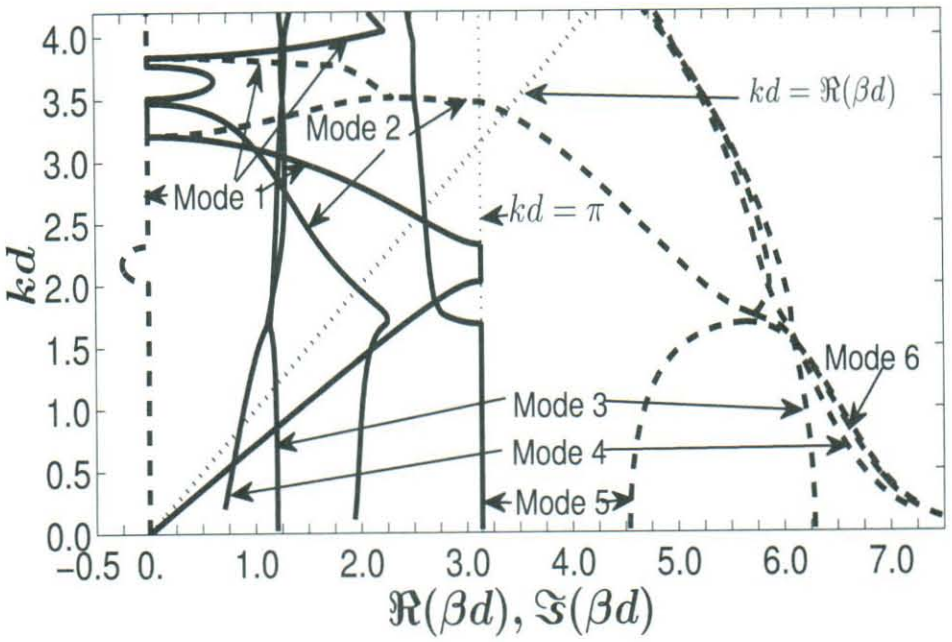

Figure 39: kd–βd diagram for a 3D cubic-lattice array of diamond spheres; dipole moments normal to the propagation direction; $a/d = .45$; βd complex. Multiple modes shown.

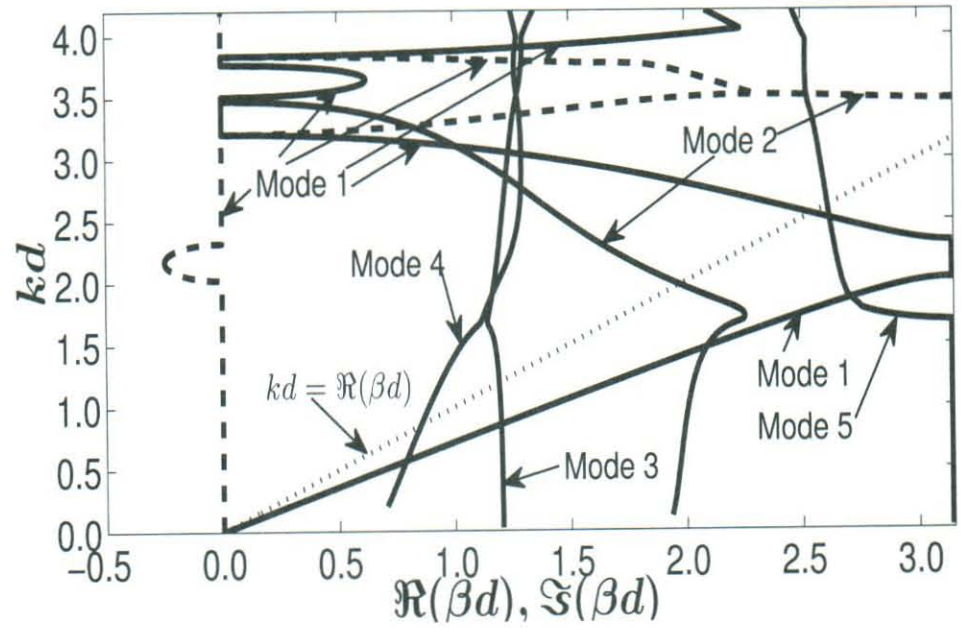

Figure 40: kd–βd diagram for a 3D cubic-lattice array of diamond spheres; dipole moments normal to the propagation direction; $a/d = .45$; βd complex. Multiple modes shown; detail.

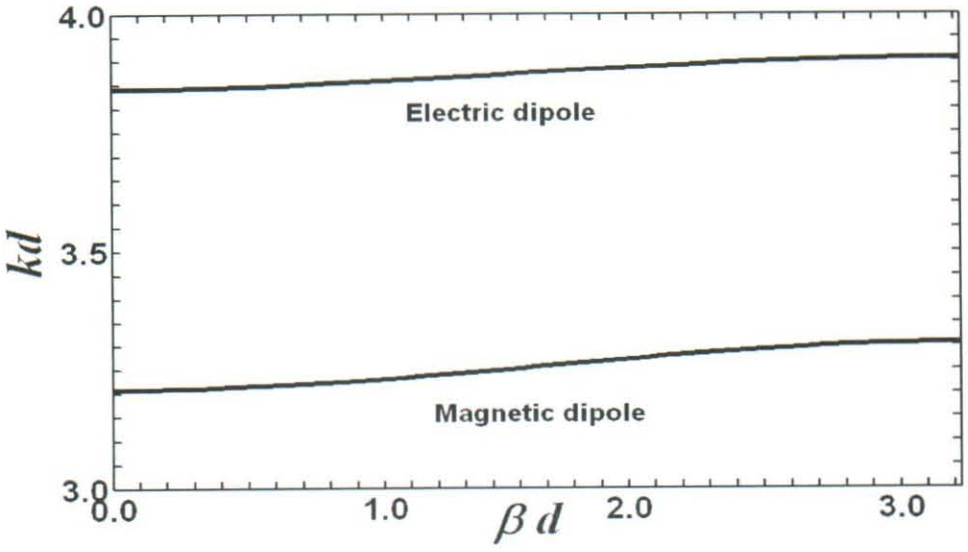

Figure 41: kd–βd diagram for a 3D cubic-lattice array of diamond spheres; magnetic or electric dipole moments parallel to the propagation direction; $a/d = .45$; βd real.

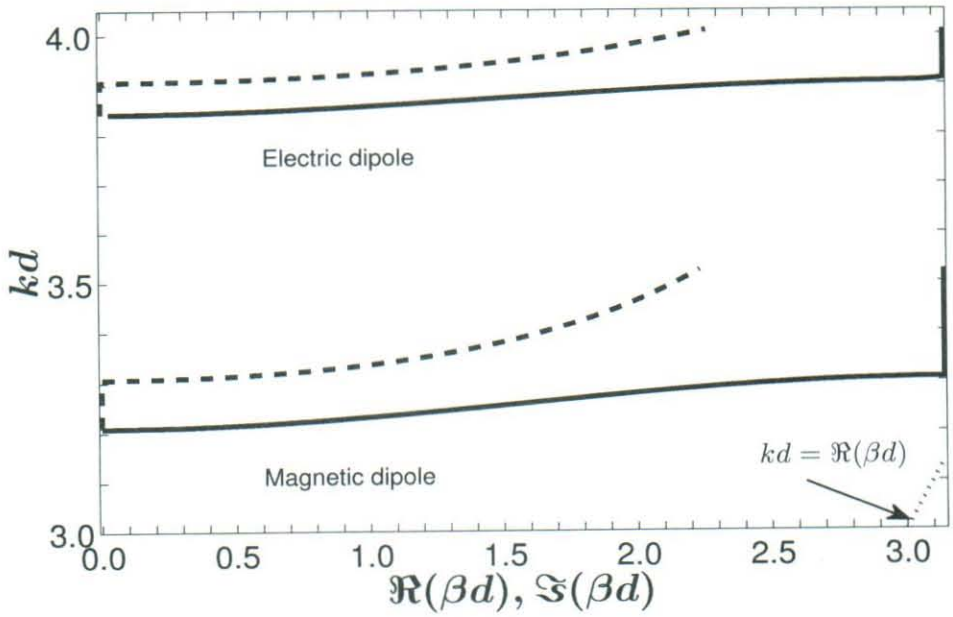

Figure 42: kd–βd diagram for a 3D cubic-lattice array of diamond spheres; magnetic or electric dipole moments parallel to the propagation direction; $a/d = .45$; βd complex.

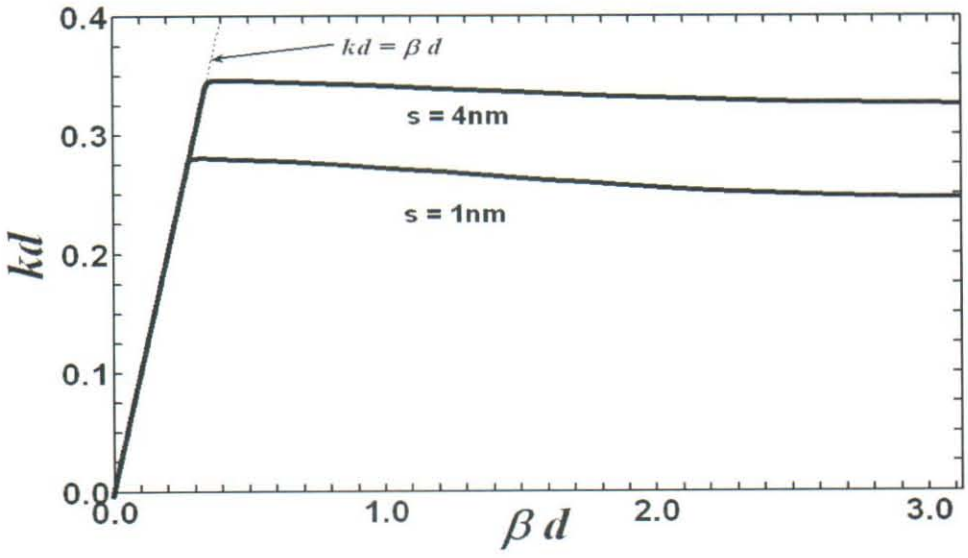

Figure 43: kd–βd curves for a 1D periodic array of glass-embedded silver nanospheres; dipole moments normal to the propagation direction; $a = 5$ nm; permittivity real; βd real.

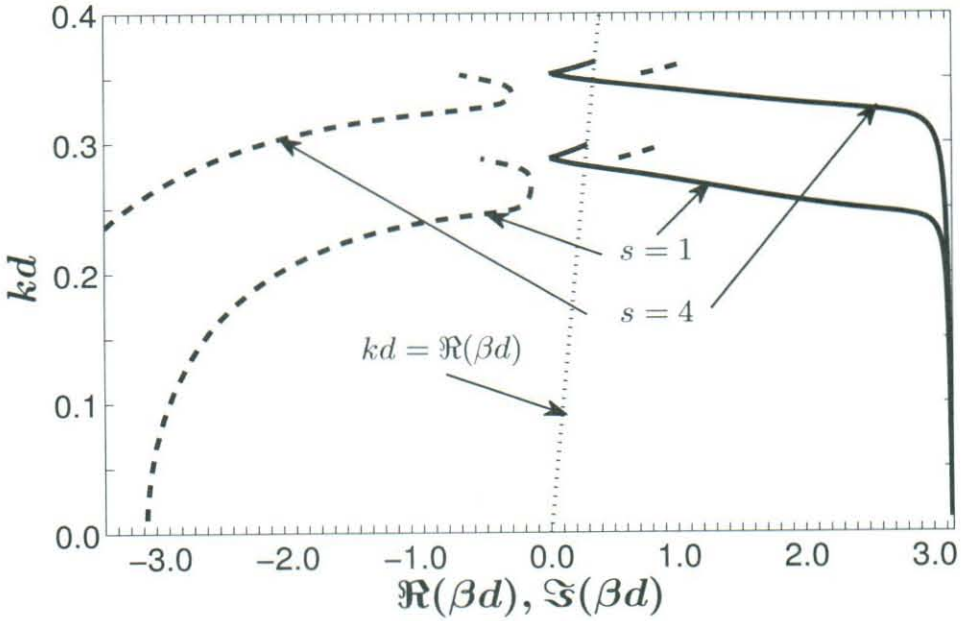

Figure 44: kd–βd curves for a 1D periodic array of lossy glass-embedded silver nanospheres; dipole moments normal to the propagation direction; $a = 5$ nm; βd complex.

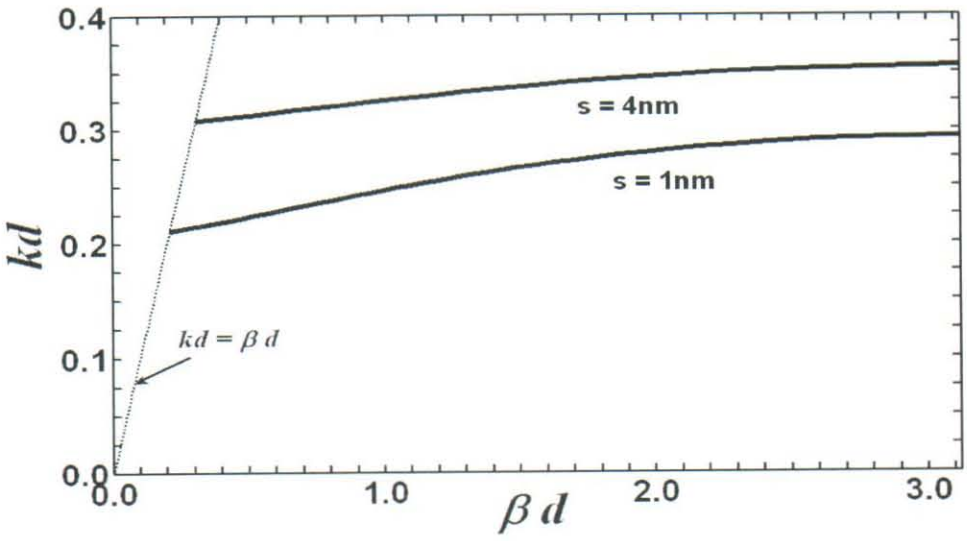

Figure 45: kd–βd curves for a 1D periodic array of glass-embedded silver nanospheres; electric dipole moments parallel to the direction of propagation; $a = 5$ nm; permittivity real; βd real.

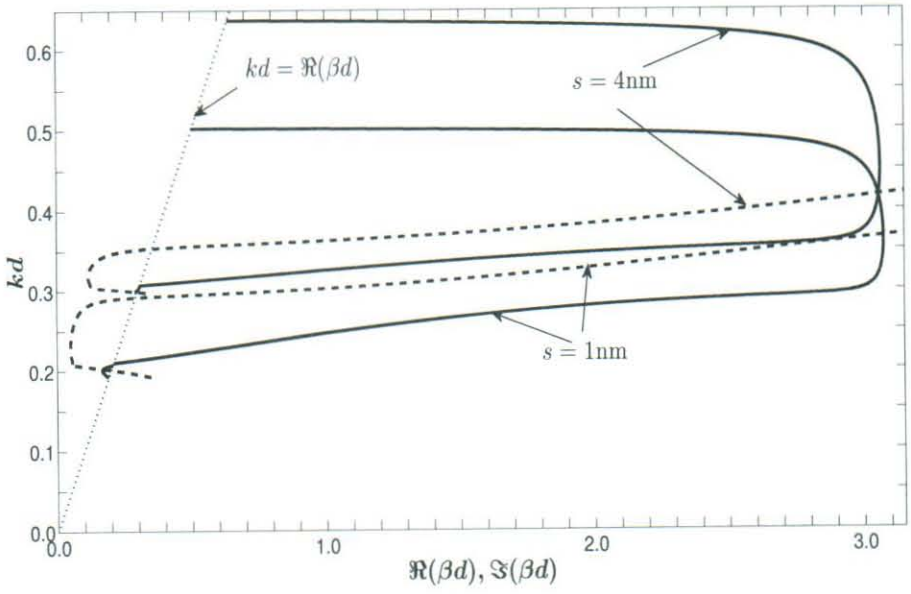

Figure 46: kd–βd curves for a 1D periodic array of lossy glass-embedded silver nanospheres; electric dipole moments parallel to the direction of propagation; $a = 5$ nm; βd complex.

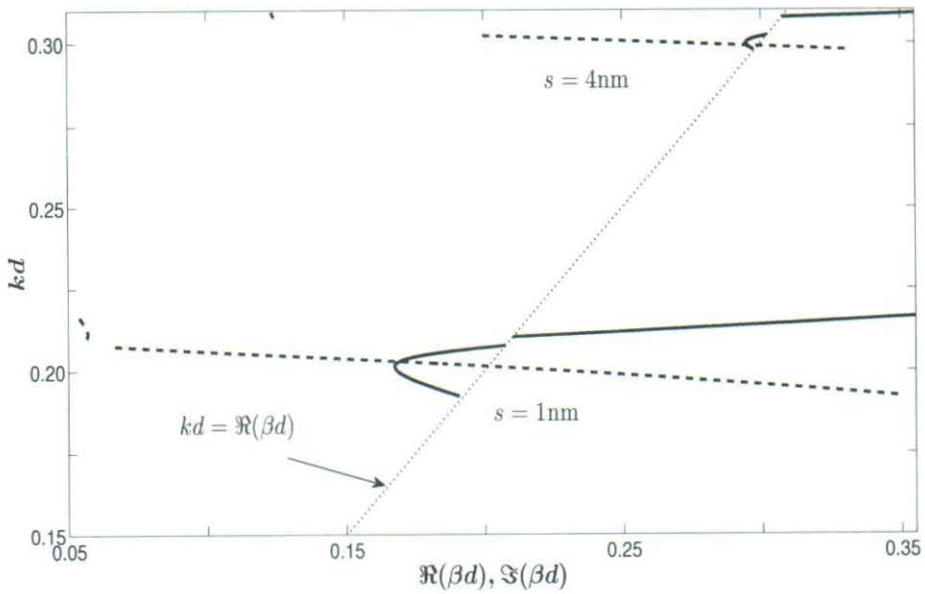

Figure 47: kd–βd curves for a 1D periodic array of lossy glass-embedded silver nanospheres; electric dipole moments parallel to the direction of propagation; $a = 5$ nm; βd complex; detail.

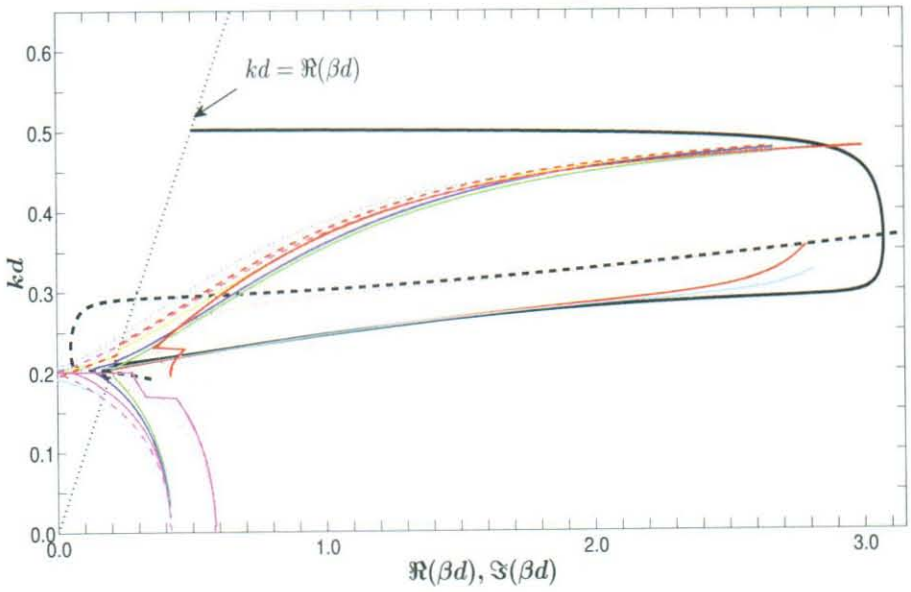

Figure 48: kd–βd curves for a 1D periodic array of lossy glass-embedded silver nanospheres; electric dipole moments parallel to the direction of propagation; $a = 5$ nm; βd complex; alternative branches shown.

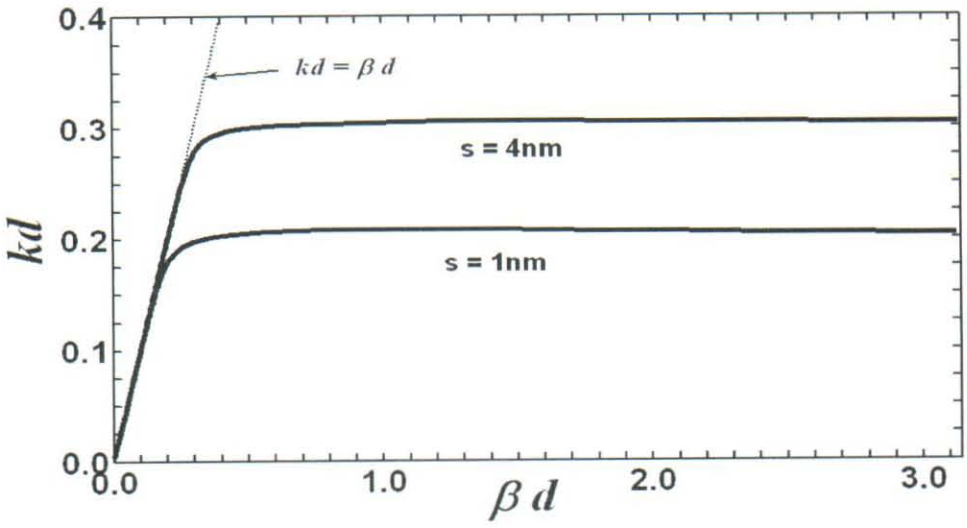

Figure 49: kd–βd curves for a 2D square-lattice array of glass-embedded silver nanospheres; electric dipole moments parallel to the array plane; $a = 5$ nm; $s = 1, 4$ nm; permittivity real; βd real.

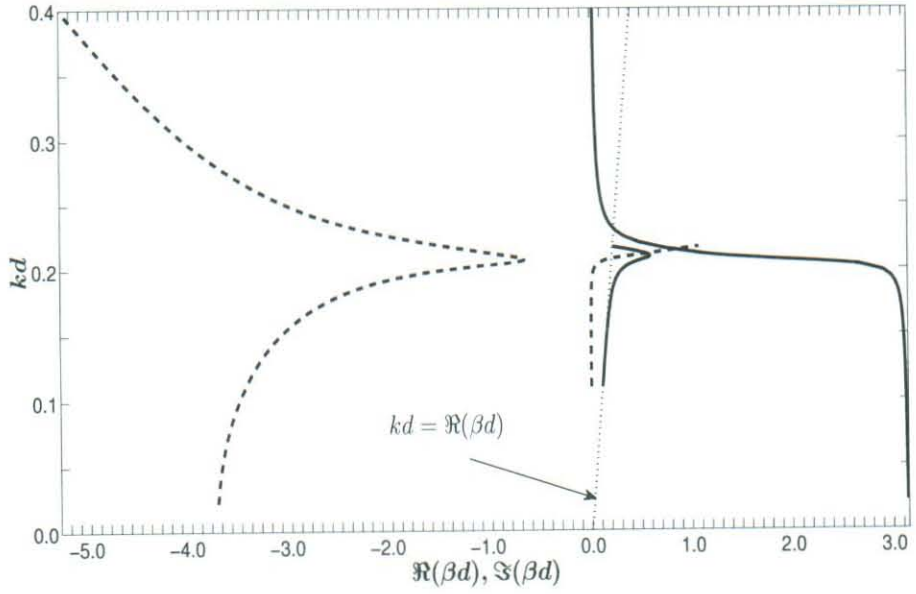

Figure 50: kd–βd curves for a 2D square-lattice array of glass-embedded silver nanospheres; electric dipole moments parallel to the array plane; $a = 5$ nm; $s = 1$ nm; permittivity complex; βd complex.

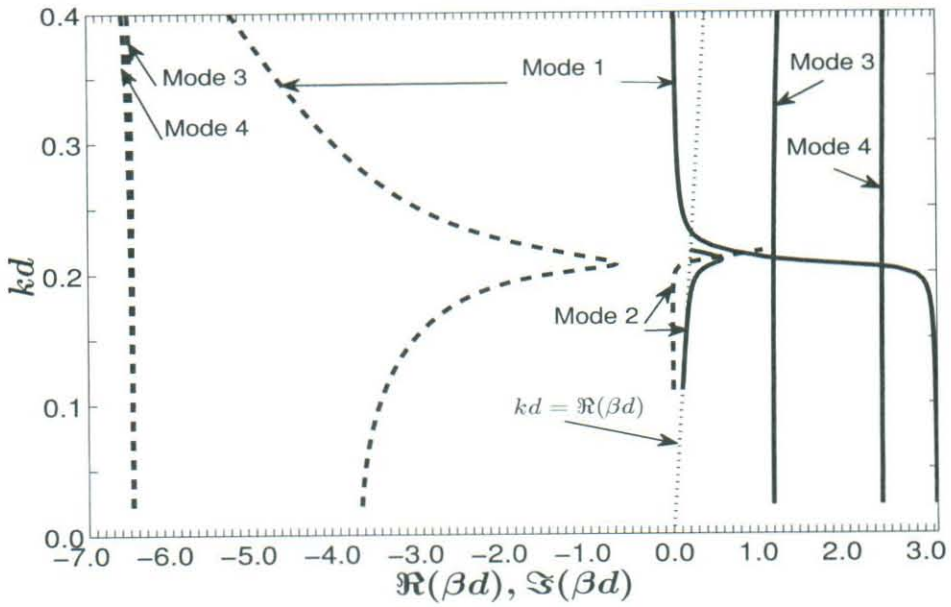

Figure 51: kd–βd curves for a 2D square-lattice array of glass-embedded silver nanospheres; electric dipole moments parallel to the array plane; $a = 5$ nm; $s = 1$ nm; permittivity complex; βd complex. Multiple modes shown.

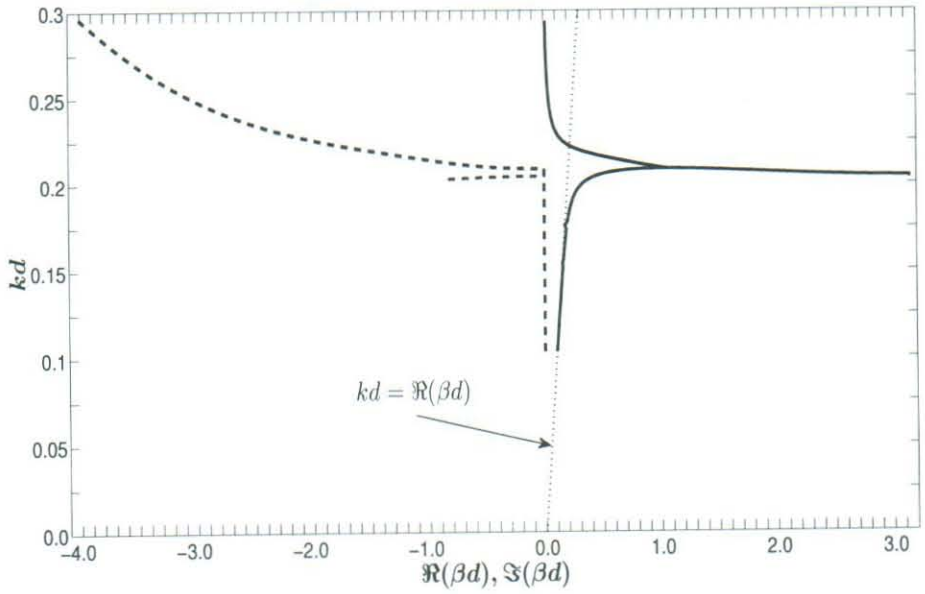

Figure 52: kd–βd curves for a 2D square-lattice array of glass-embedded silver nanospheres; electric dipole moments parallel to the array plane; $a = 5$ nm; $s = 1$ nm; permittivity real; βd complex.

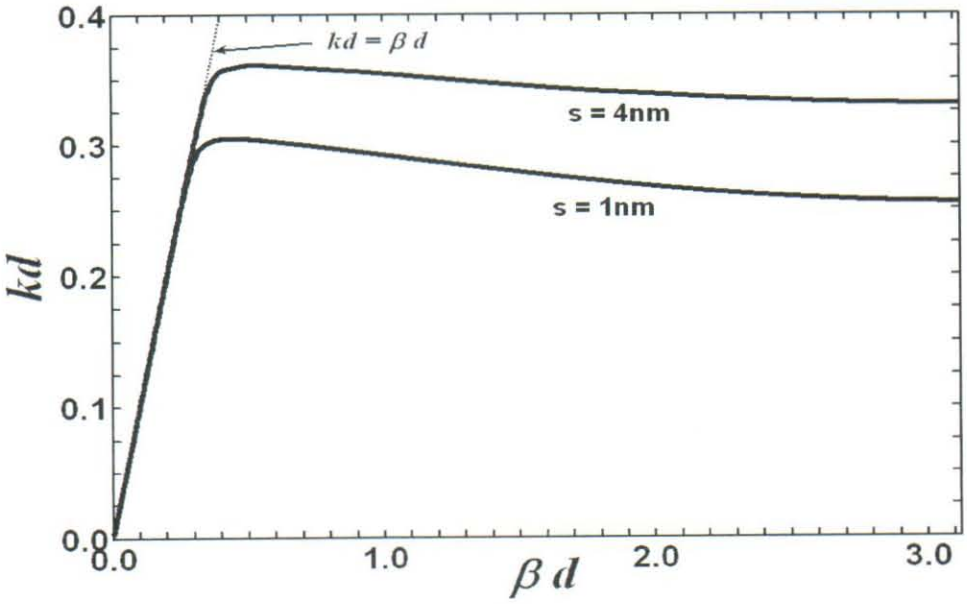

Figure 53: kd–βd curves for a 2D square-lattice array of glass-embedded silver nanospheres; electric dipole moments perpendicular to the array plane; $a = 5$ nm; $s = 1, 4$ nm; permittivity real; βd real.

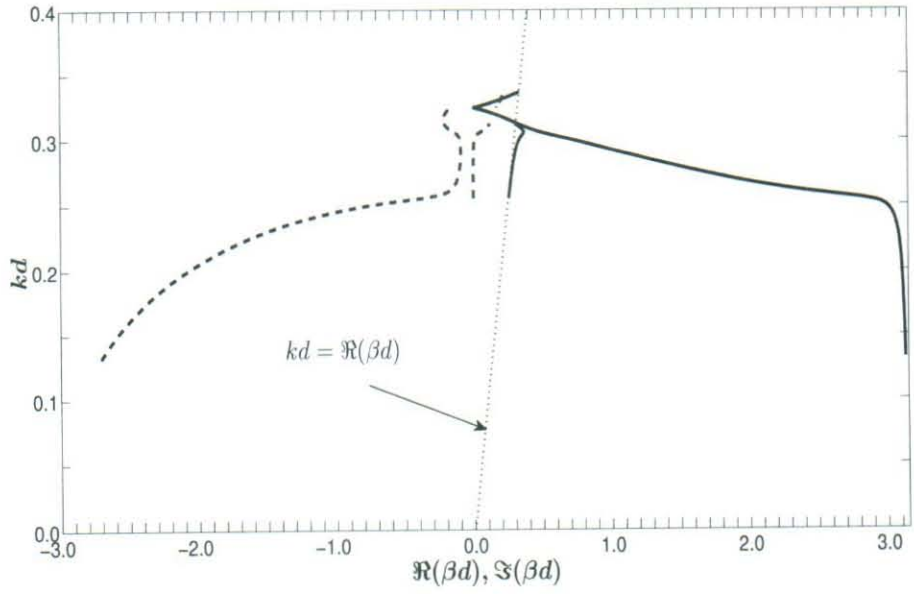

Figure 54: kd–βd curves for a 2D square-lattice array of glass-embedded silver nanospheres; electric dipole moments perpendicular to the array plane; $a = 5$ nm; $s = 1$ nm; permittivity complex; βd complex.

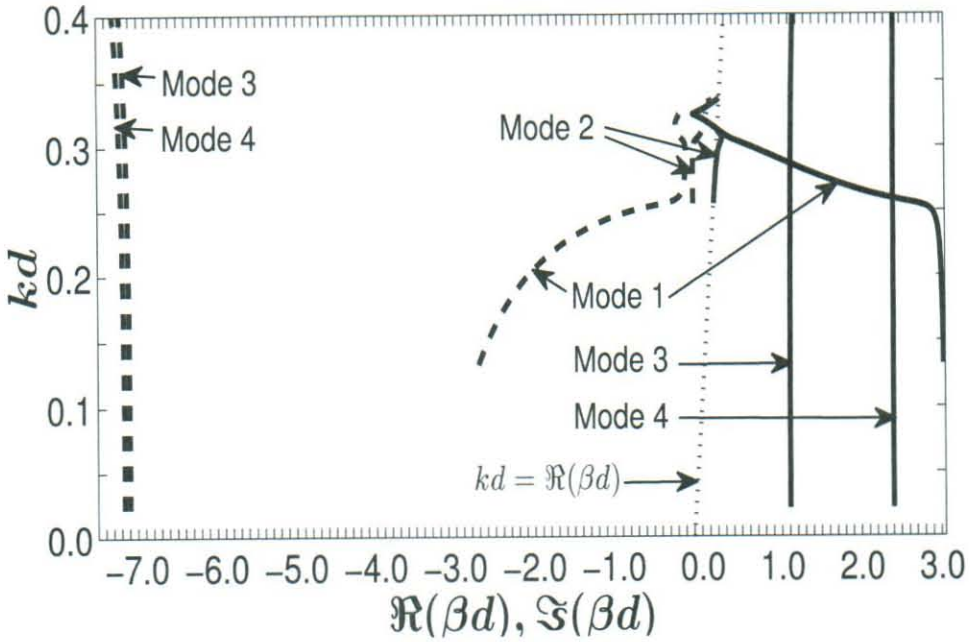

Figure 55: kd–βd curves for a 2D square-lattice array of glass-embedded silver nanospheres; electric dipole moments perpendicular to the array plane; $a = 5$ nm; $s = 1$ nm; permittivity complex; βd complex. Multiple modes shown.

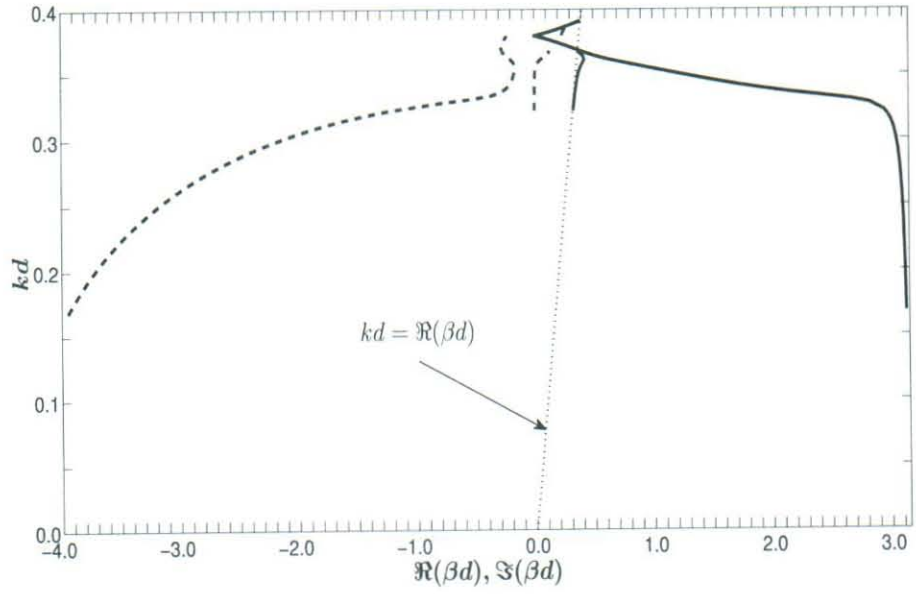

Figure 56: kd–βd curves for a 2D square-lattice array of glass-embedded silver nanospheres; electric dipole moments perpendicular to the array plane; $a = 5$ nm; $s = 4$ nm; βd complex.

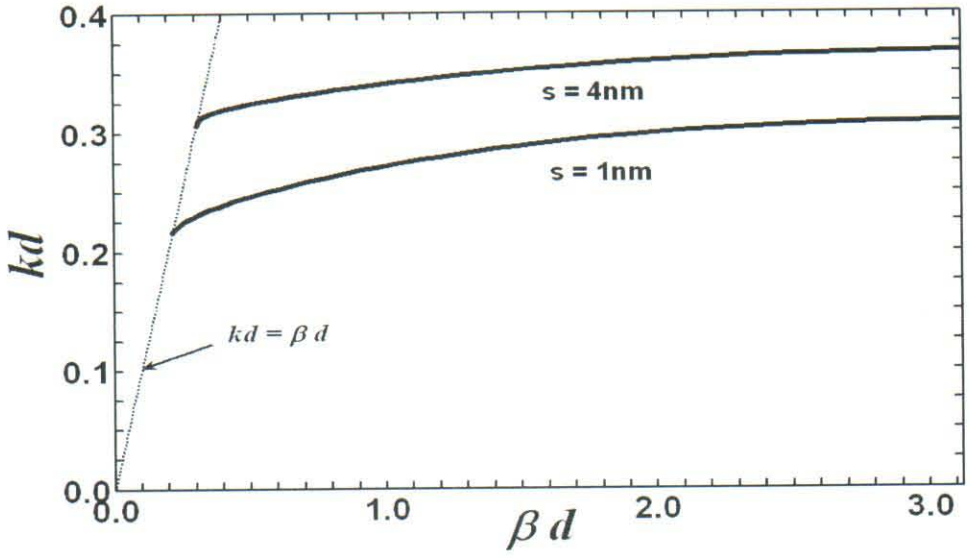

Figure 57: kd–βd curves for a 2D square-lattice array of glass-embedded silver nanospheres; electric dipole moments parallel to the direction of propagation; $a = 5$ nm; permittivity real; βd real.

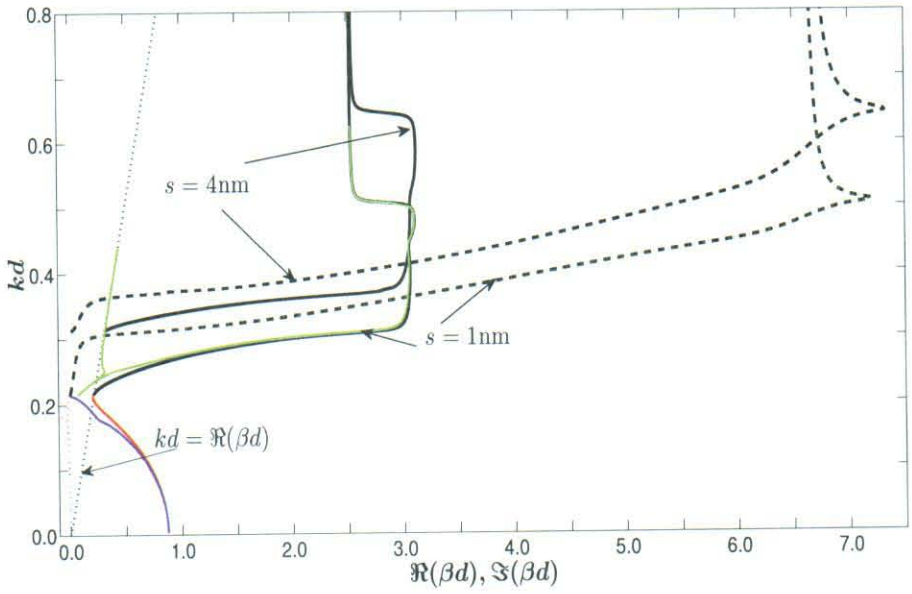

Figure 58: kd–βd curves for a 2D square-lattice array of glass-embedded silver nanospheres; electric dipole moments parallel to the direction of propagation; $a = 5$ nm; βd complex.

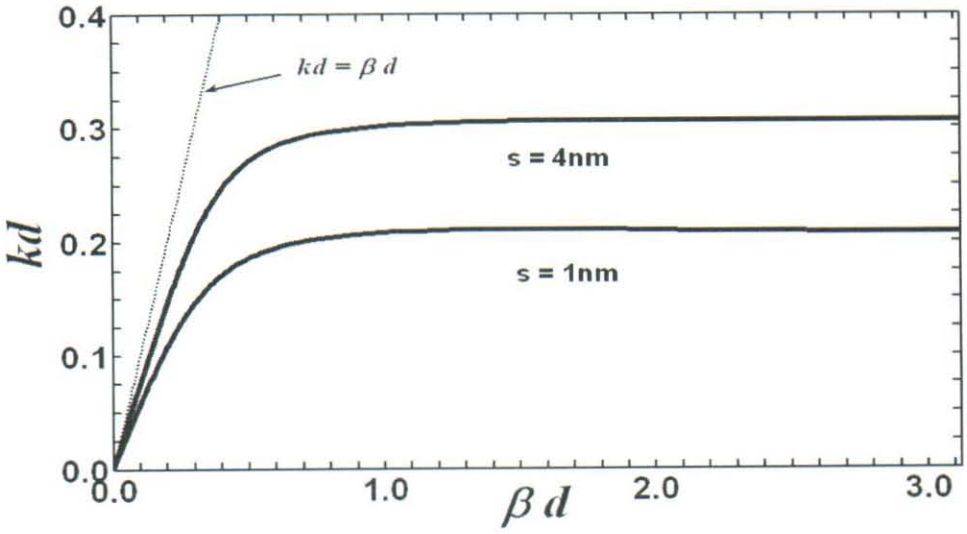

Figure 59: kd–βd curves for a 3D cubic-lattice array of glass-embedded silver nanospheres; dipole moments normal to the propagation direction; $a = 5$ nm; permittivity real; βd real.

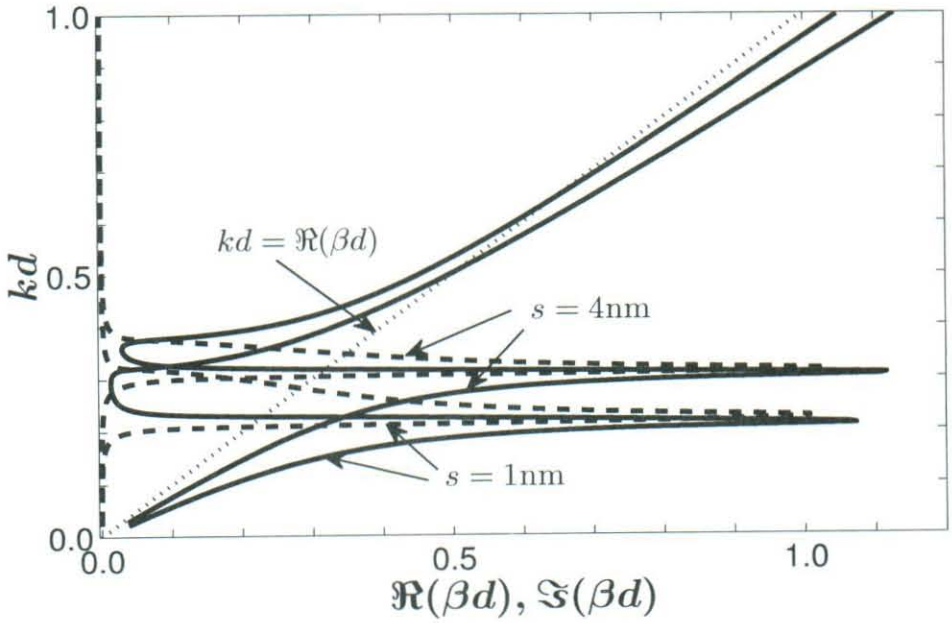

Figure 60: kd–βd curves for a 3D cubic-lattice array of glass-embedded silver nanospheres; dipole moments normal to the propagation direction; $a = 5$ nm; permittivity complex; βd complex.

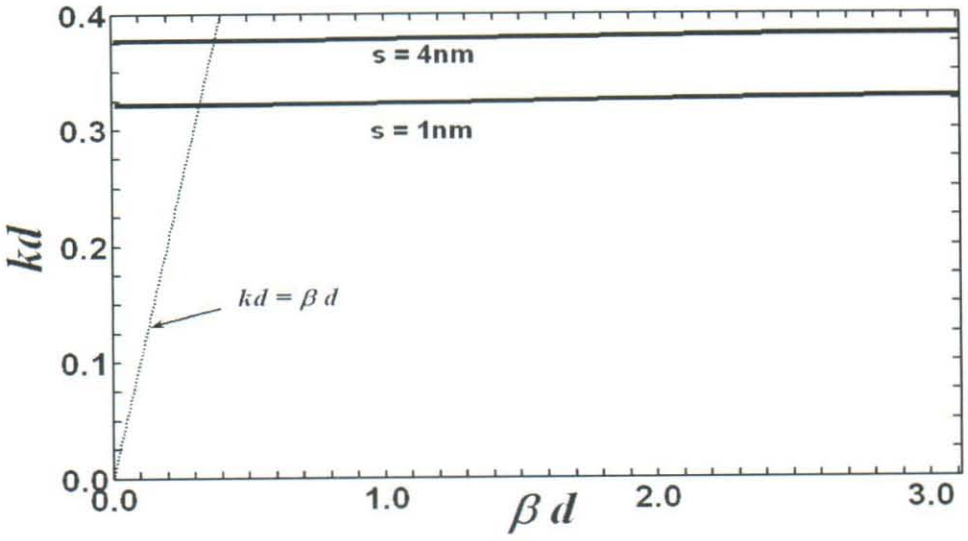

Figure 61: kd–βd curves for a 3D cubic-lattice array of glass-embedded silver nanospheres; electric dipole moments parallel to the direction of propagation; $a = 5$ nm ; permittivity real; βd real.

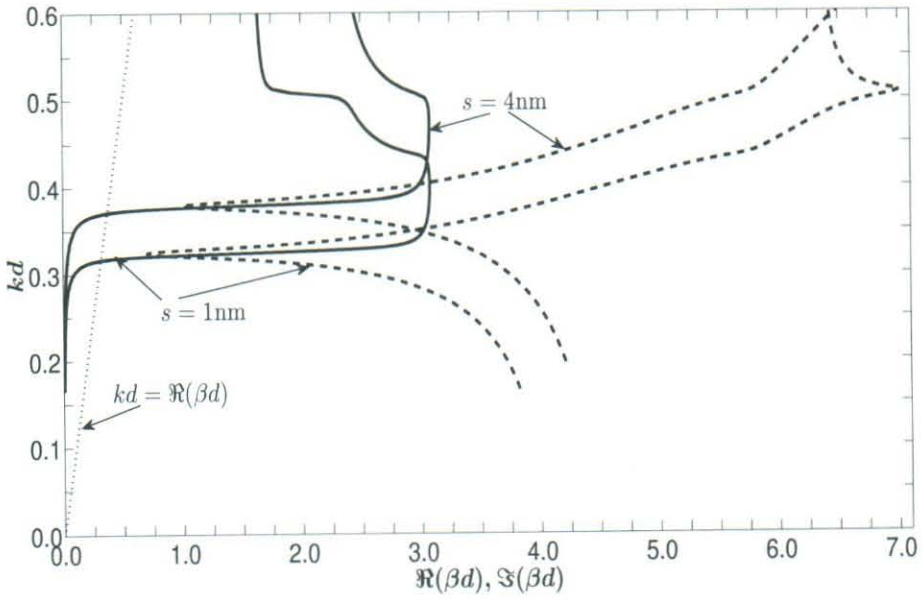

Figure 62: kd–βd curves for a 3D cubic-lattice array of glass-embedded silver nanospheres; electric dipole moments parallel to the direction of propagation); $a = 5$ nm; permittivity complex; βd complex.

A COMPLEX WAVES SUPPORTED BY A TWO-DIMENSIONAL SLAB

The key step of the analysis we have performed in this report is the derivation of the kd–βd equations for complex βd by analytically continuing the corresponding kd–βd equations for real βd into the complex βd plane. In this appendix we give an intuitive justification of this procedure by considering the problem of complex waves supported by a two-dimensional magnetodielectric slab above a ground plane. Although the structure treated here is continuous and not a discrete periodic structure as are the arrays treated in the main body of the report, the essential features are similar, and the analysis performed here will give much insight into the analytic continuation procedure used to derive the complex kd–βd equation. For an in-depth treatment of the subject of complex-plane representations of guided waves, see A. Hessel's chapter on the general characteristics of traveling waves, [52, ch. 19].

We consider three ways of obtaining the kd–βd equation for the slab problem: 1) solving the inhomogeneous boundary value problem, 2) solving the homogeneous boundary value problem, and 3) integrating over the polarization inside the slab. Throughout the appendix we assume that there is no variation of fields and sources with y and treat only E-waves, so that $E_x = E_z = 0$. As stated earlier in the report, an implicit harmonic time dependence of $\exp(-\mathrm{i}\omega t)$, $\omega > 0$, is assumed.

A.1 INHOMOGENEOUS BOUNDARY VALUE PROBLEM FOR THE SLAB

Consider a two-dimensional slab with thickness d of magnetodielectric material with permittivity ϵ and permeability μ above a perfectly conducting ground plane as shown in Fig. 63. The slab is illuminated by electric line sources located at a distance L or greater above the ground plane. The wave equation for $E_y(x,z)$ is then

$$\nabla^2 E_y(x,z) + k_0^2 E_y(x,z) = 0, \quad d < x < L \tag{A.1a}$$

$$\nabla^2 E_y(x,z) + k^2 E_y(x,z) = 0, \quad 0 < x < d\,. \tag{A.1b}$$

The boundary conditions for $E_y(x,z)$ are

$$E_y(0,z) = 0 \tag{A.2a}$$

$$E_y(d^+,z) = E_y(d^-,z)\,. \tag{A.2b}$$

The magnetic field $H(x,z)$ is given by

$$\mathbf{H}(x,z) = \frac{1}{\mathrm{i}\omega\mu_0}\nabla \times E_y(x,z)\,\hat{\mathbf{y}}, \quad d < x < L \tag{A.3a}$$

$$\mathbf{H}(x,z) = \frac{1}{\mathrm{i}\omega\mu}\nabla \times E_y(x,z)\,\hat{\mathbf{y}}, \quad 0 < x < d \tag{A.3b}$$

so that

$$H_z(x,z) = \frac{1}{\mathrm{i}\omega\mu_0}\frac{\partial E_y(x,z)}{\partial x}, \quad d < x < L \tag{A.4a}$$

$$H_z(x,z) = \frac{1}{\mathrm{i}\omega\mu}\frac{\partial E_y(x,z)}{\partial x}, \quad 0 < x < d \tag{A.4b}$$

and

$$\mu_r \frac{\partial E_y(d^+,z)}{\partial x} = \frac{\partial E_y(d^-,z)}{\partial x}, \quad \mu_r = \mu/\mu_0. \tag{A.5}$$

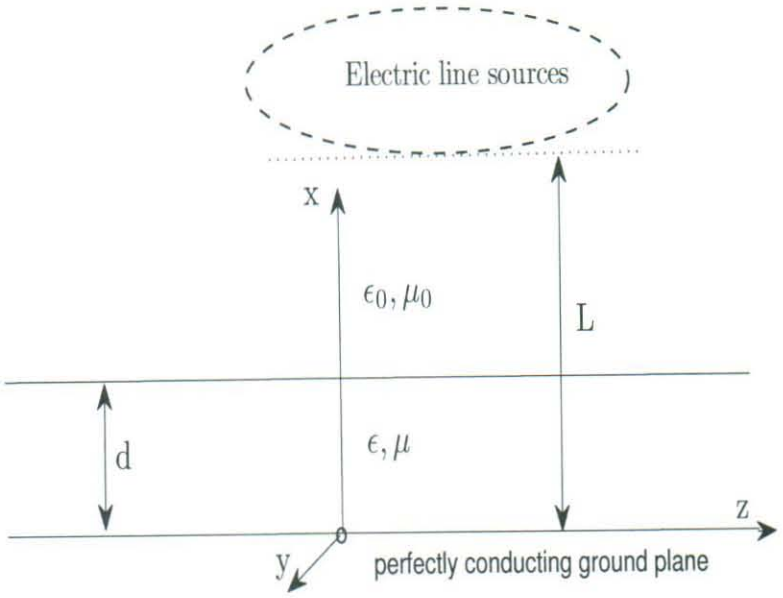

Figure 63: Slab geometry.

Now let $E_y(x,z)$ be expressed as the Fourier transform

$$E_y(x,z) = \int_{-\infty}^{\infty} E(x,\beta)\, \mathrm{e}^{\mathrm{i}\beta z}\mathrm{d}\beta, \quad x < L \tag{A.6a}$$

$$E(x,\beta) = \frac{1}{2\pi}\int_{-\infty}^{\infty} E_y(x,z)\, \mathrm{e}^{-\mathrm{i}\beta z}\mathrm{d}\beta, \quad x < L\,. \tag{A.6b}$$

Then it follows from (A.1)-(A.5) that $E(x,\beta)$ satisfies the following equations:

$$\frac{\mathrm{d}^2 E(x,\beta)}{\partial x^2} + (k_0^2 - \beta^2)E(x,\beta) = 0, \quad d < x < L \tag{A.7a}$$

$$\frac{\mathrm{d}^2 E(x,\beta)}{\partial x^2} + (k^2 - \beta^2)E(x,\beta) = 0, \quad 0 < x < d \tag{A.7b}$$

$$E(0,\beta) = 0 \tag{A.8a}$$

$$E(d^+,\beta) = E(d^-,\beta) \tag{A.8b}$$

and

$$\mu_r \frac{\mathrm{d}E(d^+,\beta}{\mathrm{d}x} = \frac{\mathrm{d}E(d^-,\beta}{\mathrm{d}x}\,. \tag{A.9}$$

From (A.7b) and (A.8b)

$$E(x,\beta) = A(\beta)\sin(k^2 - \beta^2)^{1/2}x, \quad 0 \le x \le d \tag{A.10}$$

and from (A.8a)

$$E(x,\beta) = B(\beta)\,\mathrm{e}^{\mathrm{i}[(k_0^2 - \beta^2)^{1/2}x]} + C(\beta)\,\mathrm{e}^{-\mathrm{i}[(k_0^2 - \beta^2)^{1/2}x]}, \quad d \le x < L \tag{A.11}$$

where $A(\beta)$, $B(\beta)$, and $C(\beta)$ are to be determined, so that from (A.8b) and (A.9)

$$B(\beta)\,\mathrm{e}^{\mathrm{i}[(k_0^2-\beta^2)^{1/2}d]} + C(\beta)\,\mathrm{e}^{-\mathrm{i}[(k_0^2-\beta^2)^{1/2}d]} = A(\beta)\sin[(k^2-\beta^2)^{1/2}d] \tag{A.12}$$

and

$$\mathrm{i}\mu_r(k_0^2-\beta^2)^{1/2}\left[B(\beta)\,\mathrm{e}^{\mathrm{i}[(k_0^2-\beta^2)^{1/2}d]} - C(\beta)\,\mathrm{e}^{-\mathrm{i}[(k_0^2-\beta^2)^{1/2}d]}\right]$$
$$= A(\beta)(k^2-\beta^2)^{1/2}\cos[(k^2-\beta^2)^{1/2}d]\,. \tag{A.13}$$

Assume that in (A.11) we can identify $C(\beta)\,\mathrm{e}^{-\mathrm{i}[(k_0^2-\beta^2)^{1/2}x]}$ with the field of the line sources in $d \le x < L$ incident on the slab, and $B(\beta)\,\mathrm{e}^{\mathrm{i}[(k_0^2-\beta^2)^{1/2}x]}$ with the field scattered from the slab in the region $x > d$ so that

$$E_{\mathrm{inc}}(x,\beta) = C(\beta)\,\mathrm{e}^{-\mathrm{i}[(k_0^2-\beta^2)^{1/2}x]}, \quad d \le x < L \tag{A.14a}$$

and

$$E_{\mathrm{sc}}(x,\beta) = B(\beta)\,\mathrm{e}^{\mathrm{i}[(k_0^2-\beta^2)^{1/2}x]}, \quad x \ge d\,. \tag{A.14b}$$

Then $(k_0^2-\beta^2)^{1/2}$ should be either positive real or positive imaginary (note that at this stage of the analysis β is real). Let

$$\gamma_0 = (k_0^2-\beta^2)^{1/2} \tag{A.15a}$$

and

$$\gamma = (k^2-\beta^2)^{1/2} \tag{A.15b}$$

with γ_0 positive real or positive imaginary so that (A.11) and (A.13) can be written as

$$B(\beta)\,\mathrm{e}^{\mathrm{i}\gamma_0 d} + C(\beta)\,\mathrm{e}^{-\mathrm{i}\gamma_0 d} = A(\beta)\sin\gamma d \tag{A.16a}$$

and

$$B(\beta)\,\mathrm{e}^{\mathrm{i}\gamma_0 d} - C(\beta)\,\mathrm{e}^{-\mathrm{i}\gamma_0 d} = \frac{A(\beta)\gamma\cos\gamma d}{\mathrm{i}\mu_r\gamma_0}\,. \tag{A.16b}$$

Letting

$$a(\beta) = \frac{A(\beta)}{C(\beta)} \tag{A.17a}$$

$$b(\beta) = \frac{B(\beta)}{C(\beta)} \tag{A.17b}$$

(A.16) takes the form

$$b(\beta)\,\mathrm{e}^{\mathrm{i}\gamma_0 d} - a(\beta)\sin\gamma d = -\mathrm{e}^{-\mathrm{i}\gamma_0 d} \tag{A.18a}$$

$$b(\beta)\,\mathrm{e}^{\mathrm{i}\gamma_0 d} - \frac{a(\beta)\gamma}{\mathrm{i}\mu_r\gamma_0}\cos\gamma d = -\mathrm{e}^{-\mathrm{i}\gamma_0 d} \tag{A.18b}$$

from which

$$a(\beta) = \frac{b(\beta)\,\mathrm{e}^{\mathrm{i}\gamma_0 d} + \mathrm{e}^{-\mathrm{i}\gamma_0 d}}{\sin\gamma d} \tag{A.19}$$

with

$$b(\beta) = \mathrm{e}^{-2\mathrm{i}\gamma_0 d}\,\frac{\tan\gamma d + \dfrac{\gamma}{\mathrm{i}\mu_r\gamma_0}}{\tan\gamma d - \dfrac{\gamma}{\mathrm{i}\mu_r\gamma_0}}\,. \tag{A.20}$$

Then from (A.6a) and (A.14b)

$$E_{y,sc}(x,z) = \int_{-\infty}^{\infty} b(\beta)C(\beta)\,\mathrm{e}^{\mathrm{i}\gamma_0 x}\,\mathrm{e}^{\mathrm{i}\beta z}\,\mathrm{d}\beta$$

$$= \int_{-\infty}^{\infty} C(\beta)\frac{\tan\gamma d + \dfrac{\gamma}{\mathrm{i}\mu_r\gamma_0}}{\tan\gamma d - \dfrac{\gamma}{\mathrm{i}\mu_r\gamma_0}}\,\mathrm{e}^{\mathrm{i}[\gamma_0(x-2d)]+\beta z]}\,\mathrm{d}\beta, \quad x > d\,. \tag{A.21}$$

If we close the infinite β integration in the complex β plane, we can find discrete propagating waves at the zeroes of the denominator in (A.21)

$$\tan\gamma d = \frac{\gamma d}{\mathrm{i}\mu_r\gamma_0 d} \tag{A.22}$$

with

$$\gamma d = [(kd)^2 - (\beta d)^2]^{1/2} \tag{A.23a}$$

$$\gamma_0 d = [(k_0 d)^2 - (\beta d)^2]^{1/2} \tag{A.23b}$$

and

$$(kd)^2 = \omega^2\mu\epsilon = (k_0)^2\mu_r\epsilon_r\,. \tag{A.23c}$$

(Note that $C(\beta)$, because of its identification with the coefficient of the field of the line sources incident on the slab, has no poles.) The zeroes of (A.22), the kd–βd equation, can be either real or complex depending on whether they are located along the real axis or in the half-plane of the complex β plane formed by closing the contour of integration at $|\beta| = \infty$. Thus the propagation constants of the complex propagating waves supported by the slab are obtained in effect by analytically continuing the kd–βd equation for real βd into the complex β plane, exactly the procedure we have employed in the analysis of the main body of the report. It is important to note that the original integration along the real β axis is equal not only to the sum of the residues at the poles of the kd–βd equation enclosed by closing the contour of integration, but also to the contributions of the integrations along and around the branch cuts of the kd–βd equation. These branch-cut integrals yield continuous radiation spectra of space waves that can be excited by external sources.

A.2 HOMOGENEOUS BOUNDARY VALUE PROBLEM FOR THE SLAB

Since the kd–βd equations in the main body of the report are obtained with no consideration of external sources, we now solve the homogeneous boundary value for the same slab. This can be done simply by setting $C(\beta) = 0$ in (A.16) since $C(\beta)$ is the coefficient of the field of the line sources incident on the slab. Thus

$$B(\beta)\,\mathrm{e}^{\mathrm{i}\gamma_0 d} = A(\beta)\sin\gamma d \tag{A.24a}$$

and

$$B(\beta)\,\mathrm{e}^{\mathrm{i}\gamma_0 d} = \frac{A(\beta)\gamma\cos\gamma d}{\mathrm{i}\mu_r\gamma_0}\,. \tag{A.24b}$$

from which we immediately obtain the kd–βd equation for the homogeneous slab boundary value problem

$$\frac{\gamma d}{\mathrm{i}\mu_r\gamma_0 d} = \tan\gamma d \tag{A.25}$$

which is identical to the kd–βd equation, (A.22), we have obtained for the inhomogeneous boundary value problem. It should be noted that although we have here obtained the solution to the

homogeneous slab boundary value problem by specializing the solution to the inhomogeneous slab boundary value problem, it could have been obtained directly without reference to the inhomogeneous slab problem by treating the homogeneous slab problem as an open waveguide problem and assuming a propagating mode supported by the waveguide. The advantage of proceeding as we have, however, is that the procedure of obtaining the dispersion equation for complex β by analytically continuing the dispersion equation for real β is then clearly understood as a simple consequence of closing the infinite real β integration in the complex β plane.

A.3 INTEGRATION OVER POLARIZATION

The derivation of kd–βd equations in the main body of the report is based on obtaining the electric and magnetic field at the center of a reference sphere by summing the scattered field contributions from all the other spheres in the array, and not on solving a boundary value problem. It is therefore of interest to show that the kd–βd equations for the slab that we have obtained by solving the slab boundary value problems can also be obtained by the procedure, analogous to that used in the array analysis, of integrating over the polarization in the slab to get the fields at $z = 0$ and then equating them to $E_y(x, 0)$. We consider the field of a single propagating wave in the slab which from (A.10) and (A.23a) takes the form

$$E_y(x, z) = A(\beta) \sin \gamma x \, \mathrm{e}^{\mathrm{i}\beta z}, \quad 0 \le x \le d, \quad \beta \text{ real.} \tag{A.26}$$

The analysis is simpler if the ground plane is dropped and the slab extended to $x = -d$. For simplicity we will assume here that $\mu_r = 1$. Then there is no magnetic polarization and the only source is the electric polarization

$$P_y(x, z) = (\epsilon - \epsilon_0) A(\beta) \sin \gamma x \, \mathrm{e}^{\mathrm{i}\beta z}, \quad -d \le x \le d, -\infty < z < \infty. \tag{A.27}$$

The field everywhere, written as an integral of the polarization $P_y(x, z)$, is given by

$$E_y(x, z) = \frac{\mathrm{i}\omega^2 \mu_0}{4} \int_{-\infty}^{\infty} \int_{-d}^{d} P_y(x', z') H_0^1 \left[k_0 \sqrt{(x - x')^2 + (z - z')^2} \right] \mathrm{d}x' \mathrm{d}z'$$

$$= \frac{\mathrm{i}k_0^2(\epsilon_r - 1)}{4} A(\beta) \int_{-\infty}^{\infty} \int_{-d}^{d} \sin \gamma x' \, \mathrm{e}^{\mathrm{i}\beta z'} \, H_0^1 \left[k_0 \sqrt{(x - x')^2 + (z - z')^2} \right] \mathrm{d}x' \mathrm{d}z' \, . \tag{A.28}$$

At $z = 0$

$$E_y(x, 0) = \frac{\mathrm{i}k_0^2(\epsilon_r - 1)}{2} A(\beta) \int_{-d}^{d} \sin \gamma x' \mathrm{d}x' \int_{0}^{\infty} \cos \beta z' \, H_0^1 \left[k_0 \sqrt{(x - x')^2 + z'^2} \right] \mathrm{d}z' \, . \tag{A.29}$$

Referring to [58, 6.677(8)(9)]

$$\int_0^{\infty} \cos \beta z' \, H_0^1 \left[k_0 \sqrt{(x - x')^2 + z'^2} \right] \mathrm{d}z' = \frac{\mathrm{e}^{\gamma_0 |x - x'|}}{\gamma_0} \tag{A.30}$$

where as usual

$$\gamma_0 = (k_0^2 - \beta^2)^{1/2}, \quad \gamma_0 \text{ positive real or positive imaginary.} \tag{A.31}$$

Substituting (A.30) in (A.29) and performing the integration with respect to x' we obtain

$$E_y(x, 0) = \frac{A(\beta)}{\gamma_0} \left[-\mathrm{e}^{\mathrm{i}\gamma_0 d} \sin \gamma_0 x \, (\gamma \cos \gamma d - \mathrm{i}\gamma_0 \sin \gamma d) + \gamma_0 \sin \gamma x \right]$$

$$= -\frac{A(\beta)\,\mathrm{e}^{\mathrm{i}\gamma_0 d}}{\gamma_0}\sin\gamma_0 x\,(\gamma\cos\gamma d - \mathrm{i}\gamma_0\sin\gamma d) + A(\beta)\sin\gamma x \tag{A.32}$$

But from (A.26)

$$E_y(x,0) = A(\beta)\sin\gamma x\,. \tag{A.33}$$

Hence, equating (A.32) and (A.33)

$$\gamma\cos\gamma d - \mathrm{i}\gamma_0\sin\gamma d = 0 \tag{A.34}$$

or

$$\tan\gamma d = \frac{\gamma}{\mathrm{i}\gamma_0} = \frac{\gamma d}{\mathrm{i}\gamma_0 d} \tag{A.35}$$

identical with the kd–βd equations, (A.22) and (A.25), that we have obtained by solving the inhomogeneous and homogeneous slab boundary value problems, respectively, when $\mu_r = 1$. Note that, just as in the periodic case with the divergent summations for complex propagating waves, if we integrate the polarization of the complex wave as in (A.28) the exponentially increasing polarization as $z \to +\infty$ or $-\infty$ depending on whether $\Im(\beta) < 0$ or > 0, respectively, makes the integral diverge.

B DIVERGENCE OF COMPLEX-WAVE FIELDS OBTAINED FROM DIRECT SUMMATION OF DIPOLE FIELDS OF PERIODIC ARRAYS

In this appendix we address the issue of divergent dipole-field summations for complex waves, namely that when a traveling wave supported by a periodic array of dipole inclusions has a complex propagation constant, the field incident on a reference element of the array obtained by summing the fields produced by all the other array elements becomes infinite. Although the infinite summation can be properly handled (as we do in deriving the kd–βd equation for complex βd by starting with the corresponding summation when the propagation constant is real and rewriting the summation in a form that can be analytically continued into the complex βd plane), nevertheless the divergence of the summation evaluated at complex β remains and deserves explanation. Of course, a simple mathematical reason for the divergence of the summation is the exponentially increasing terms of the summation as $z \to -\infty$ (for complex waves decaying in the $+z$ direction) caused by the non-zero imaginary part of the complex βd, but we will show here that a deeper physical insight into this divergence can be obtained by considering not only a complex traveling wave itself but also the sources needed to excite it. While it may at first seem inconsistent to be discussing sources in a report that centers on obtaining as much information about a traveling wave as is possible by treating only the homogeneous problem without any explicit consideration of sources, it will be seen that the introduction of sources that eventually recede to an infinite distance is required to elucidate the divergences. In particular, we want to explain physically why the infinite summation diverges for complex propagation constants, whereas the analytic continuation of the summation from real to complex propagation constants is well behaved.

The fields of the traveling waves with either real or complex propagation constants β satisfy Maxwell's equations. Thus, if all sources of these traveling waves are taken into account, the fields produced by all the sources must equal the fields of the traveling waves whether or not the propagation constants of the traveling waves are real or complex. Since the infinite summation of the dipolar fields of a traveling wave produced by the dipoles of the array diverges if the propagation constant of the traveling wave is complex, it follows that there must be sources at infinity other than the dipoles that produce fields to cancel the divergence and to yield the fields of the complex traveling wave. Moreover, since the infinite summation of the dipolar fields of a traveling wave with real β converges to the fields of that traveling wave, any sources at infinity (specifically, at $z = -\infty$ assuming that the power flow of the wave is in the $+z$ direction) needed to excite the real β traveling wave contribute negligibly to the fields of that traveling wave in bounded space. The remainder of this appendix substantiates this argument with supporting derivations.

Suppose we want to excite only the fields of a single traveling wave (decaying in the $+z$ direction for complex β or with power flow in the $+z$ direction for real β) in the half space of a semi-infinite array of dipole scatterers located at $z = 0, d, 2d, 3d, \cdots, \infty$. An equivalence principle can be derived that says we can do this by applying surface electric and magnetic currents on the plane $z = 0^-$ equal to $-\hat{\mathbf{z}} \times \mathbf{H}_e$ and $\hat{\mathbf{z}} \times \mathbf{E}_e$, respectively, where $\mathbf{E}_e$ and $\mathbf{H}_e$ are the fields of the sources in the half space $z < 0$.

For 1D arrays, the derivation of this equivalence principle involves taking the infinite array of dipoles carrying the single traveling wave and applying the Kottler-Franz integral formula [38, sec. 8.14],[72] to a closed surface consisting of the $z = 0^-$ infinite plane and the hemispherical surface of infinite radius in the region $z > 0$ that caps the infinite plane. The sources on this closed surface are the equivalent electric and magnetic surface currents, $\hat{\mathbf{n}} \times \mathbf{H}$ and $-\hat{\mathbf{n}} \times \mathbf{E}$, respectively, where $\hat{\mathbf{n}}$

is the outward normal to the surface. For proper complex waves,[27] the fields of the traveling waves decrease exponentially in magnitude as the radius approaches infinity. Thus, the exponentially decreasing $\hat{\mathbf{n}} \times \mathbf{H}$ and $-\hat{\mathbf{n}} \times \mathbf{E}$ surface current sources at infinity do not contribute to the fields inside the closed surface (as determined by the Kottler-Franz integration) and only surface currents on an effectively finite extent of the $z = 0^-$ plane contribute source fields. Moreover, the Kottler-Franz integration of the part of the equivalent surface current produced by the dipole sources in the half space $z < 0$ is identically zero [38, sec. 8.14],[72] and thus $-\hat{\mathbf{z}} \times \mathbf{H}$ and $\hat{\mathbf{z}} \times \mathbf{E}$ can be replaced by -$\hat{\mathbf{z}} \times \mathbf{H}_e$ and $\hat{\mathbf{z}} \times \mathbf{E}_e$.

For 2D arrays, the same argument applies using a semi-circular infinite cylindrical surface to cap the $z = 0^-$ plane. The axis of the infinite cylinder is in the plane of the 2D array perpendicular to the direction of propagation of the traveling wave, and the equivalent surface currents at the ends of the cylinder contribute negligible fields compared to the fields from the surface currents on the $z = 0^-$ plane as the length of the cylinder approaches infinity. For 3D arrays (which have no improper waves), semi-infinite planes at $x = \pm\infty$ and $y = \pm\infty$, and an infinite plane at $z = +\infty$ can be used to cap the $z = 0^-$ plane. The contribution to the fields at bounded values of z from the Kottler-Franz integration on the infinite $z = +\infty$ plane can be made to go to zero by inserting a small imaginary part of β to make the fields attenuate to zero as $z \to +\infty$. Then the contribution to the fields from the Kottler-Franz integrations on the semi-infinite $x = \pm\infty$ and $y = \pm\infty$ planes are also negligible compared to the fields from the surface currents on the $z = 0^-$ plane. (The insertion of a small imaginary part of β to attenuate the fields to zero as z approaches $\pm\infty$ for 3D arrays is also needed to assure the convergence of the infinite 3D summation of dipole fields; see Footnote 11 in the Introduction.)

Consequently, for 1D, 2D, and 3D semi-infinite arrays, the fields of the traveling wave in the half space $z > 0$ can be expressed as the sum $[\sum_{n=0}^{\infty} \mathbf{E}_{\mathrm{d}n}, \sum_{n=0}^{\infty} \mathbf{H}_{\mathrm{d}n}]$ of the fields of the dipoles plus the fields $[\mathbf{E}_s, \mathbf{H}_s]$ of the surface currents in the plane $z = 0^-$. In particular, for the electric field

$$\mathbf{E} = \sum_{n=0}^{\infty} \mathbf{E}_{\mathrm{d}n} + \mathbf{E}_s, \quad z > 0\,. \tag{B.1}$$

Now move the entire half space of dipoles with their plane of surface currents to the left along the $-z$ axis a distance $z_0 = Nd$, where N is a positive integer, while keeping the coordinate system fixed. Then the expression for the electric field of the traveling wave in (B.1) becomes

$$\mathbf{E}_0 = \sum_{n=-N}^{\infty} \mathbf{E}_{\mathrm{d}0n} + \mathbf{E}_{s0}, \quad z > -z_0\,. \tag{B.2}$$

[27] For outgoing improper waves, that is, the "leaky waves" (the waves in Fig. 65 with right-pointing arrows), the exponentially increasing fields at infinity contribute to the Kottler-Franz equivalent surface-current integration. Because, however, these surface currents represent fields propagating away from the axis of the array, their contribution to the fields inside the closed surface is no larger than that of the fields produced by the surface currents on the $z = 0^-$ plane and thus their contribution can be included by adding extra finite surface currents on the $z = 0^-$ plane. Moreover, even though the surface currents on the $z = 0^-$ plane increase exponentially as the transverse radius ρ approaches ∞, they can be diminished slowly to zero as a function of ρ with negligible effect on the fields well within the transverse radius of the undiminished surface currents. For incoming improper waves (the waves in Fig. 65 with left-pointing arrows), the integration over the hemispherical surface adds fields with spatial dependence $e^{i(\beta z + \kappa\rho)}$ to $[\mathbf{E}_s, \mathbf{H}_s]$. Nevertheless, these extra fields contribute terms that are finite in equation (B.5) and thus do not change the conclusions drawn from (B.5).

Because outgoing improper complex waves (leaky waves) decaying for $z > 0$ can effectively be excited by sources at $z = 0^-$, such leaky waves often represent the dominant fields in certain regions of space in the solutions to waveguide excitation problems. In contrast, the incoming improper waves require excitation surface currents on both the $z = 0^-$ plane and its capping surface. Thus, incoming improper waves do not generally represent a significant contribution to the fields in the solution to waveguide excitation problems [64].

For z_0 (or equivalently N) large enough, the electric field of the surface currents (now on the $z = (-z_0)^-$ plane) at a large distance from the plane will have the general far-field behavior $\mathbf{E}_{s0} \approx \mathbf{F}_s\, \mathrm{e}^{\mathrm{i}kz_0}/f(z_0)$ where $f(z_0) = z_0$, $\sqrt{z_0}$, and 1 for 1D, 2D, and 3D arrays, respectively. $\mathbf{F}_s$ is not a function of z_0 and the approximation becomes exact as $z_0 \to \infty$. Thus, as z_0 gets large, equation (B.2) can be rewritten as

$$\mathbf{E}_0 = \sum_{n=-N}^{\infty} \mathbf{E}_{\mathrm{d}0n} + \frac{\mathbf{F}_s}{f(z_0)}\, \mathrm{e}^{\mathrm{i}kz_0}, \quad z > -z_0\,. \tag{B.3}$$

However, as $z_0 \to \infty$ the fields $[\mathbf{E}_0, \mathbf{H}_0]$ of a traveling wave with a complex propagation constant β will become exponentially small at any finite value of z. Fortunately, the original values of the fields of the traveling wave that existed in the initial half space $z > 0$ can be restored by simply multiplying (B.3) by the exponential $\mathrm{e}^{-\mathrm{i}\beta z_0}$ to get

$$\mathbf{E} = \sum_{n=-N}^{\infty} \mathbf{E}_{\mathrm{d}n} + \frac{\mathrm{e}^{-\mathrm{i}\beta z_0}}{f(z_0)} \mathbf{F}_s\, \mathrm{e}^{\mathrm{i}kz_0}, \quad z > -z_0 \tag{B.4}$$

since $\mathbf{E} = \mathbf{E}_0 \mathrm{e}^{-\mathrm{i}\beta z_0}$ and $\mathbf{E}_{\mathrm{d}n} = \mathbf{E}_{\mathrm{d}0n} \mathrm{e}^{-\mathrm{i}\beta z_0}$. With β complex and $\Im(\beta) > 0$ for complex waves that decay in the $+z$ direction, the factor $\mathrm{e}^{-\mathrm{i}\beta z_0}/f(z_0) \to \infty$ as $z_0 \to \infty$, and equation (B.4) becomes

$$\mathbf{E} = \sum_{n=-\infty}^{\infty} \mathbf{E}_{\mathrm{d}n} + (\infty)\mathbf{F}_s\, \mathrm{e}^{\mathrm{i}kz_0}, \quad z > -\infty\,. \tag{B.5}$$

This equation shows that the surface-current sources required to maintain a non-zero complex traveling-wave electric field, $\mathbf{E}$, at finite values of z, produce an electric field (last term in (B.5)) that diverges as these surface-current sources recede to $z = -\infty$ ($z_0 \to +\infty$). Since the traveling-wave electric field $\mathbf{E}$ in (B.5) is finite for all finite z, it follows that the summation in (B.5) of the fields produced by the infinite array of dipoles supporting the complex traveling wave must also diverge. Although this divergence is mathematically obvious because of the terms in the summation that grow exponentially large as $n \to -\infty$ (as mentioned at the beginning of this appendix), we have now shown physically that this divergence is a consequence of the infinite fields produced by the surface-current sources at $z = -\infty$ that are required to excite a complex wave that has finite fields at bounded values of z.

If, however, the traveling wave has a purely real propagation constant, the factor $\mathrm{e}^{-\mathrm{i}\beta z_0}/f(z_0) \to 0$ as $z_0 \to \infty$ for 1D and 2D arrays, and (B.4) reduces to

$$\mathbf{E} = \sum_{n=-\infty}^{\infty} \mathbf{E}_{\mathrm{d}n}, \quad z > -\infty \tag{B.6}$$

which implies that the fields of a traveling wave with a real propagation constant are equal to the fields produced by the dipoles alone, and that the fields of the sources at $z = -\infty$ required to excite a real β traveling wave do not contribute to the fields at bounded values of z (because they are proportional to $1/f(z_0) \to 0$ as $z_0 \to \infty$ for 1D and 2D arrays).

For traveling waves with purely real propagation constants on 3D arrays, $f(z_0) = 1$ and (B.4) becomes

$$\mathbf{E} = \sum_{n=-\infty}^{\infty} \mathbf{E}_{\mathrm{d}n} + \mathrm{e}^{\mathrm{i}(k-\beta)z_0}\, \mathbf{F}_s, \quad z > -\infty \tag{B.7}$$

which confirms that the infinite summation of unattenuated dipole fields of a 3D array converges except for an oscillatory contribution given by the last term in (B.7). This oscillatory term can be suppressed in the infinite summation of dipole fields by giving the dipoles a small attenuation as $z \to \pm\infty$; see Footnote 11 in the Introduction.

C PROPERTIES OF COMPLEX WAVES ON UNIFORM OR PERIODIC WAVEGUIDES

This appendix is divided into two sections. In Section C.1, we summarize the general properties of complex waves supported by uniform or periodic waveguides. In Section C.2, we discuss some of the distinguishing features of fast and slow waves.[28]

C.1 INTRODUCTION TO COMPLEX WAVES

Much of the information on complex waves summarized in this appendix can be found in greater detail in the references [64] and [36]. We shall use the term "complex wave" to refer to a time-harmonic ($e^{-i\omega t}$, $\omega > 0$) discrete wave with a longitudinal (z axis) propagation constant β that is neither purely real nor purely imaginary. The discrete waves with purely real propagation constants β on one-dimensional and two-dimensional lossless, open waveguides are commonly referred to as surface waves, and waves with purely imaginary propagation constants β (on open or closed waveguides) are commonly referred to as evanescent waves.

We begin by considering uniform or periodic, open (to free space) or closed infinite waveguides composed of lossy or lossless, reciprocal material. The waveguides can be one dimensional (1D) (uniform or periodic in the z-propagation direction but not in the x and y directions), two dimensional (2D) (uniform or periodic in the z-propagation direction and uniform or periodic in either the x or y direction but not in both the x and y directions), or three dimensional (3D) (uniform or periodic in the z-propagation direction, uniform or periodic in the x direction, and uniform or periodic in the y direction). Fully periodic 1D, 2D, or 3D waveguides are formed by 1D, 2D, or 3D infinite rectangular-lattice arrays of identical elements. *All 3D waveguides (uniform and periodic) can be considered closed waveguides* with respect to waves that are uniform or uniformly periodic in the two rectangular directions transverse to the z-propagation direction because there is no radiation loss transverse to the z-propagation (longitudinal) direction. For waveguides that are periodic in the z direction, β refers to the *primary* Floquet-mode propagation constant satisfying $|\Re(\beta d)| \leq \pi$. The complete spectrum[29] of waves, referred to as modes, on closed waveguides at any one frequency consists of an infinite number of discrete modes. The complete spectrum of waves (modes) on lossless uniform (in the z direction)[30] open waveguides at any one frequency consists of a denumerable (finite or infinite depending on the waveguide) number of discrete modes plus a continuous spectrum of "radiation modes." The discrete spectrum of modes on open waveguides is composed of all independent homogeneous solutions to Maxwell's equations that have exponentially decreasing fields in the direction transverse to the z-propagation axis (longitudinal direction) of the waveguide (and thus carry finite power along the z direction). These discrete modes are called proper waves. The corresponding discrete waves on lossless open waveguides that obey Maxwell's

[28] A good source for early references on the subject of complex waves on isotropic structures plus a treatment that in some ways complements ours is given in [73]. Also see the treatment of traveling waves by A. Hessel in [52, ch. 10], and the treatment of leaky waves by T. Tamir in [52, ch. 11] and by D. Jackson and A. Oliner in [37, sec. IV].

[29] The word "complete" is used here in its mathematical sense, as in a "complete set of eigenfunctions," to refer to the full set of independent solutions satisfying wave equations and boundary conditions including boundary conditions of finite fields at infinity.

[30] Open waveguides periodic in the z-propagation direction always have an infinite number of discrete higher order Floquet modes associated with each primary Floquet mode. Also, as indicated, there can be an infinite number of discrete complex modes (proper waves) on open waveguides that are uniform in the z-propagation direction [74], and we cannot rule out the possibility of an infinite number of primary complex Floquet modes on open waveguides that are periodic in the z propagation direction. There can also exist an infinite number of discrete improper complex waves on some waveguides [74].

homogeneous equations, but have exponentially increasing fields in the transverse direction, carry infinite power along the z direction and thus are not part of the complete spectrum of modes. They are called non-spectral or improper waves.[31]

It was proven in [36] that every complex (proper or improper) wave on a lossless, reciprocal, open or closed, uniform or periodic waveguide comes as one of a quadruplet of complex waves with propagation constants β, $-\beta$, β^*, and $-\beta^*$. Two of these complex waves decay exponentially in the $+z$ direction and two decay exponentially in the $-z$ direction.[32] Because the complex waves that increase exponentially in the z direction away from the sources (assumed finite in magnitude and extent) would dissipate an infinite amount of power if a small loss were inserted into the material of the waveguide, only the two complex waves decaying away from finite-power sources may exist to the right and to the left of the sources. That is, any allowable complex waves must attenuate in the z direction away from the sources.[33] Assuming β is the propagation constant of a complex wave decaying in the $+z$ direction to the right of the sources exciting a lossless, reciprocal waveguide, we can confine our attention to the two complex waves with propagation constants β and $-\beta^*$ because the complex waves with propagation constants $-\beta$, and β^* merely propagate with decay in the $-z$ direction to the left of the sources.

In [36] it was also proven that the electric and magnetic fields $(\mathbf{E}, \mathbf{H})$ of a complex wave with propagation constant β on a lossless, reciprocal waveguide simply change to $(\mathbf{E}^*, -\mathbf{H}^*)$ for the corresponding complex wave with propagation constant $-\beta^*$. Therefore, on open, lossless, reciprocal waveguides, the two complex waves decaying in the $+z$ direction with propagation constants β and $-\beta^*$ are either both proper waves (both part of the complete spectrum of discrete modes, which have fields that decrease exponentially transverse to the z axis of the waveguide) or both improper waves (with fields that increase exponentially transverse to the z axis of the waveguide and are not part of the complete spectrum of discrete modes). The exponential variation of the far fields of these two complex waves decaying to the right of the sources in the $+z$ direction can be found directly from Maxwell's equations as

$$\mathrm{e}^{\mathrm{i}\kappa\rho}\,\mathrm{e}^{\mathrm{i}\beta z} \text{ and } \mathrm{e}^{-\mathrm{i}\kappa^*\rho}\,\mathrm{e}^{-\mathrm{i}\beta^* z} \tag{C.1}$$

with

$$\beta = \Re(\beta) + \mathrm{i}\Im(\beta)\,, \qquad \Im(\beta) > 0 \tag{C.2}$$

and

$$\kappa = \pm\sqrt{k^2 - \beta^2}\,, \qquad k = \omega/c \tag{C.3}$$

[31] For evanescent waves ($\Re(\beta) = 0$), the proper and improper criteria of exponentially decreasing and increasing waves in the transverse direction are replaced by outgoing and incoming waves in the transverse direction. The limit case of a TEM surface wave ($\Im(\beta) = 0$) with $|\Re(\beta)| = k$ is not a proper wave because it carries an infinite amount of power in the longitudinal (z) direction.

[32] Since the waveguides are lossless, the exponential decay is consistent with energy conservation only if the total average (real part of the complex Poynting vector) power flow is zero for each proper complex wave across a transverse plane (z = constant plane). However, a pair of proper complex waves with z-propagation constants β and $-\beta^*$ do not generally display complex Poynting vector orthogonality and can transfer net complex power in the z direction [75]. Still, it can be shown that both $\mathbf{E} \times \mathbf{H}$ and real power flow for β and $-\beta^*$ proper complex modes exhibit orthogonality [73]. But unlike opposite decaying identical evanescent waves [76, p. 65], equation (99) in [75] can be used to show that opposite traveling identical proper complex waves (with z-propagation constants β and $-\beta$) exhibit complex power orthogonality and transfer no net complex power [73]. (As mentioned in the previous paragraph, the total power flow in the z direction for an improper complex wave on an open waveguide is infinite — a property that disallows them from the complete spectrum of open waveguides.)

[33] This, however, does not mean that a complex wave is a proper wave if it attenuates away from the sources in the z direction because improper complex waves on open waveguides can attenuate away from the sources but are disallowed as part of the complete spectrum because they carry infinite power in the z direction as a result of their exponential increase transverse to the z direction.

where κ is the transverse propagation constant of the primary Floquet mode (assuming its fields are not zero) with corresponding z-propagation constant β, and ρ refers to a direction transverse to the z axis.[34] If the sign of κ in (C.3) is chosen to make the $\Im(\kappa) > 0$, then the two complex waves in (C.1) on the open, lossless, reciprocal waveguide are proper waves. (For 2D open waveguides, we assume that the sign of κ is the same on both sides of the waveguide. For the more general case, see [77].) The two complex waves in (C.1) can also be written as

$$e^{i\mathbf{k}\cdot\mathbf{r}} \text{ and } e^{-i\mathbf{k}^*\cdot\mathbf{r}} \tag{C.4}$$

with

$$\mathbf{k} = \kappa\hat{\boldsymbol{\rho}} + \beta\hat{\mathbf{z}}\,, \qquad \mathbf{r} = \rho\hat{\boldsymbol{\rho}} + z\hat{\mathbf{z}} \tag{C.5}$$

and thus

$$\mathbf{k}\cdot\mathbf{k} = \mathbf{k}^*\cdot\mathbf{k}^* = k^2\,. \tag{C.6}$$

Equation (C.1) or (C.4) shows that the β and $-\beta^*$ waves correspond also to $\mathbf{k}$ and $-\mathbf{k}^*$ waves. Thus the only difference between the full propagation behavior of the β and $-\beta^*$ waves is the sign of the phase. From the equations in (C.6), we find that $\Re(\mathbf{k})\cdot\Im(\mathbf{k}) = 0$. Therefore, if one moves along the direction given by $\Re(\mathbf{k})$, specifically, $\mathbf{r} = \mathbf{r}_0 + \alpha\Re(\mathbf{k})$ with α a real number and $\mathbf{r}_0$ a fixed reference position, there is no change in the magnitude of the waves in (C.4) or (C.1). In other words, $\Re(\mathbf{k})$ is orthogonal to the equi-phase planes. Moreover, (C.4) shows that the magnitude of the wave varies exponentially in these equi-phase planes. That is, in the far-field, the local equi-phase and equi-magnitude lines are orthogonal. Consequently, with just constant-magnitude rays, we can depict the two proper complex waves determined by (C.4) or (C.1) as shown in Fig. 64, and the two improper complex waves determined by (C.4) or (C.1) as shown in Fig. 65. The two-headed arrows in each of the Figs. 64 and 65 along the rays are the respective directions of increasing phase of the two complex waves [the direction of $\Re(\mathbf{k})$]. A larger distance between the solid constant-magnitude rays indicates a smaller magnitude of the complex waves. In the directions normal to the rays (arrows), the phase is constant and the fields vary exponentially. This exponential variation is in the direction of $\Im(\mathbf{k})$ (along the dotted lines in Figs. 64 and 65).

Since the improper complex waves in Fig. 65 are not part of the complete spectrum of modes on the open, lossless, reciprocal waveguide, one could ask why we include them in our discussion. For one thing, these improper waves can convert to proper waves if the open waveguide is converted to a closed waveguide, for example, by surrounding it with a perfectly conducting cylinder [78]. Secondly, these improper waves still satisfy Maxwell's homogeneous equations everywhere ($r < \infty$) even though they are not finite as $\rho \to \infty$ and, thus, they are of theoretical interest. More importantly, however, in certain limited regions in the vicinity of the material-air boundaries of the waveguide, the improper wave with outward propagating energy, depicted by the arrows pointing toward the right (left) in Fig. 65 for forward (backward) improper complex waves, can represent

[34] If the primary Floquet mode decays exponentially in the ρ direction, all the Floquet modes decay exponentially in the ρ direction.

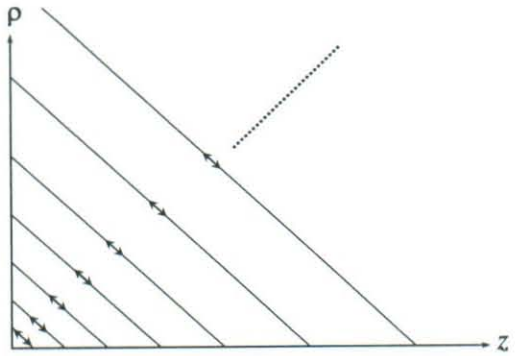

Figure 64: The two proper complex waves for $z > 0$ (to the right of the sources) on lossless, reciprocal, open waveguides.

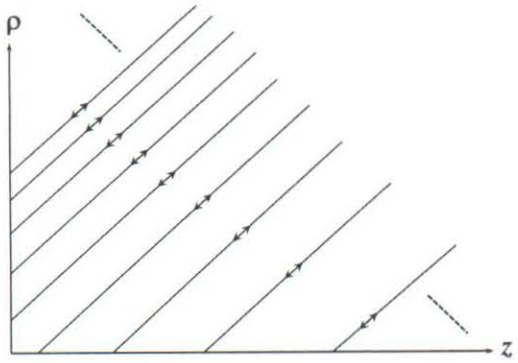

Figure 65: The two improper complex waves for $z > 0$ (to the right of the sources) on lossless, reciprocal, open waveguides.

the dominant portion of the fields [64], for example, on open dielectric-slab waveguides with permittivity greater than that of free space [74]. This outward-energy-propagating improper wave on an open waveguide is commonly referred to as the improper leaky wave. The inward-energy-propagating improper wave, depicted by the arrows pointing toward the left (right) in Fig. 65 for forward (backward) improper complex waves, has apparently never been found to represent a significant portion of the fields anywhere [64], presumably because it represents energy coming from sources at $\rho = \infty$ and z to the right of the waveguide sources; see Footnote 27. Proper complex waves are not found on open dielectric-slab waveguides with permittivity greater than that of free space, but are found, for example, on slab waveguides made with double negative materials [74]. Here in this report we find complex waves well within the slow-wave region where we expect they are proper waves (see, for example, Fig. 18).

In Section 8 of this report, we compute numerical values for the complex propagation constants (βd) versus frequency (kd) on 1D, 2D, and 3D periodic arrays of lossy and lossless, reciprocal magnetodielectric spheres. For the lossless open arrays (that is, for the 1D and 2D arrays), these complex values of βd alone do not uniquely determine the proper or improper nature of their associated complex waves. For example, suppose we find that $\Re(\beta) > 0$ and $\Im(\beta) > 0$ at a particular frequency. The sign ambiguity in (C.3) allows this wave to be either an improper leaky wave depicted in Fig. 65 with arrows pointing toward the right, or a proper complex wave depicted in Fig. 64 with arrows also pointing toward the right. One, of course, could distinguish between these two possibilities with additional information such as whether the waves are exponentially decreasing (proper wave) or increasing (improper wave) with transverse distance from the array; see last paragraph of Section 7.

On lossy waveguides, the complex conjugate waves become two separate waves with propagation constants not equal to the complex conjugate of each other [79]. Therefore, *to find backward-traveling waves on lossy waveguides, both positive and negative values of* $\Im(\beta)$ *must be considered to include all the* $+z$ *decaying complex waves if* $\Re(\beta)$ *is restricted to positive values in the computations.*

C.2 FAST AND SLOW WAVES

Whether the discrete wave is on a lossy or lossless, reciprocal or nonreciprocal, open waveguide, the equation for κ in (C.3) describes the transverse far field of the wave given by the exponential function $e^{i\kappa\rho}e^{i\beta z}$ in (C.1). With the real and imaginary parts of the z-propagation constant written

as $\beta = \beta_r + \mathrm{i}\beta_i$, the transverse propagation constant κ can be expressed from (C.3) as

$$\kappa = \pm\sqrt{k^2 + \beta_i^2 - \beta_r^2 - 2\mathrm{i}\beta_r\beta_i} \tag{C.7}$$

where we are concentrating on waves to the right side ($+z$ side) of the sources so that $\beta_i \geq 0$. The discrete wave is usually classified as a *fast wave* if $|\beta_r| < k$ and as a *slow wave* if $|\beta_r| \geq k$.

For $\beta_r\beta_i \neq 0$, we see from (C.7) that κ has a non-zero imaginary part and thus the sign in (C.7) can be chosen to yield a proper (or an improper) complex wave. Note, however, that we arrive at a contradiction if we assume that $\beta_i = 0$ and $|\beta_r| < k$, because then κ would be real and represent radiation outgoing to $\rho = +\infty$ (for the + sign in (C.7)) or radiation incoming from $\rho = +\infty$ (for the − sign in (C.7)). This radiation to or from $\rho = +\infty$ would not be compatible with an unattenuated wave ($\beta_i = 0$) in the z direction. *Therefore, for the fast-wave region $|\beta_r| < k$, the wave must be complex (or evanescent if $\beta_r = 0$).*[35]

For $\beta_i = 0$ on lossless, open waveguides and $|\beta_r| > k$, the discrete wave is a proper (exponentially decreasing with ρ) or improper (exponentially increasing with ρ) surface wave depending on the sign of the square root in (C.7). For $\beta_i > 0$, there is no reason that a discrete wave cannot be complex in the slow-wave region, that is, for $|\beta_r| \geq k$, even for lossless, open waveguides. For example, if $\beta_r = k$ on a lossless waveguide in (C.7), then $\kappa = 0$ (the limit case of a surface wave) for $\beta_i = 0$, but κ is complex for $\beta_i > 0$. In other words, it is possible for a non-zero value of β_i in a slow traveling wave ($\beta_r \geq k$) to produce radiation in the transverse direction compatible with energy conservation. This result has been confirmed by the asymptotic and numerical evaluations of k–β curves in [64] and [74]. The slow-wave range $k < |\beta_r| < k + \Delta k$ ($\Delta k > 0$) where the discrete wave is complex on a lossless, open waveguide is said by Tamir and Oliner [64] to be the region where there is a "winding down of the leaky-wave solution." Beyond this range ($|\beta_r| > k + \Delta k$), the wave becomes a surface wave with $\beta_i = 0$ on lossless, open waveguides.

[35] An exception to this rule would be a 1D or 2D lossless periodic array with a null in the embedded element pattern such that the fast wave having a phase progression corresponding to this null direction would see a radiation "blind spot" [25]. Such a radiationless fast wave would be a surface wave having no primary Floquet mode (for which $\kappa = \pm\sqrt{k^2 - \beta_r^2}$) but its dominant non-zero Floquet mode still described in the far field by $\mathrm{e}^{\mathrm{i}\kappa_{\mathrm{fast}}\rho}\mathrm{e}^{\mathrm{i}\beta z}$ with $\beta_i = 0$, $|\beta_r| < k$, and κ_{fast} imaginary [80].

References

[1] S. Haslbeck, K.-P. Martinek, L. Stievano, and F.E. Wagner, "Formation of gold nanoparticles in gold ruby glass: the influence of tin," *Proceedings of the 28th International Conference on the Applications of the Mössbauer Effect (ICAME 2005), Montpellier, France, 4-9 September 2005, Volume I (Part I-II/V)*, Berlin: Springer, 2007.

[2] P. Ikonen, "Artificial dielectrics and magnetics in microwave engineering: a brief historical revision," www.tkk.fi/Yksikot/Sahkommagnetiika/kurssit/S-96.4620/2006/reports/artificial_history_pekka.pdf, 2006.

[3] C.R. Simovski and S.A. Tretyakov, "Historical notes on metamaterials," ch. 1 in F. Capolino, Ed., *Metamaterials Handbook: Theory and Phenomena of Metamaterials,* Boca Raton, FL: Taylor and Francis CRC Press, 2009.

[4] J. Brown, "Artificial dielectrics," in J.B. Birks, Ed. *Progress in Dielectrics, vol. 2,* New York: Wiley, 1960.

[5] R.E. Collin, *Field Theory of Guided Waves; 2nd edition,* Piscataway, NJ: IEEE Press, 1991. (We reference the second edition of Collin's book. The first edition was published by McGraw-Hill in 1960 and contains the chapter on artificial dielectrics in almost the same form as the second edition.)

[6] J.-M. Lourtioz, H. Benisty, V. Berger, J.-M. Gérard, D. Maystre, and A. Tchelnokov, *Photonic Crystals: Towards Nanoscale Photonic Devices,* Berlin: Springer, 2005.

[7] J.D. Joannopoulous, S.G. Johnson, J.N. Winn, and R.D. Meade, *Photonic Crystals: Molding the Flow of Light, 2nd edition,* Princeton, NJ: Princeton University Press, 2008.

[8] K. Sakoda, *Optical Properties of Photonic Crystals,* Berlin: Springer, 2005.

[9] R.W. Ziolkowski and N. Engheta, Guest Editors, Metamaterial Special Issue, *IEEE Transactions on Antennas and Propagation,* vol. 51, no. 10, part 1, October 2003.

[10] C. Caloz and T. Itoh, *Electromagnetic Metamaterials: Transmission Line Theory and Microwave Applications,* Hoboken, NJ: Wiley-IEEE, 2005.

[11] G.V. Eleftheriades and K.G. Balmain, *Negative-Refraction Metamaterials: Fundamental Principles and Applications,* Hoboken, NJ: Wiley-IEEE, 2005.

[12] N. Engheta and R.W. Ziolkowski, Eds., *Electromagnetic Metamaterials: Physics and Engineering Explorations,* Hoboken, NJ: Wiley, 2006.

[13] E. Shamonina and L. Solymar, "Metamaterials: how the subject started," *Metamaterials,* vol. 1, issue 1, pp. 12–18, 2007, available online from ScienceDirect, www.sciencedirect.com.

[14] R. Marqués, F. Martín, and M. Sorolla, *Metamaterials with Negative Parameters: Theory, Design and Microwave Applications,* Hoboken, NJ: Wiley, 2008.

[15] C.R. Simovski, "Material parameters of metamaterials (a review)," *Optics and Spectroscopy,* vol. 107, no. 5, pp. 726–753, 2009.

[16] L. Solymar and E. Shamonina, *Waves in Metamaterials,* New York: Oxford University Press (USA), 2009.

[17] F. Capolino, Ed., *Metamaterials Handbook: Theory and Phenomena of Metamaterials,* Boca Raton, FL: Taylor and Francis CRC Press, 2009.

[18] F. Capolino, Ed., *Metamaterials Handbook: Applications of Metamaterials,* Boca Raton, FL: Taylor and Francis CRC Press, 2009.

[19] B. Munk, *Metamaterials: Critique and Alternatives,* Hoboken, NJ: Wiley, 2009.

[20] R.A. Shore and A.D. Yaghjian, *Traveling Electromagnetic Waves on Two- and Three-Dimensional Periodic Arrays of Lossless Acoustic Monopoles, Electric Dipoles, and Magnetodielectric Spheres*, Air Force Research Laboratory In-House Report, AFRL-SN-HS-TR-2006-0039, 2006. (PDF file available on request.)

[21] R.A. Shore and A.D. Yaghjian, "Traveling waves on two- and three-dimensional periodic arrays of lossless scatterers," *Radio Sci.*, 42, RS6S21, doi:10.1029/2007RS003647 19 December 2007.

[22] R.A. Shore and A.D. Yaghjian, "Traveling waves on three-dimensional periodic arrays of two different alternating magnetodielectric spheres," *IEEE Trans. Antennas Propagat.*, vol. 57, pp. 3077–3091, October, 2009.

[23] C.L. Holloway, E.F. Kuester, J. Baker-Jarvis, and P. Kabos, "A doubly negative (DNG) composite medium composed of magneto-dielectric spherical particles embedded in a matrix," *IEEE Trans. Antennas Propagat.*, vol. 51, pp. 2596–2603, October 2003.

[24] L. Lewin, "The electrical constants of a material loaded with spherical particles," *Proc. Inst. Elec. Eng.*, vol. 94, pp. 65–68, 1947.

[25] A.D. Yaghjian, "Scattering-Matrix Analysis of Linear Periodic Arrays," *IEEE Trans. Antennas Propagat.*, vol. 50, pp. 1050–1064, August 2002.

[26] R.A. Shore and A.D. Yaghjian, *Scattering-Matrix Analysis of Linear Periodic Arrays of Short Electric Dipoles*, Air Force Research Laboratory In-House Report, AFRL-SN-HS-TR-2004-045, 2004. (PDF file available on request.)

[27] R.A. Shore and A.D. Yaghjian, *Traveling Electromagnetic Waves on Linear Periodic Arrays of Small Lossless Penetrable Spheres*, Air Force Research Laboratory In-House Report, AFRL-SN-HS-TR-2004-044, 2004. (PDF file available on request.)

[28] R.A. Shore and A.D. Yaghjian, "Traveling electromagnetic waves on linear periodic arrays of lossless spheres," *Electronics Letters*, vol. 41, no. 10, pp. 578–580, 2005.

[29] R.A. Shore and A.D. Yaghjian, "Traveling electromagnetic waves on linear periodic arrays of lossless penetrable spheres," *IEICE Trans. Commun.*, vol. E88-B, no. 6, pp. 2346-2352, 2005.

[30] R.A. Shore and A.D. Yaghjian, "Traveling waves on 1D, 2D, and 3D arrays of acoustic monopoles and electromagnetic dipoles," Paper B02.10(400), *Proceedings of the XXVIIIth General Assembly of the International Union of Radio Science (URSI), New Delhi, India,* October 2005.

[31] C.M. Linton, "The Green's function for the two-dimensional Helmholtz equation in periodic domains," *J. Engineering Mathematics*, vol. 33, pp. 377–402, 1998.

[32] F. Capolino, D.R. Jackson, and D.R. Wilton, "Mode excitation from sources in two-dimensional EBG waveguide using the array scanning method," *IEEE Microwave and Wireless Components Letters*, vol. 15, no. 2, pp. 49–51, February 2005.

[33] C.L. Holloway, M. Mohamed, E. Kuester, and A. Dienstfrey, "Reflection and transmission properties of a metafilm: with an application to a controllable surface composed of resonant particles," *IEEE Trans. Electromagnetic Compatibility*, vol. 47, Issue 4, pp. 833–844, November 2005.

[34] C.M. Linton, R. Porter and I. Thompson, "Scattering by a semi-infinite periodic array and the excitation of surface waves," *SIAM J. Appl. Math.*, vol. 67, no. 5, pp. 1233–1258, 2007.

[35] A. Ishimaru, *Electromagnetic Wave Propagation, Radiation, and Scattering*, Englewood Cliffs, NJ: Prentice Hall, 1991.

[36] A.D. Yaghjian, "Bidirectionality of reciprocal, lossy or lossless, uniform or periodic waveguides," *IEEE Microwave and Wireless Components Letters*, vol. 17, pp. 480–482, July 2007.

[37] D.R. Jackson and A.A. Oliner, "Leaky-wave antennas," Ch. 7 of C.A. Balanis, Ed., *Modern Antenna Handbook (v.1)*, Hoboken, NJ: Wiley, 2008.

[38] J.A. Stratton, *Electromagnetic Theory*, New York: McGraw-Hill, 1941.

[39] S. Tretyakov, *Analytical Modeling in Applied Electromagnetics*, Boston MA: Artech House, 2003.

[40] T.B. Hansen and A.D. Yaghjian, *Plane-Wave Theory of Time-Domain Fields: Near-Field Scanning Applications*, Piscataway, NJ: Wiley-IEEE, 1999.

[41] D.S. Citrin, "Plasmon-polariton transport in metal-nanoparticle chains embedded in a gain medium," *Optics Letters* vol. 31, no. 1, pp. 98–100, 2006.

[42] A.F. Koenderink and A. Polman, "Complex response and polariton-like dispersion splitting in periodic and metal nanoparticle chains," *Phys. Rev. B*, vol. 74, 033402, 2006.

[43] A. Alù and N. Engheta, "Theory of linear chains of metamaterial/plasmonic particles as subdiffraction optical nanotransmission lines," *Phys. Rev. B*, vol. 74, 205436, 2006.

[44] J.E. Dennis, Jr. and R.B. Schnabel, *Numerical Methods for Unconstrained Optimization and Nonlinear Equations*, Englewood Cliffs, NJ: Prentice-Hall, 1983.

[45] D.E. Müller, "A method for solving algebraic equations using an automatic computer," *Mathematical Tables and Aids to Computation* vol. 10, pp. 208–215, 1956.

[46] W.H. Press, B.P. Flannery, S.A. Teukolsky, and W.T. Vetterling, *Numerical Recipes in FORTRAN 77: The Art of Scientific Computing (v. 1), 2nd edition*, New York: Cambridge University Press, p. 364, 1992.

[47] L. Tsang and B. Wu, "Electromagnetic fields of Hertzian dipoles in layered media of moderate thickness including the effects of all modes," *IEEE Antennas and Wireless Propagation Letters*, vol. 6, pp. 316–319, 2007.

[48] C.R. Simovski and S. He, "Frequency range and explicit expressions for negative permittivity and permeability for an isotropic medium formed by a lattice of perfectly conducting Ω particles," *Physics Letters A*, vol. 311, pp. 254–263, 2003.

[49] L. Brillouin, *Wave Propagation in Periodic Structures: Electric Filters and Crystal Lattices, 2nd edition*, New York: Dover, 1953.

[50] M.J. Buerger, *Contemporary Crystallography*, New York: McGraw-Hill, 1970.

[51] V.M. Agranovich and V.L. Ginzburg, *Spatial dispersion in crystal optics and the theory of excitons*, New York: Wiley-Interscience, 1966; see also 2nd Edition, New York: Springer-Verlag, 1984.

[52] R.E Collin and F.J. Zucker, Eds. *Antenna Theory, Part 2*, New York: McGraw-Hill, 1969.

[53] C.H. Walter, *Traveling Wave Antennas*, New York: Dover, 1970.

[54] L. Lewin, *Polylogarithms and Associated Functions*, New York: Elsevier North Holland, 1981.

[55] L.C. Maximon, "The dilogarithm function for complex argument," *Proc. R. Soc. London A*, vol. 459, pp. 2807–2819, 2003.

[56] R.E. Crandall, "Note on fast polylogarithm computation," PDF file http://people.reed.edu/~crandall/papers/Polylog.pdf, 2006.

[57] C.M. Linton, "Schlömilch series that arise in diffraction theory and their efficient computation," *J. Phys. A: Math. Gen.*, vol. 39, pp. 3325–3339, 2006.

[58] I.S. Gradshteyn and I.M. Ryzhik, *Table of Integrals, Series, and Products; 6th edition*, Boston: Academic Press, 1994.

[59] M. Abramowitz and I.A. Stegun, Eds., *Handbook of Mathematical Functions*, New York: Dover Publications, 1965.

[60] W.K.H. Panofsky and M. Phillips, *Classical Electricity and Magnetism; 2nd edition*, Reading, MA: Addison-Wesley, 1962.

[61] C.R. Simovski, "Analytical-modelling of double-negative composites," *Metamaterials*, vol. 2, pp. 169–185, 2008.

[62] A. Yariv, *Optical Electronics; 4th edition*, Philadelphia, PA: Saunders College Publishing, 1991.

[63] E. Weisstein, "Polylogarithm", from Wolfram MathWorld, http://mathworld.wolfram.com/Polylogarithm.html.

[64] T. Tamir and A.A. Oliner, "Guided complex waves; part 1: fields at an interface," *Proc. IEE*, vol. 110, pp. 310–324, 1963.

[65] N. Engheta, A. Salandrino, and A. Alù, "Circuit elements at optical frequencies: nanoinductors, nanocapitors, and nanoresistors," *Phys. Rev. Lett.* vol. 95, 095504, 2005.

[66] A. Alù and N. Engheta, "Optical nanotransmission lines: synthesis of planar left-handed metamaterials in the infrared and visible regimes," *J. Opt. Soc. Am. B*, vol. 23, no. 3, March 2006.

[67] A. Alù and N. Engheta, "Three-dimensional nanotransmission lines at optical frequencies: a recipe for broadband negative-refraction optical metamaterials," *Phys. Rev. B*, vol. 75, 024304, 2007.

[68] A.D. Yaghjian, S. Maci, and E. Martini, Characteristic wave velocities in spherical electromagnetic cloaks, *New Journal of Physics*, vol. 11, doi: 10.1088/1367-2630/11/11/113011, 2009.

[69] P. Lampariello, F. Frezza, and A. A. Oliner, "The transition region between bound-wave and leaky-wave ranges for a partially dielectric-loaded open guiding structure," *IEEE Trans. Microwave Theory and Techniques*, vol. 38, no. 12, pp. 1831–1836, December 1990.

[70] P.B. Johnson and R.W. Christy, "Optical constants of the noble metals," *Phys. Rev. B*, vol. 6, pp. 4370–4379, 15 December 1972.

[71] L.A. Sweatlock, S.A. Maier, H.A. Atwater, J.J. Penninkhof, and A. Polman, "Highly confined electromagnetic fields in arrays of strongly coupled Ag nanoparticles," *Phys. Rev. B*, vol. 71, pp. 235408-1–7, 2005.

[72] C.T. Tai, "Kirchhoff theory: scalar, vector, or dyadic?," *IEEE Trans. Antennas Propagat.*, vol. 20, pp. 114–115, January 1972.

[73] R. Islam and G.V. Eleftheriades, "On the independence of the excitation of complex modes in isotropic structures," *IEEE Trans. Antennas Propagat.*, to be published 2010.

[74] W. Shu and J.M. Song, "Complete mode spectrum of a grounded dielectric slab with double negative metamaterials," *Progress in Electromagnetics Research (PIER)*, vol. 65, pp. 103–123, 2006.

[75] P. Chorney, *Power and Energy Relations in Bidirectional Waveguides*, MIT Research Laboratory of Electronics Tech. Rep. 396, September 1961.

[76] D.M. Kerns, *Plane-Wave Scattering-Matrix Theory of Antennas and Antenna-Antenna Interactions*, NBS Monograph 162, Washington, DC: U.S. Government Printing Office, 1981.

[77] T. Tamir and F.Y. Kou, "Varieties of leaky waves and their excitation along multilayered structures," *IEEE J. Quantum Electronics*, vol. QE-22, pp. 544–551, April 1986.

[78] P.J.B. Clarricoats and B.C. Taylor, "Evanescent and propagating modes of dielectric-loaded circular waveguide," *IEE Proc.*, vol. 111, pp. 1951–1956, December 1964.

[79] W. Shu, *Electromagnetic Waves in Double Negative Metamaterials and Study on Numerical Resonances in the Method of Moments*, Ph.D. Dissertation, Iowa State University, Ames IA, 2008.

[80] N. Amitay, V. Galindo and C.P. Wu, *Theory and Analysis of Phased Array Antennas*, New York: Wiley-Interscience, 1972.